Theory of the periodic orbits of a chaotic quantum well

E. E. Narimanov and A. Douglas Stone
Applied Physics, Yale University, P.O. Box 208284, New Haven, Connecticut 06520-8284
(Received 14 April 1997)

A theory is developed for the periodic orbits of an electron trapped in a rectangular potential well under the influence of an electric field normal to the barriers and a magnetic field. When the magnetic field is parallel to the electric field the dynamics of an electron in the well is integrable; however, when it is tilted by an angle θ the system undergoes a transition to chaos. Motivated by recent experimental and theoretical studies of magnetotunneling in quantum wells that emphasize the role of periodic orbits, we present here a unified theory of all the periodic orbits within the well that are of relevance to experiments. We define the appropriate scaled variables for the problem, which we divide into two qualitatively different cases, the single-barrier model (depending on two parameters) and the double-barrier model (depending on three parameters). We show that in both cases all relevant orbits are related to bifurcations of period-one traversing orbits. A full analytic theory is derived for the period and stability of these traversing orbits; and analytic and numerical results are obtained for the important period-two and period-three orbits. An unusual feature of the classical mechanics of the double-barrier is a discontinuity in the classical Poincaré map, which leads to a new type of bifurcation that we term a cusp bifurcation. We show that all the periodic orbits that traverse the well exist only in finite intervals of voltage and magnetic field, appearing and disappearing in bifurcations. These intervals are shown to correspond to the appearance of new resonance peaks in the experimental data, laying the foundation for a quantitative semiclassical treatment of the system. [S0163-1829(98)05107-8]

I. INTRODUCTION

Most of our intuition about the properties of quantum systems comes from the consideration of Hamiltonians with high symmetry, for which the classical motion is integrable and hence the Schrödinger equation is separable. Symmetry-breaking terms are typically treated by perturbation theory and the physics is described in terms of transitions induced between stationary states of the symmetric problem. This approach fails when the symmetry-breaking terms become too large and many levels of the unperturbed system are strongly mixed. In this situation one approach is direct numerical solution of the nonseparable Schrödinger equation using a large basis set and calculation of the expectation values of interest from the numerically determined eigenstates. For most problems of interest the computational effort involved is substantial, particularly if one wishes to explore a large parameter space of Hamiltonians and not just a single fixed set of parameters. Moreover, an exclusively numerical approach makes it very difficult to understand qualitatively the dependence of physical properties on the parameters of the problem and thus to generalize the results to other related systems.

An alternative approach that can give greater physical insight is to use the semiclassical methods developed for nonintegrable systems during the past two decades by researchers studying ''quantum chaos,'' i.e., the quantum manifestations of chaotic classical dynamics. This approach has been used successfully in atomic physics during the past decade. Of particular note is the theory of the spectra of Rydberg states in a high magnetic field (diamagnetic Kepler problem),[1,2] where a qualitative *and* quantitative understanding has been obtained semiclassically in excellent agreement with experiments. In that case the essential idea underlying the theory is a relationship between the quantum density of states (DOS) and a sum over isolated unstable periodic classical orbits first derived by Gutzwiller (the ''Gutzwiller Trace Formula'').[3] However this semiclassical formulation had to be extended to account quantitatively for experimental spectra, since these depend on other factors in addition to the density of states.[4]

Until recently there were no comparable applications of semiclassical theory to condensed-matter systems. Within the past few years, however, several such systems have been identified: ballistic microcavities,[5,6] two-dimensional antidot arrays,[7–9] and the system that is the subject of this paper, resonant tunneling diode in a magnetic field tilted by an angle θ with respect to the tunneling direction. It has become clear that of the three, the latter system allows the most detailed comparison between theory and experiment, because the microscopic Hamiltonian is known so accurately and because several continuous experimental control parameters may be tuned *in situ* to map out a large parameter space.

This system was first identified and studied by Fromhold and co-workers,[10] who immediately understood the close analogy to the Garton-Tomkins[1] spectral oscillations in the diamagnetic Kepler problem. When the tilt angle θ is zero the experiment corresponds to a conventional resonant magnetotunneling geometry; there is resonant structure in the I-V characteristic (causing peaks in d^2I/dV^2) with each peak corresponding to the subband thresholds in the quantum well. The experiments were done at fixed magnetic field $B=11$ T, for which the emitter state of the resonant tunneling device is primarily the $n=0$ Landau level, so that the observed peaks were only due to quantum-well states with subband quantum number p and Landau index $n=0$, as selection rules prohibit tunneling to other Landau levels. Typically of order 20, such resonance peaks (subbands) were observed over the interval zero to one volt. However, when the magnetic field was tilted by a substantial amount ($\theta > 20°$), Fromhold and co-workers[10] found that in certain voltage intervals the number of tunneling resonances would abruptly increase, indicating the presence of tunneling processes that could not be explained by the subband structure of the well at $\theta = 0$. They interpreted these new peaks in terms of density-of-states oscillations associated semiclassically with the short periodic orbits of the well, specifically those that collide with both the emitter and collector barriers. Numerical integration of the classical equations of motion revealed a number of relevant periodic orbits and that in most of the voltage range at $B = 11$ T these orbits were unstable fixed points of the classical Poincaré map in an almost completely chaotic phase space. It was found that the spacing of the new resonances in voltage was consistent with the period of the orbits identified, as was their appearance at particular values of the magnetic field. In more recent work those authors[11] have emphasized that in many cases these oscillations should be interpreted as arising from individual electron eigenstates in the well that concentrate on the relevant classical periodic orbit (the ''scarred'' wave functions), and not by the level clustering normally associated with the DOS oscillations given by Gutzwiller's trace formula. Most of this work was done at high magnetic field and large tilt angles such that the classical dynamics is almost completely chaotic.

Another important series of experiments[12] looked at the *I-V* peaks in the entire (plane) parameter space of magnetic field and voltage, varying the tilt from $\theta = 0$ to $\theta = 45°$ in small increments so that the resonance structure could be carefully analyzed in the transition regime between chaos and integrability. They found a complicated pattern of peak doubling and peak tripling in various regions of the *B-V* plane, which extended to much lower magnetic field than previously reported. Such experiments are particularly interesting from the theoretical point of view because, as discussed below, classically the system is undergoing a transition to chaos as a function of continuous parameters (θ, B, V). In our view no quantum system of comparable controllability existed previously for the study of the quantum manifestations of the *transition* to chaos with its associated KAM (Kolmogorov-Arnold-Moser) behavior in phase space.[13]

In this paper we will lay the groundwork for a detailed semiclassical theory of these experiments by developing a systematic theory of the relevant classical periodic orbits. The complete basis of such a semiclassical theory did not exist until recently, since no semiclassical formula for the resonant tunneling current was known. Specifically, although the previous work on scars[11] and on scaled spectra[14,15] indicated the crucial role of periodic orbits within the well, it was unclear how to derive a formula in which the contribution of the well wave functions was expressed entirely in terms of periodic orbit properties in the well. We have recently derived such a formula,[16] and using the results of this work, have shown that it can explain qualitatively and quantitatively many aspects of the experimental data of Ref. 12.

A key property of the experimental system that is exploited in our derivation is that the tunneling is sequential. An electron tunnels into the well from the emitter, gains kinetic energy under the high voltage across the well, and collides with the collector barrier. After several such collisions in the well, the electron begins to lose this energy by optic phonon emission, and only tunnels out after of order one hundred collisions. Therefore the tunneling resonances are substantially broadened and only are sensitive to structure in the DOS on energy scales $> \hbar / \tau_{\rm opt} \sim 5$ meV. Under such circumstances the system may be treated by the Bardeen tunneling Hamiltonian formalism,[17] which expresses the tunneling current in terms of wave functions of the isolated well, which may then be reexpressed in terms of the semiclassical Green function, and ultimately[16] in terms of periodic orbit (PO) properties. We find for the oscillatory part of the tunneling current:

$$w_{\rm osc} = {\rm Re} \sum_{\mu} A_{\mu} \exp(-T_{\mu}/\tau_{\rm opt}) \exp\left(i \frac{S_{\mu}}{\hbar} - \frac{\pi n_{\mu}}{2} \right), \quad (1)$$

where $w_{\rm osc}$ is the oscillatory part of the tunneling rate from the emitter to the well per unit time, the summation is carrier out over various primitive periodic orbits in the well reaching the emitter wall and their repetitions, and the amplitude

$$A_{\mu} = \int dy \int dp_y f_W^{(e)}(y, p_y) \frac{16 p_z^{\mu}}{m^* \sqrt{|m_{11}^{\mu} + m_{22}^{\mu} + 2|}} \exp\left(\frac{2i}{\hbar} \frac{m_{21}^{\mu}(y - y_m u)^2 + (m_{22}^{\mu} - m_{11}^{\mu})(y - y_{\mu})(p_y - p_y^{\mu}) - m_{12}^{\mu}(p_y - p_y^{\mu})^2}{(m_{11}^{\mu} + m_{22}^{\mu} + 2)} \right), \quad (2)$$

where $\mathbf{p}^{\mu}$ and y_{μ} is the electron momentum and coordinate at the point of collision, S_{μ}, T_{μ}, and $(m)_{ij}$ are, respectively, the action, the period and the monodromy matrix[3] of the periodic orbit, and m^* is the effective mass of the electron. The distribution function $f_W^{(e)}(y, p_y)$ of the electrons injected into the well, is defined as the Wigner transform of the isolated emitter wave function, calculated at the plane of the barrier.

The level-broadening in the well due to optic phonon emission (which is represented by the term $\exp(-T_{\mu}/\tau_{\rm opt})$ in the tunneling formula (1), implies that only the shorter PO's, corresponding to ~ 5 or fewer collisions with the barriers, will give resolvable structure in the experiments we analyze. In this paper we focus on the the classical mechanics of these short periodic orbits.

Although the work of Fromhold and co-workers had identified several important periodic orbits in the classical mechanics, they had not provided a model of the global phase-space structure as the system undergoes the transition to chaos. Shepelyansky and Stone[18] developed such a model by reducing the dynamics to a two-dimensional effective map which, in the limit where the emitter state energy is negligible, is equivalent to the Chirikov standard map. This limit amounts to replacing the double-barrier system with a single-barrier model since the injected electron does not have enough energy to climb the potential hill and collide with the emitter barrier. In this limit, for fixed θ, the dynamics is controlled by a single chaos parameter $\beta=2v_0B/E$ where B,E are the magnetic, electric fields and $\varepsilon_0=m^*v_0^2/2$ is the total injection energy of the electron. Since for much of the experimental parameter range $eV\approx\varepsilon_0$, Shepelyansky and Stone argued that the classical mechanics should be approximately constant along parabolas $V=8ed^2m^{*-1}\beta^{-2}B^2$ (d is the distance between the barriers) and estimated the value of β at which global chaos occurs using the Chirikov resonance overlap criterion.[19] They pointed out that the first appearance of additional resonance peaks at $B\approx5$ T, $\theta=11°$ appeared to be due to the bifurcation of the main period-one orbit; however, they did not analyze these bifurcations further at the time.

In this paper we provide a detailed analysis of the classical mechanics of these bifurcations both within the single-barrier model (SBM) and the more accurate double-barrier model (DBM). The essential physics of these bifurcations is the nonlinear (classical) resonance between the cyclotron rotation and the longitudinal ''bouncing ball'' motion in the well, which are coupled for $\theta\neq0$. These resonances lead to bifurcations of the main period-one orbit, which we shall refer to as the ''traversing orbit'' (TO), since near resonance this orbit is not isolated and new orbits can be born without violating the Poincaré index conservation theorem.[20] These nonlinear resonances have relatively simple analytic properties due to the fact that the cyclotron frequency is independent of the energy, and these basic properties are captured by the SBM, which describes a standard, smooth KAM transition to chaos. Therefore, in our view, the conjecture of Refs. 18 and 12, relating peak doubling and tripling to period-two and period-three bifurcations of the traversing orbit using the SBM, is qualitatively correct. However, we now understand that the DBM is not a standard KAM system, since the discontinuity in the dynamics between orbits that reach and those that do not reach the emitter barrier violates the assumptions of this theory. The DBM then generates some new physics in the bifurcation theory which is described in detail in Sec. IV below. Specifically we find that period-N bifurcations arise in families related according to certain topological rules. Certain of the bifurcations, which we term *cusp bifurcations*, violate standard principles of bifurcation theory due to the discontinuity just mentioned. One member of each family participates in the period-N bifurcation of the traversing orbit, but the corresponding orbit is often not the one responsible for the appearance of multiple peaks in the experimental data. This point has been made earlier,[21,22] but without recognition of the bifurcation trees connecting all of these orbits.[23]

Below we derive an exact analytic expression for the period and stability of the traversing orbit in both the SBM and DBM, which allows us to locate precisely the bifurcation points for all values of B,V,θ. The existence of such exact analytic formulas for nontrivial periodic orbits of a Hamiltonian in the mixed regime is to our knowledge unique to this system and suggests its value as a computationally tractable example of bifurcation theory and the approach to Hamiltonian chaos. A further benefit of the stability analysis is that we are able to explain the anomalously strong scarring of wave functions found previously;[11] these implications are described briefly below, and in detail elsewhere.[24]

First, we briefly discuss qualitatively the origin of classical chaos in this system, which we shall refer to as the ''tilted well.'' At zero tilt angle ($\theta=0$) the acceleration along the electric field $\mathbf{E}=E\hat{\mathbf{z}}$ normal to the barriers and the transverse cyclotron motion decouple and are integrable. Collisions with the barriers reverse the longitudinal component of momentum ($v_z\rightarrow-v_z$) and do not transfer energy between the cyclotron and longitudinal motion. Once the B field is tilted, so that $\mathbf{B}=B\cos\theta\hat{z}+\sin\theta\hat{y}$, between collisions the electron executes cyclotron motion around the $\hat{\mathbf{B}}$ direction, with a superimposed drift velocity $\mathbf{v}_d=(E/B)\sin\theta\hat{\mathbf{x}}$, and accelerates *along* $\hat{\mathbf{B}}$ due to the component $\mathbf{E}\cdot\hat{\mathbf{B}}=E\cos(\theta)$. This motion is still integrable. However, now collisions with the barriers in general *do* mix the cyclotron and longitudinal energies $\varepsilon_c,\varepsilon_L$ and make the total dynamics nonintegrable. (When $\theta\neq0$ longitudinal will mean parallel to the magnetic field direction $\hat{\mathbf{B}}$, and transverse will refer to the plane perpendicular to $\hat{\mathbf{B}}$.) The amount of energy exchange $\Delta\varepsilon=\varepsilon_L-\varepsilon_c$ depends sensitively on the *phase* of the cyclotron rotation at impact. For example, we shall see below that when the phase is such that the velocity falls precisely in the x-z plane there is no energy exchange ($\Delta\varepsilon=0$), and periodic orbits with this property will be of great importance. When degrees of freedom are nonlinearly coupled so that the amount of energy exchange is determined by a rapidly varying phase, chaos is the inevitable result.[18] Since the rate of variation of the phase between collisions is $\omega_c=eB/m^*$, we expect the degree of chaos to increase with increasing B. Similarly, since the time between collisions decreases with increasing voltage, the rate of phase variation is a decreasing function of V and we expect chaos to diminish as V *increases*. This explains qualitatively the dependence of the chaos parameter $\beta\sim B/\sqrt{V}$ found by Shepelyansky and Stone.[18] To go beyond these qualitative considerations we need to perform a scaling analysis of the classical double-barrier Hamiltonian, which we will describe in the next section.

This paper is organized as follows. In Sec. II we introduce the scaled Hamiltonian, which is effectively two dimensional, and discuss the nonlinear Poincaré map it generates, recovering the limiting behavior discussed by Shepelyansky and Stone, which is equivalent to the single-barrier model. We introduce the crucial notion of nonmixing periodic orbits. In Sec. III we discuss the periodic orbit structure of the SBM, deriving analytic expressions for the period and stability of all period-one orbits. We consider the bifurcations of the traversing orbits in the SBM, enumerating the relevant period-two and period-three orbits. In Sec. IV we turn to the double-barrier model (DBM) and derive analytic formulas for the period-one orbits there. The bifurcations of the TO in the DBM are discussed and the families of period-N orbits are identified. Finally, we summarize the properties of the

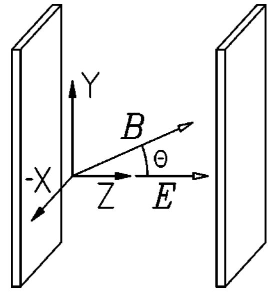

FIG. 1. Schematic of the geometry of the system with our axis conventions.

short periodic orbits and set the stage for their use to calculate the tunneling spectra semiclassically in Ref. 16.

II. SCALED DYNAMICS AND POINCARÉ MAP

A. Scaled Hamiltonian

We now define the Hamiltonian we will use for analyzing the classical mechanics. We neglect the coupling of the electrons to optic phonons within the well; we will take it into account in the semiclassical theory by introducing an appropriate level broadening. The semiclassical tunneling theory expresses the tunneling current in terms of the emitter wave function, the tunneling rate through each barrier, and the periodic orbits of electrons trapped within the well. Therefore we are only concerned with the classical mechanics within the well and can represent the barriers by infinite hard walls separated by a distance d. The z axis will be chosen normal to the barriers (parallel to the electric field $\mathbf{E}$) and with an origin such that the collector barrier is at $z=0$ and the emitter barrier is at $z=d$. The magnetic field is tilted in the (y,z) plane, $\mathbf{B}=B(\cos\theta\hat{\mathbf{z}}+\sin\theta\hat{\mathbf{y}})$—see Fig. 1. We choose a gauge where the vector potential $\mathbf{A}=[-By\cos(\theta)+Bz\sin(\theta)]\hat{\mathbf{x}}$. The Hamiltonian is

$$H=\frac{[p_x-eBy\cos(\theta)+eBz\sin(\theta)]^2}{2m^*}+\frac{p_y^2}{2m^*}+\frac{p_z^2}{2m^*}+eEz$$
$$+U(-z)+U(z-d)=\varepsilon, \tag{3}$$

where the function U $(U(z<0)=0, U(z>0)=\infty)$ represents the infinite hard walls at $z=0,d$.

The Hamiltonian (3) involves four variable experimental parameters: B, E, θ, and d. It is of great convenience to rescale the variables in Eq. (3) so as to express the dynamics generated by this Hamiltonian in terms of the minimum number of independent parameters. This will simplify the analysis of the periodic orbits and also predict scaling relations relevant to the experimental data. We present a rescaling below that is most useful for a periodic orbit theory of both the single-barrier and double-barrier models. It is a natural extension of the simpler scaling introduced by Shepelyansky and Stone.[18] An alternative scaling which applies to the DBM has been introduced by Monteiro and co-workers.[14,15]

The natural unit of time for the problem is ω_c^{-1}, where $\omega_c=eB/m^*$ is the cyclotron frequency. The barrier spacing d gives one length scale, and the only other energy-independent length scale in the problem is $l_D=v_D\omega_c^{-1}$, where $v_D=E/B$ is the drift velocity for perpendicular electric and magnetic fields (the actual drift velocity when the fields cross at angle θ is $v_d\equiv v_D\sin\theta$). For electron total energies $\varepsilon<eV=eEd$ the emitter barrier is energetically inaccessible so the length scale d is irrelevant. Since we wish to introduce a dimensionless Hamiltonian related to Eq. (3) by a canonical transformation, the scaling must be independent of energy and applicable to both the case $\varepsilon<eEd$ and $\varepsilon>eEd$. Hence we must scale all lengths by l_D.

In addition, we want to exploit all symmetries of the Hamiltonian. The Hamiltonian (3) is independent of the coordinate x and, therefore, p_x is conserved, so we can see immediately that the dynamics is two dimensional for each value of p_x. However, there is an additional symmetry related to gauge invariance: the invariance of H under all transformations of p_x and y, which keep the value of the difference $p_x-eBy\cos\theta$ unchanged. This implies that if a periodic orbit exists for one value of p_x, then an exact copy of this orbit exists for all p_x translated by the distance $\Delta y=\Delta p_x\cos\theta/eB$. Combined with the translational invariance in the x direction this means that any periodic orbits can be arbitrarily translated in the x-y plane. This is the classical analogue of the Landau-level degeneracy that is preserved in the Hamiltonian (3). We want to rescale our Hamiltonian to eliminate this classical degeneracy in p_x as well, so as to define a unique dynamics for each value of the total energy. This can be achieved by the following canonical transformation:

$$\xi=\frac{x}{l_D}-\frac{\omega_c^{-1}p_y}{m^*l_D\cos\theta},\quad \eta=\frac{y}{l_D}-\frac{\omega_c^{-1}p_x}{m^*l_D\cos\theta},\quad \zeta=z/l_D,$$

$$p_\xi=\frac{\omega_c^{-1}}{m^*l_D}p_x,\quad p_\eta=\frac{\omega_c^{-1}}{m^*l_D}p_y,\quad p_\zeta=\frac{\omega_c^{-1}}{m^*l_D}p_z,$$

$$\tau=\omega_c t, \tag{4}$$

which leads to the dimensionless Hamiltonian with two degrees of freedom:

$$H_{\rm eff}=\frac{p_\eta^2+p_\zeta^2}{2}+\tfrac{1}{2}(\eta\cos\theta-\zeta\sin\theta)^2+\zeta+U(-\zeta)$$
$$+U\left(\zeta-\frac{d}{l_D}\right), \tag{5}$$

$$=\frac{\varepsilon}{\varepsilon_D} \tag{6}$$

where rescaled energy is measured in units of the "drift energy" $\varepsilon_D=mv_D^2$ and may be rewritten as

$$\frac{\varepsilon}{\varepsilon_D}=\frac{v_0^2B^2}{2E^2}\equiv\frac{\beta^2}{8}.$$

Note that both the coordinate ξ *and* the momentum p_ξ are absent in the scaled Hamiltonian, which is hence truly two dimensional.

B. DBM vs SBM: γ parameter

The only dependence on the barrier-spacing d in the scaled Hamiltonian is through the term $U(\zeta - d/l_D)$ representing the emitter barrier. As noted, when the total energy of the electron is less than the potential drop eEd across the well, the electron cannot reach the emitter barrier, and the term $U(\zeta - d/l_D)$ can be removed from the equation (5). In this case, for fixed θ, the dynamics is uniquely defined by the value of the scaled energy, $\varepsilon/\varepsilon_D \equiv \beta^2/8$. This case corresponds to the single-barrier model studied by Shepelyansky and Stone,[18] who first showed that the dynamics of the SBM at fixed θ depends only on the parameter $\beta \equiv 2v_0 B/E$.

When $\varepsilon > eEd$, the electron can collide with the emitter barrier and the classical motion of the electron in such a case depends essentially on *both* d/l_D and β, leading to a more complicated and interesting dynamics. Since the crossover between these two regimes is determined by the condition $\gamma \equiv \varepsilon/eEd = 1$, we reexpress the parameter d/l_D in Eq. (5) in terms of the dimensionless parameters β, γ: $d/l_D = \beta^2/(8\gamma)$, so that the dynamics in the DBM is determined by the values of β, γ. This is particularly convenient because in experiments the ratio of the emitter state energy to the applied voltage is approximately unchanged, so γ is approximately constant over the B-V parameter space. Therefore both the dynamics of the SBM *and* the DBM can be fully analyzed at fixed θ by varying a single dimensionless parameter β. This is how we will proceed in the remainder of this work.

Before making any further analysis of the dynamics we note that there is one completely general prediction that follows from the scaled Hamiltonian of Eq. (5) if γ is constant. We can write

$$\beta^2 = \frac{8\gamma eV}{\varepsilon_D} = \frac{8\gamma e d^2}{m^*}\frac{B^2}{V}, \tag{7}$$

which implies that for a given θ *the classical mechanics is constant along parabolic boundaries in the B-V plane:* $V = (8\gamma e d^2/m^*\beta^2)B^2$. This is true of the exact dynamics of the double-barrier model as long as γ is constant and the variation of effective mass with injection energy is negligible.

C. Poincaré map

In order to analyze the two-dimensional Hamiltonian dynamics of the canonical coordinates $(\eta, p_\eta; \zeta, p_\zeta)$ we use the Poincaré surface of section (SOS) method, which is standard in nonlinear dynamics.[3,25,26] For fixed values of β and γ the classical trajectories in this four-dimensional phase space lie on a three-dimensional surface determined by energy conservation. When $\theta \neq 0$ the system is nonintegrable, there is no additional constant of motion other than the energy, and there exist chaotic trajectories which cover a finite fraction of this three-dimensional surface. To define the stability matrix for the periodic orbits and also to better visualize the phase-space structure we plot the behavior of a set of trajectories on a two-dimensional cross section of this surface. The motion of an electron in the tilted well is bounded and all trajectories collide eventually with the collector barrier at $\zeta = 0$. Therefore it is convenient to choose the cross section to be the plane (p_η, η) when $\zeta = 0$ (p_ζ being then fixed by energy conservation). If an initial condition is chosen on this plane then Hamilton's equations of motion can be used to obtain the values of (η, p_η), when the trajectory again passes through the plane $\zeta = 0$. This procedure defines a Poincaré map for the tilted well (other choices are possible, e.g., the emitter barrier map at $\zeta = d/l_D$ and may be used below).

$$\eta_{n+1} = \Phi_q(\eta_n, (p_\eta)_n),$$

$$(p_\eta)_{n+1} = \Phi_p(\eta_n, (p_\eta)_n). \tag{8}$$

Since every orbit reaches the collector barrier, *every* periodic orbit of the Hamiltonian (5) corresponds to either a fixed point of the Poincaré map (period-one orbits) or to a fixed point of the Nth iteration of the Poincaré map (period-N orbits).

Note that the coordinates η and momentum p_η are proportional to the x and y components of the *velocity* of the electron in the original coordinate system:

$$v_x = -l_D \cos\theta \omega_c \eta,$$

$$v_y = l_D \omega_c p_\eta. \tag{9}$$

This property allows us to relate the Poincaré map (8) in the coordinates (η, p_η) to an equivalent Poincaré map in more familiar coordinates $(v_x/v_0, v_y/v_0) \equiv (\tilde{v}_x, \tilde{v}_y)$, which describes the evolution of the velocity components of the electron in the plane perpendicular to the collector barrier:

$$(\tilde{v}_x)_{n+1} = \Phi_x((\tilde{v}_x)_n, (\tilde{v}_y)_n),$$

$$(\tilde{v}_y)_{n+1} = \Phi_y((\tilde{v}_x)_n, (\tilde{v}_y)_n), \tag{10}$$

where the relations between Φ_x, Φ_y and Φ_q, Φ_p follow from Eqs. (9) and (8).

Note that we have scaled the velocities by the maximum allowed velocity v_0 so that the values of this Poincaré map will be contained within the unit circle, independent of the energy [this would not be true of the variables (η, p_η) as the size of the energetically allowed region of the plane varies with the scaled energy $\beta^2/8$]. Although the variables (η, p_η) were most convenient for discussions of scaling, we will use the energy-scaled velocity map (10) henceforth, since it is easiest to interpret and compare for varying β values.

A plot of the Poincaré map (10), which is called SOS, is generated by choosing a grid of initial conditions in the plane $(v_x/v_0, v_y/v_0)$ corresponding to a particular value of β and iterating the map many times for each initial condition. Period-N stable orbits appear as ''chains'' of N ''islands;'' whereas period-N unstable orbits will be embedded in the chaotic layers between the islands[26] and are not evident to the (untrained) eye. In Fig. 2 we show several examples of the collector barrier SOS as β is increased for fixed $\gamma = 1.17$ (which corresponds to the approximate value in the relevant experiments[12]).

When $\theta = 0$ the squared distance of a point in the SOS from the origin is proportional to the cyclotron energy, which is conserved, so each trajectory must lie on a circle

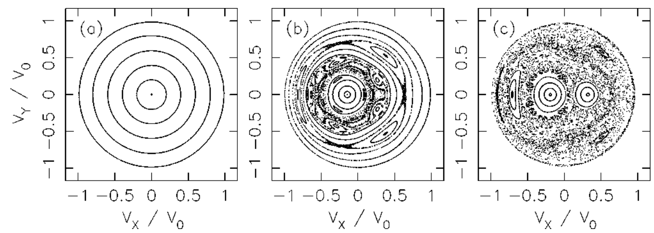

FIG. 2. Three Poincaré surfaces of section for experimentally relevant $\gamma=1.17$ at (a) $\theta=0°$, $\beta=2$, (b) $\theta=20°$, $\beta=3.2$, (c) $\theta=20°$, $\beta=4$.

[see Fig. 2(a)]. When $\theta\neq 0$ [Fig. 2(b)] we immediately see the appearance of stable islands and chaotic layers, coexisting with slightly distorted circular curves that represent the unbroken tori according to the standard KAM scenario.[25] For larger β [Fig. 2(c)] no KAM curves survive and the entire SOS is chaotic except for a few surviving stable islands, which however typically represent the features of most importance for the experimental tunneling oscillations.

We now undertake a more explicit determination of the properties of the Poincaré map for the tilted well. To calculate the functions Φ_p and Φ_q of the Poincaré map, one has first to analyze the motion of the electron between collisions. This motion is integrable and is most easily represented in a frame of reference [denoted by (x',y',z')], rotated by the tilt angle θ around the x axis, so that z' is parallel to the direction of the magnetic field:

$$x'=x,$$

$$y'=y\cos\theta-z\sin\theta,$$

$$z'=y\sin\theta+z\cos\theta.$$

In this frame of reference the motion of the electron in the (x',y') plane between collisions is a superposition of the cyclotron rotation with the frequency $\omega_c\equiv 2\pi/T_c$ and a uniform drift along x' with the velocity $v_d=E\sin\theta/B\equiv v_D\sin\theta$, while the longitudinal motion is a uniform acceleration:

$$v_{x'}(\tau)=v_c\cos(\phi^0+\tau)-v_d,$$

$$v_{y'}(\tau)=v_c\sin(\phi^0+\tau),$$

$$v_{z'}=v_{z'}^0-e\frac{E\cos\theta}{m}t=v_{z'}^0-l_D\cos\theta\,\omega_c\tau, \tag{11}$$

where v_c is the cyclotron velocity (which remains constant between collisions) and ϕ^0 is the initial phase of the cyclotron rotation.

The energies associated with the transverse (cyclotron) and longitudinal motion are separately conserved between collisions. For $\theta\neq 0$ the cyclotron and longitudinal motions get mixed by the collisions with the barriers:[18]

$$\overline{v_{z'}}=-\cos(2\theta)v_{z'}+\sin(2\theta)v_{y'},$$

$$\overline{v_{y'}}=\sin(2\theta)v_{z'}+\cos(2\theta)v_{y'},$$

$$\overline{v_{x'}}=v_{x'}, \tag{12}$$

where $\mathbf{v}$ and $\overline{\mathbf{v}}$ are the velocities immediately before and after collision, respectively. This transformation is equivalent to a clockwise rotation of the velocity vector by 2θ in the $(y'$-$z')$ plane, followed by a reflection $v_{z'}\rightarrow -v_{z'}$; hence it leaves no vector in this plane invariant (for $\theta\neq 0$). Therefore, generically there *is* exchange of kinetic energy between the longitudinal and cyclotron motion at each collision,

$$\delta\varepsilon_{L\leftrightarrow c}=\frac{m}{2}(v_{z'}-\overline{v_{z'}})^2, \tag{13}$$

and the dynamics is nonintegrable.

Note that it is *possible* to have zero energy exchange upon collision for $\theta\neq 0$. The condition for this is simply that $v_y=0$ at collision, i.e., the cyclotron phase is such that the instantaneous motion is in the x-z plane. The reason that no energy is exchanged in this case is that the impulse at collision is purely in the z direction and reverses this component of velocity leaving v_x and v_y unchanged. If $v_y=0$ at the time of collision then $v_{z'}=v_z\cos\theta\rightarrow\overline{v_{z'}}=-v_z\cos\theta=-v_{z'}$ and the longitudinal kinetic energy is conserved. Stable period-one orbits with $v_y=0$ ($p_\eta=0$) are visible in both Figs. 2(b),2(c). We refer to these as *nonmixing* orbits since they involve no energy exchange; they will play a fundamental role in the periodic orbit theory developed below.

The transformation equations for $\mathbf{v}'$ due to collisions at the emitter barrier are identical to Eq. (12). As we shall see below, it is useful to consider the dynamics in yet a third frame of reference that is parallel to the primed frame, but is moving with the drift velocity v_d in the x' direction. In this moving frame the transverse motion is pure cyclotron rotation and each iteration of the Poincaré map is just a pair of noncommuting orthogonal transformations of the velocity: first the continuous cyclotron rotation around the z' axis, followed by the instantaneous rotation/reflection around the x' axis. Since the latter is known explicitly [Eq. (12)], to get an explicit formula for the Poincaré map what is needed is an expression for the increment in the cyclotron phase between collisions. However, there is no simple general formula for this phase increment for $\gamma>1$ because after a collision with the collector barrier an orbit may or may not have enough longitudinal energy to collide with the emitter barrier before its next collision with the collector. Since $v_{y'}$ changes discontinuously in a collision, the cyclotron phase increment will change discontinuously due to the emitter collision. If one varies the initial conditions of a trajectory so that it ceases colliding with emitter barrier in the next iteration of the map, one can show that the phase jump goes to zero as the impulse at the emitter goes to zero (i.e., as v_z at collision goes to zero), but its derivative is discontinuous. Hence, in general the Poincaré map for $\gamma>1$ does not have continuous derivatives everywhere on the surface of section. As a consequence the stability matrix of periodic orbits for the exact map for $\gamma>1$ is not always defined. This has significant and novel consequences for the behavior of periodic orbits in the DBM: these can vanish without reaching marginal stability in a new kind of bifurcation we will refer to as a *cusp bifurcation* because such a bifurcation generates a cusp in the bifurcation diagram.[27] We shall return to this in detail below.

As a result of this discontinuous behavior we can only present a simple explicit form of the Poincaré map in certain limiting cases. The simplest of these, previously analyzed by Shepelyansky and Stone,[18] is when $\gamma<1(\varepsilon<eV)$, in which case no orbit reaches the emitter barrier and classically the problem is equivalent to the motion of an electron in an infinite triangular well in a tilted B field. We now briefly review this limit.

D. Single-barrier model

When $\gamma\leqslant 1$, the cyclotron phase increment between collisions with the collector barrier is $\omega_c t_0$, where t_0 is the time it takes the electron launched ''upwards'' after the collision in the effective electric field, $\mathbf{E}\cos\theta$, to fall back down and hit the collector. The resulting Poincaré map takes the form

$$\Phi_x(\tilde{v}_x,\tilde{v}_y)=\mathcal{V}_x(\tilde{v}_x,\tilde{v}_y,\tilde{v}_z;\omega_c t_0),$$

$$\Phi_y(\tilde{v}_x,\tilde{v}_y)=\mathcal{V}_y(\tilde{v}_x,\tilde{v}_y,\tilde{v}_z;\omega_c t_0), \tag{14}$$

where

$$\mathcal{V}_x(\tilde{v}_x,\tilde{v}_y,\tilde{v}_z;\tau)=\tilde{v}_x\cos(\tau)-\tilde{v}_y\cos\theta\sin(\tau)+\tilde{v}_z\sin\theta\sin(\tau)$$
$$-(2/\beta)\sin\theta[1-\cos(\tau)],$$

$$\mathcal{V}_y(\tilde{v}_x,\tilde{v}_y,\tilde{v}_z;\tau)=\tilde{v}_x\cos\theta\sin(\tau)+\tilde{v}_y[\cos^2\theta\cos(\tau)+\sin^2\theta]$$
$$+\tilde{v}_z\sin\theta\cos\theta[1-\cos(\tau)]$$
$$+(2/\beta)\sin\theta\cos\theta[\sin(\tau)-\tau], \tag{15}$$

the scaled velocity $\tilde{\mathbf{v}}\equiv\mathbf{v}/v_0$ [with $\tilde{v}_z(\tilde{v}_x,\tilde{v}_y)\equiv\sqrt{1-\tilde{v}_x^2-\tilde{v}_y^2}>0$] and the time interval $t_0(\tilde{v}_x,\tilde{v}_y)$ between successive collisions of the electron with the collector barrier is the first positive root of the equation:

$$0=z(t_0)\equiv\frac{v_0\mathcal{Z}(\tilde{v}_x,\tilde{v}_y,\tilde{v}_z;\omega_c t_0)}{\omega_c}, \tag{16}$$

where the function $\mathcal{Z}(\tilde{v}_x,\tilde{v}_y,\tilde{v}_z;\tau)$ is defined as

$$\mathcal{Z}(\tilde{v}_x,\tilde{v}_y,\tilde{v}_z;\tau)$$
$$=-\tilde{v}_x\sin\theta[1-\cos(\tau)]+\tilde{v}_y\sin\theta\cos\theta[\tau-\sin(\tau)]$$
$$+\tilde{v}_z[\tau\cos^2\theta+\sin^2\theta\sin(\tau)]$$
$$-(2/\beta)\left(\sin^2\theta[1-\cos(\tau)]+\cos^2\theta\frac{\tau^2}{2}\right). \tag{17}$$

If $\omega_c T\gg 1$, an approximate root is found easily,

$$T=\frac{\beta\tilde{v}_{z'}}{\cos\theta}. \tag{18}$$

In this approximation the map when transformed to the (x',y',z') coordinates becomes identical[18] to the kicked-top map introduced by Haake.[28,29]

As is indicated by the numerical analysis of both the kicked-top map and of the exact mapping (14), the KAM transition to chaos takes place when $\theta\beta\sim 1$. We therefore take the limit $\beta\gg 1$ and $\theta\ll 1$. In this case both the kicked-top map and the exact map (14) in the vicinity of a particular value of $\tilde{v}_{z'}=\tilde{v}'$ can be expressed precisely in the form of a local standard map (kicked rotor),[19,25]

$$I_{n+1}=I_n+K\sin\phi_{n+1},$$

$$\phi_{n+1}=\phi_n+I_n, \tag{19}$$

where

$$I_n=\beta\tilde{v}_{z'},$$

$$K=2\theta\beta\sqrt{1-(\tilde{v}')^2}, \tag{20}$$

and ϕ is the phase of the cyclotron rotation.

The map is called local because the kick strength varies with $v_{z'}$, so that the chaos boundary, given by the condition[19] $K\approx 1$ varies with $v_{z'}$. The resulting condition for chaos as an explicit function of all system parameters is[18]

$$B^2>\frac{mE\varepsilon}{32e\theta^2\varepsilon_c}, \tag{21}$$

where $\varepsilon_c\equiv\varepsilon(1-(\tilde{v}')^2)$ is the instantaneous energy of the cyclotron motion.

Although the estimate Eq. (21) was obtained only in the limiting case $\theta\ll 1$ and $\beta\gg 1$, it does predict the correct behavior of the exact mapping (14) for the SBM. Qualitatively it predicts that chaos increases with increasing magnetic field and energy and with decreasing electric field and quantitatively the condition given by Eq. (21) is in good agreement with the onset of complete energy exchange between the cyclotron and longitudinal motion as determined from simulations of the exact map.[18]

E. Double-barrier model

When $\gamma=\varepsilon/eV>1$, the electron can retain enough longitudinal energy on collision with the collector barrier to reach the emitter wall, although it need not do so. If we regard the coordinates $(\tilde{v}_x,\tilde{v}_y)$ in the SOS as initial conditions for the next segment of the trajectory, we may partition the SOS into inner and outer regions. Initial conditions $(\tilde{v}_x,\tilde{v}_y)$ in the inner region will define all trajectories that collide with the emitter before their next collision with the collector. For such initial conditions the equation

$$z(t)\equiv\frac{v_0\mathcal{Z}(\tilde{v}_x,\tilde{v}_y,\tilde{v}_z;\omega_c t)}{\omega_c}=d\equiv\frac{v_0}{\omega_c}\frac{\beta}{4\gamma}, \tag{22}$$

where the function $\mathcal{Z}$ was defined in Eq. (17), must have a positive root $t=t^{\uparrow}$, which corresponds to the time interval to the next collision with the emitter barrier.

For initial conditions in the outer region Eq. (22) has no positive roots, the electron does not reach the emitter barrier before the next collision with the collector barrier, and its trajectory is exactly the same as in the SBM for this iteration of the map. Hence the Poincaré map is still given by the expression (14).

The ''critical boundary'' between the two regions is the curve $(\tilde{v}_x^{(c)},\tilde{v}_y^{(c)})$, such that the electron launched from the collector barrier with the velocity $\mathbf{v}=v_0(\tilde{v}_x^c,\tilde{v}_y^c,\tilde{v}_z^c)$, will

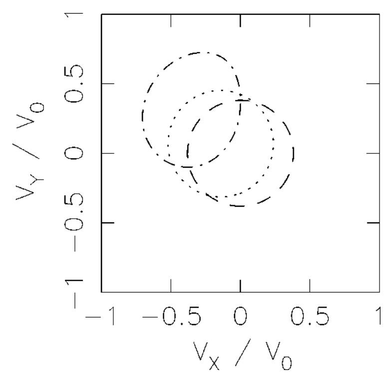

FIG. 3. The critical boundary, separating initial conditions such that the electron will reach the emitter barrier before the next collision with the collector wall (region enclosed by the critical boundary) from those when the electron returns to the collector wall without striking the emitter barrier (the region outside the critical boundary). $\gamma=1.17$, and (a) $\theta=0°$ (dashed line), (b) $\theta=15°$, $\beta=3$ (dotted line), (c) $\theta=30°$, $\beta=5$ (dashed-dotted line).

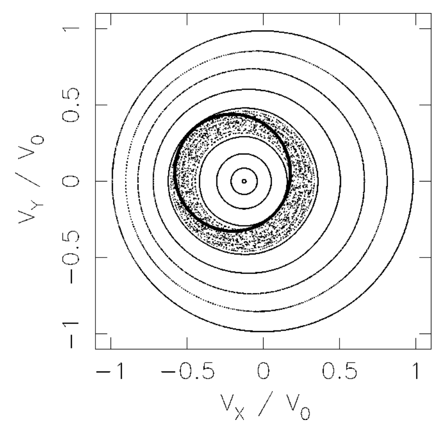

FIG. 4. The Poincaré surface of section for $\gamma=1.17$, and $\beta=2$, $\theta=30°$. The chaotic region near the critical boundary (thick solid line) is the ''chaotic halo,'' created by the nonanalyticity of the map.

reach the emitter wall with the component of the total velocity perpendicular to the plane of the barrier equal to zero. For $\theta=0$ the critical boundary is a circle given by the equation

$$\tilde{v}_x^2+\tilde{v}_y^2=1-1/\gamma\equiv\frac{\varepsilon-eV}{\varepsilon}. \tag{23}$$

In Fig. 3 we show a few examples of the ''critical boundary'' for different values of β and γ. It is important to realize that in general trajectories can cross the critical boundary and indeed for large chaos parameter almost all trajectories do. However, knowledge of the critical boundary is useful for formulating the Poincaré map of the DBM.

For $(\tilde{v}_x,\tilde{v}_y)$ outside the critical boundary, the next iteration of the Poincaré map does not involve the collision with the emitter barrier, and the Poincaré map is therefore still given by Eq. (14), as in the single-barrier model.

When $(\tilde{v}_x,\tilde{v}_y)$ is inside the critical boundary, then the Poincaré map is given by

$$\Phi_x(\tilde{v}_x,\tilde{v}_y)=\mathcal{V}_x(\tilde{v}_x^e,\tilde{v}_y^e,\tilde{v}_z^e;\omega_c t^{\downarrow}),$$

$$\Phi_y(\tilde{v}_x,\tilde{v}_y)=\mathcal{V}_y(\tilde{v}_x^e,\tilde{v}_y^e,\tilde{v}_z^e;\omega_c t^{\downarrow}), \tag{24}$$

where $\tilde{\mathbf{v}}_e$ is the scaled velocity immediately after collision with the emitter barrier and can be obtained as

$$\tilde{v}_x^e=\mathcal{V}_x(\tilde{v}_x,\tilde{v}_y,\tilde{v}_z;\omega_c t^{\uparrow}),$$

$$\tilde{v}_y^e=\mathcal{V}_x(\tilde{v}_x,\tilde{v}_y,\tilde{v}_z;\omega_c t^{\uparrow}),$$

$$\tilde{v}_z^e=-\sqrt{1-1/\gamma-(\tilde{v}_x^e)^2-(\tilde{v}_y^e)^2}. \tag{25}$$

$t^{\uparrow}$ is defined as the time interval until the next collision with the emitter barrier and is given by the first positive root of Eq. (22), and the parameter $t^{\downarrow}$ represents the time interval between the collision with the emitter barrier and the next collision with the collector map. The value of $t^{\downarrow}$ can be obtained from the equation

$$d+\frac{v_0}{\omega_c}\mathcal{Z}(\tilde{v}_x^e,\tilde{v}_y^e,\tilde{v}_z^e;\omega_c t^{\downarrow})=0. \tag{26}$$

As noted above, an important property of the Poincaré map (24) is that it has a discontinuous derivative as the initial conditions $(\tilde{v}_x,\tilde{v}_y)$ are varied across the critical boundary. Therefore the conditions for the global validity of the KAM theorem are not satisfied by this map and the transition to chaos can be discontinuous here as in the stadium billiard.[30] However unlike the stadium billiard not all trajectories are affected by the discontinuity of the map for an arbitrarily small chaos parameter. Away from the critical boundary the map satisfies all the conditions for the existence of KAM tori and, for a small chaos parameter, in the inner and outer regions there will exist an outermost and innermost KAM torus. These two tori will define a set of trajectories that either always hit the emitter barrier (lie within the outermost KAM curve of the inner region) or always miss the barrier (lie outside the innermost KAM curve of the outer region). Between these two tori the nonanalyticity of the map is felt by the trajectories and the numerics demonstrates clearly that there are no remaining KAM curves in an annular region bounded approximately by the maximum and minimum cyclotron energies of points on the critical boundary. In this region the chaos does not appear to be associated with the separatrices corresponding to the hyperbolic fixed points as it would be for a small chaos parameter in a KAM system. The practical consequence is that one observes an anomalously large ''chaotic halo'' around the critical boundary (see Fig. 4). In this region the effective map description fails badly and only analysis of the exact map can be used. In fact, as we shall see below, many of the important short periodic orbits first appear *at* the critical boundary at a finite value of β and emerge from the chaotic halo region with increasing β. We will be able to develop an analytic theory of the simplest such orbits from the exact map.

Although the effective map based on the SBM fails in the ''halo'' region, for small chaos parameter and small θ it should work just as well in the outer region of the SOS as it does in the SBM, since here the trajectories are prevented by the innermost KAM curve from reaching the emitter and the

DBM Poincaré map is *identical* to the SBM. Since the local chaos parameter in the effective map description of the SBM is $K=2\beta\theta\sqrt{1-(\tilde{v}')^2}$ the chaos is weakest at the innermost KAM curve of the outer region (since the cyclotron energy is the smallest there) and this curve is the last in the outer region to break. The quantitative prediction for the breaking of this curve from the local standard map approximation [Eq. (19)] is in a good agreement with the exact behavior.

One may try to extend similar reasoning to the inner region of trajectories that always reach the emitter barrier. Here the effective map is clearly somewhat different because of the additional energy exchange (''kick'') at the emitter barrier. It *is* possible to obtain an effective area-preserving map for small tilt angles, which is similar to a standard map with two unequal kicks per period. However, the SOS generated by this approximation has little similarity to the exact map. This is because when the energy is almost completely longitudinal (as it is in this region of phase space) the kick strength goes to zero at leading order in the tilt angle and the effective map description fails. Note that it is precisely the periodic orbits in the inner region (which reach the emitter) that are measured in the tunneling spectrum. Thus we are particularly interested in obtaining a good description of this region of phase space and must work with the exact map described by Eqs. (24).

Fortunately, as we show below, it is possible to obtain a good theoretical understanding of the short periodic orbits in the entire phase space, including the crucial central region of the SOS, based on analysis of the exact map. In fact we are able to obtain analytic expressions for the period and stability of an infinite class of important periodic orbits for arbitrarily large values of the chaos parameter.

III. PERIODIC ORBIT THEORY (SINGLE-BARRIER MODEL)

A. Integrable behavior

Equation (1) of Sec. I gives a quantitative semiclassical formula for the tunneling current through the tilted well in terms of the contributions of different periodic orbits that connect emitter and collector barriers. Clearly these orbits can be fully described only within the framework of the double-barrier model. Nevertheless, the behavior of the periodic orbits in the DBM as a function of tilt angle and β is exceedingly complex and had not been understood systematically previously. In order to develop such a systematic understanding it is very helpful to consider the SBM, which has a similar but simpler periodic orbit structure. The similarity between the two models is easily seen by considering the limit of zero tilt angle.

When $\theta=0$, both systems are integrable and all of the periodic orbits can be divided into two groups: A *single* TO bouncing perpendicular to the barrier(s) with zero cyclotron energy and infinite families of helical orbits (HO's) with periods equal to an integer multiple of the cyclotron period $2\pi/\omega_c$. The traversing orbit corresponds to the fixed point of the Poincaré map in the center (0,0) of the surface of the section—see Fig. 2; its period is given by

$$T_{\rm TO}=\frac{\beta}{\omega_c}(\mathrm{SBM}), \tag{27}$$

$$T_{\rm TO}=\frac{\beta}{\omega_c}\left(1-\sqrt{1-\frac{1}{\gamma}}\right)(\mathrm{DBM}). \tag{28}$$

Unlike all other one-bounce orbits, the TO exists for arbitrarily small energy, since its frequency need not be in resonance with the cyclotron frequency. Since it has zero cyclotron energy its semiclassical quantization yields the states of the well with Landau index equal to zero, and hence the TO determines the subband energy spacings of the triangular (SBM) or trapezoidal (DBM) well by the semiclassical rule for integrable systems: $\Delta\varepsilon=h/T_{\rm TO}$.[12]

Due to the rotational invariance of the system at zero tilt angle all other periodic orbits in the well (in both the SBM and DBM) exist in degenerate families related by rotation around the z axis. The union of all trajectories in a family defines a torus in phase space, known as a ''resonant'' torus in the nonlinear dynamics literature[26] because the periodic motion of the two degrees of freedom are commensurate:

$$n\omega_c=k\omega_L, \tag{29}$$

where n and k are integers (which do not have a common divisor) and ω_L is the frequency of the periodic motion in the longitudinal direction. Since longitudinal and transverse motion decouple, ω_L is the frequency of the periodic motion of the uniformly accelerated electron bouncing normal to the barriers, and its value is

$$\omega_L=\frac{2\pi\omega_c}{\beta\sqrt{\tilde{\varepsilon}_L}}(\mathrm{SBM}), \tag{30}$$

$$\omega_L=\frac{2\pi\omega_c}{\beta\sqrt{\tilde{\varepsilon}_L}}\times\begin{cases}1 & \gamma\tilde{\varepsilon}_L<1\\ \left(1-\sqrt{1-\dfrac{1}{\gamma\tilde{\varepsilon}_L}}\right)^{-1} & \gamma\tilde{\varepsilon}_L\geqslant 1\end{cases}(\mathrm{DBM}), \tag{31}$$

where $\tilde{\varepsilon}_L\equiv\tilde{v}_z^2$ is the scaled longitudinal energy.

The resonance condition (29) means that any periodic orbit of a family labeled by the integers n and k collides with the collector barrier n times while making k full cyclotron rotations before retracing itself. Therefore all such orbits in real space trace out rational fractions of a helix (hence the term helical orbits) between successive collisions and have periods given by

$$T_{\rm HO}=\frac{2\pi k}{\omega_c} \tag{32}$$

for both the SBM and DBM.

A simplifying feature of these systems is that one of the oscillation periods, the cyclotron period, is independent of energy and voltage. The longitudinal period varies with both energy and voltage, going to zero as longitudinal energy tends to zero. If a family of helical orbits $\{n,k\}$ exists at a given energy, a family of the same type can be generated at a lower energy by simply removing cyclotron energy (hence reducing the cyclotron radius) until the radius of the helix shrinks to zero, at which point this ''family'' has become degenerate with the TO and ceases to exist. These degeneracy points occur then, whenever the period of the traversing orbit T_{TO} passes through the value kT_c/n, for both the SBM and DBM.

When the magnetic field is tilted the rotational symmetry around the field direction that was the origin of continuous families of helical orbits in the well is broken and *all* the resonant tori are destroyed. According to the Poincaré-Birkhoff theorem[25] each of them is replaced by an integer number of pairs of stable and unstable orbits (normally just a single pair). The degeneracy points of the untilted system, at which an $\{n,k\}$ resonant torus collapsed, evolve into n-fold bifurcations of the TO.

The reason that the periodic orbit theory of the DBM is more complicated than that of the SBM stems from two facts. (1) In the unperturbed DBM there are two distinct families of orbits for each pair $\{n,k\}$ (one which reaches the emitter and one which does not), whereas there is only one such family in the SBM. (2) These families can collapse at the critical boundary and not just by reaching degeneracy with the TO. However in all the other respects mentioned above the two models are similar, and in particular, the bifurcations near the TO, which are crucial for explaining the experimental data of Muller and co-workers,[12] are very similar in the two models. We thus begin with the simpler case of the SBM.[31]

B. Periodic orbits at $\theta=0$

As just noted, the periodic orbits at $\theta=0$ are of two types: the (usually) isolated traversing orbit and the families of helical orbits. The TO, with no cyclotron energy, has a period that is independent of magnetic field and monotonically increasing from zero with increasing energy:

$$T_{\mathrm{TO}}=\frac{2\sqrt{2m^*\varepsilon}}{eE}\equiv\frac{\beta}{\omega_c}. \tag{33}$$

For all HO's the period is finite and an integer multiple of $T_c=2\pi/\omega_c$. Thus a given family of HO's labeled by $\{n,k\}$ can only exist above the energy at which $nT_{\mathrm{TO}}=kT_c$. These thresholds are the degeneracy points discussed above. At the threshold all the energy is longitudinal ($\tilde{\varepsilon}_L=1$); together with Eqs. (29),(30) this yields

$$\beta_{\{n,k\}}=\frac{2\pi k}{n}. \tag{34}$$

Since $0\leqslant\tilde{\varepsilon}_L\leqslant1$, for values of $\beta>\beta_{\{n,k\}}$ there always exists exactly one root of the equation

$$\tilde{\varepsilon}_L(n,k)=\left(\frac{2\pi k}{\beta n}\right)^2, \tag{35}$$

where $\tilde{\varepsilon}_L=\tilde{v}_z^2$ is the *scaled* longitudinal energy. The scaled cyclotron energy for this family (resonant torus) is just $\tilde{v}_c^2=1-\tilde{\varepsilon}_L$. As the value of β is increased, the existing helical orbits gain more cyclotron energy and move away from the traversing orbit, allowing for the creation of new families of HO near the TO. We will now analyze what happens to the shorter periodic orbits as the magnetic field is tilted, beginning with the one-bounce orbits.

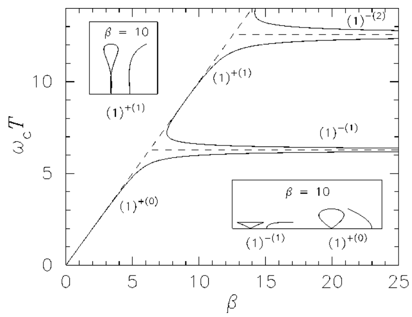

FIG. 5. Periods of one-bounce orbits as functions of β for the tilt angle $\theta=11°$. The dashed lines correspond to the periods of one-bounce orbits at zero tilt angle. The insets show the x-z and y-z projections of the three existing one-bounce orbits at $\beta=10$.

C. One-bounce orbits

1. Continuity argument

One-bounce orbits are periodic orbits that have retraced themselves between each bounce off the single barrier, i.e., they are fixed points of the first iteration of the Poincaré map. Note that different one-bounce orbits may have widely differing periods, and may for instance have periods longer than two- or three-bounce orbits. For $\theta=0$ the existing one-bounce orbits consist of the TO and all HO families with $n=1$ which are above threshold, i.e., with $k<\beta/2\pi$. The behavior of the periods of these orbits is indicated by the dashed lines in Fig. 5. Since the periods T of the HO families are fixed to be integer multiples of T_c they are independent of β when we plot ω_cT.

When the magnetic field is infinitesimally tilted, all helical families (resonant tori) are immediately destroyed and replaced by pairs of stable and unstable periodic orbits. These surviving one-bounce orbits are only infinitesimally distorted from their analogs at $\theta=0$ and by continuity the periods of these orbits are also only infinitesimally altered. For our system it is clear which orbits from each infinite family survive. For each helical family there are exactly two orbits that collide with the barrier with $v_y=0$, the condition for zero energy exchange according to Eq. (13). It is these two orbits from each family that survive. This is easily seen by recalling that longitudinal and transverse energy are separately conserved between collisions even in the tilted system, so any *one-bounce* periodic orbit for arbitrary tilt angle must also conserve these quantities during the collision. But the condition for this is just $v_y=0$, which is satisfied for the two one-bounce helical orbits from each family that hit with $v_x=\pm v_c$. By continuity these two orbits must evolve into the two surviving isolated fixed points of the map under tilting of the field. However, this tilt spoils the $y\rightarrow-y$ symmetry of the system, so these two orbits are no longer symmetry related and their periods differ, one becoming longer than kT_c and the other becoming shorter. As a result each of the horizontal lines in Fig. 5, which there represent the one-bounce HO families, splits into an upper and lower branch representing these two orbits. Moreover, for infinitesimal tilt angle one of these branches must be stable and one unstable (the lower branch is the stable one as we shall see below). Finally, there is no longer a qualitative difference between the TO and the HO's once the field is tilted. For $\theta\neq0$ the TO is required to have nonzero transverse energy in order to satisfy the $v_y=0$ condition and since it was degenerate with the $\{1,k\}$ family of HO's at $\beta=2\pi k$ it must be continuously deformable into one of the HO's near these points.

To label the single-bounce orbits, it is convenient to introduce the following notation:

$$(1)^{\pm(k)},$$

which means that it is a single-bounce periodic orbit (''1'') with the period T such that $kT_c<T<(k+1)T_c$. To distinguish the two orbits, which for $k\geqslant 1$ can satisfy this inequality, we introduce an additional index $\pm$, such that the sign ''$+$'' corresponds to the periodic orbit, which is initially stable (we use this notation in Fig. 5).

The qualitative behavior of the complete set of one-bounce orbits of the SBM follows from these continuity arguments and is shown in Fig. 5, where for definiteness we have plotted the exact analytical results of the next subsection. Note that for $\beta\neq 2\pi k$ there is always one orbit with a nearly linear variation of its period with β. This is the $(1)^{+(k)}$ orbit and *it* is the analog of the TO of the untilted system. However, near $\beta=2\pi k$ the period of each of the $(1)^{+(k)}$ orbit saturates to kT_c as it becomes primarily helical, while a new pair of orbits is born at a tangent bifurcation near $\beta=2\pi k$. One of these, the $(1)^{+(k+1)}$, takes over the role of the TO while the other, the $(1)^{-(k+1)}$, becomes the unstable partner of the helical orbit generated by the $(1)^{+(k)}$ orbit. Thus, qualitatively speaking, the system repeats itself every time β is increased by 2π. Quantitative scaling relations between the behaviors in each interval are discussed in Appendix B. Note finally that the continuity argument suggests that in the tilted system the period kT_c is forbidden for one-bounce orbits since the two surviving HO's from each resonant torus are shifted away from this value and the period of the TO can no longer cross that of the HO's as β varies; we shall prove this statement rigorously shortly.

2. Quantitative theory

We now derive exactly the periods of all one-bounce orbits for arbitrary tilt angle. We also prove that there can exist no one-bounce orbit not identified by the continuity argument given above. As just noted, it is trivial to see that all one-bounce orbits must be nonmixing (i.e., bounce with $v_y=0$) for any tilt angle. Therefore we can impose this condition in order to find all one-bounce orbits and their periods. The derivation is most easily performed in the coordinate system (x'',y'',z''), which *moves* in the direction perpendicular to B and E with the drift velocity $v_d=E\sin\theta/B$:

$$x''=x'+v_d t,$$

$$y''=y',$$

$$z''=z'. \tag{36}$$

Projected on the plane (x'',y''), the trajectory of the electron between successive collisions is a portion of a circle of radius v_c/ω_c with an angular size $\omega_c T$, where v_c is the cyclotron velocity and T is the time interval between collisions (period of the one-bounce orbit). For $T>2\pi/\omega_c$ the trajectory retraces the circle several times (see Fig. 6). Any orbit

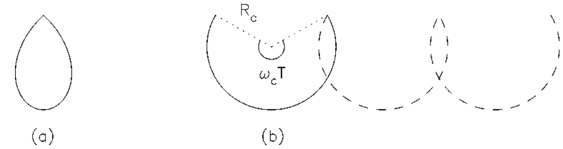

FIG. 6. A single-bounce orbit projected onto the (x',y') plane (a) and (x'',y'') plane of the ''drifting'' frame of reference (b).

that is periodic in the lab frame will not be so in the drift frame, instead the initial and the final points of the trajectory between successive collisions must be separated by the distance $\delta x''=v_d T$ (where T is the period of the orbit) and have the same value of y''. On the other hand, for one-bounce periodic orbits the distance $\delta x''$ can be expressed as (see Fig. 6)

$$\delta x''=2v_c/\omega_c\sin(\omega_c T/2),$$

so that

$$v_c=v_d\frac{\omega_c T/2}{\sin(\omega_c T/2)}$$

and at the point of collision, therefore,

$$v_{x''}|_{z=0}=v_d(\omega_c T/2)\cot(\omega_c T/2),$$

$$v_{y''}|_{z=0}=v_d(\omega_c T/2). \tag{37}$$

Since the motion along the direction of the magnetic field $\hat{\mathbf{z}}''=\hat{\mathbf{B}}$ is a uniform acceleration under the force $eE\cos\theta/m^*$, at the point of collision

$$v_{z''}=\frac{eE\cos\theta}{m^*\omega_c}\frac{\omega_c T}{2}. \tag{38}$$

Note that at the point of collision $v_y=v_{y''}\cos\theta-v_{z''}\sin\theta=0$, as expected.

Substituting v'' into the equation of energy conservation $\varepsilon=m(\mathbf{v}''-\mathbf{v}_d)^2/2$ at the barrier, we finally obtain

$$\frac{(\beta/2)^2-(\omega_c T/2)^2}{[1-(\omega_c T/2)\cot(\omega_c T/2)]^2}=\sin^2(\theta). \tag{39}$$

This is the basic equation determining the periods $T(\beta,\theta)$ for all one-bounce orbits. As $\beta\rightarrow 0$ the only solutions which exist require $T\rightarrow 0$ also, and it is easily seen by expanding the left-hand side that there is in fact only one solution for any value of θ, and this solution has $\beta=\omega_c T$ as for the TO in the unperturbed system. For any β there are no solutions with $\omega_c T=2\pi k$ (as argued above) due to the divergence of the denominator in the left-hand side at these values. If there were solutions with this value of the period, then viewed in the drift frame the orbit would be an integer number of full circles, which is one can see intuitively is impossible due to the collision (see. Fig. 6).

For $\beta\gg 2\pi k$ there are many solutions as can be easily shown graphically by plotting the single-valued function

$$\beta=\mathcal{F}\left(\sin\theta,\frac{\omega_c T}{2}\right), \tag{40}$$

where

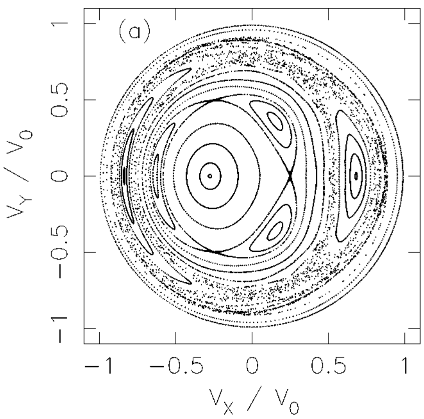

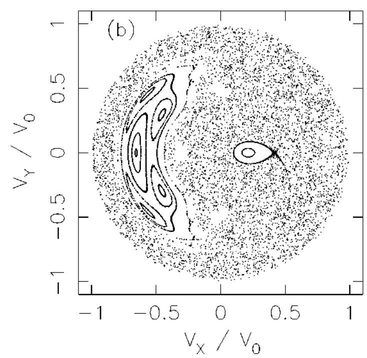

FIG. 7. Poincaré surface of section for the single-barrier model for $\theta=11°$ and (a) $\beta=5$ {as in the unperturbed system, the single-bounce orbit $[(1)^{+(0)}]$ is still surrounded by a large stable island, but has a nonzero x component of the total velocity at the collision with the collector barrier}, and (b) $\beta=7.7$ [the $(1)^{+(0)}$ orbit is still stable, but moved to the periphery of the surface of section; a tangent bifurcation has just produced two new single-bounce orbits: stable $(1)^{+(1)}$ near the origin, which now takes the role of the TO, and unstable $(1)^{-(1)}$, which produces an elongated flow pattern near the stable island of $(1)^{+(1)}$].

$$\mathcal{F}(x,y)=2\sqrt{y^2+x^2(1-y\cot y)^2} \tag{41}$$

as is done in Fig. 5.

The single solution at $\beta<2\pi k$ corresponds to the $(1)^{+(0)}$, which is a slightly deformed version of the TO; it is visible as the central island in the SOS of Fig. 7(a) with $v_y=0$ (as is required, cf. above discussion), but with now some small value of $\widetilde{v}_x$. As β is increased, this orbit gains cyclotron energy, and the corresponding fixed point moves away from the center to the left side of the surface of section. As discussed above, for $\beta>2\pi$ the period of the orbit $(1)^{+(0)}$ approaches asymptotically T_c as the majority of its energy is fed into transverse motion and it becomes a recognizable deformation of a $k=1$ helical orbit of the untilted system [see Figs. 5, 7(b)].

The two new orbits $(1)^{\pm(k)}$ that must arise by continuity in each interval appear in tangent bifurcations at thresholds given by $\beta=\beta_{\rm tb}^{(k)}$, where

$$\beta_{\rm tb}^{(k)}=\mathcal{F}(\sin\theta,\varrho_k) \tag{42}$$

and ϱ_k is the kth positive root of the equation

$$\frac{\varrho\tan\varrho}{(1-\varrho\cot\varrho)(1-2\varrho\,\mathrm{cscz}\varrho)}=\sin^2\theta.$$

This is clearly seen in the SOS of Fig. 7(b), the fixed point of the stable periodic orbit $(1)^{+(1)}$ is at the center of the stable island near the origin, whereas its unstable partner is (less obviously) visible as the elongated flow pattern at slightly larger values of v_x and $v_y=0$. The evolution of these orbits above threshold is precisely as predicted by the continuity argument above: the $(1)^{+(k)}$ initially has a period close to that of the TO before saturating to $T\approx(k+1)T_c$; whereas the $(1)^{-(k)}$ orbit immediately becomes helical with $T\approx kT_c$. We must emphasize that Eq. (39) uniquely identifies all one-bounce orbits for arbitrary θ. Thus there are no one-bounce orbits for any θ that cannot be related to one-bounce orbits of the untilted system (this is not the case for period-two and higher orbits). Hence we have a qualitative and quantitative understanding of the periods and topology of all one-bounce orbits. The next issue to address is their stability properties.

3. Stability

We define the stability of a periodic orbit in the standard manner.[25,26] The nonlinear Poincaré velocity map [Eq. (14)] is linearized for small deviations of the initial velocity from the values corresponding to the periodic orbit (fixed point of the map). This linear map is represented by a 2×2 *monodromy* matrix M_1 which has determinant one due to conservation of phase-space volume in the Hamiltonian flow. The PO is unstable if one of the eigenvalues of M_1 has a modulus larger than 1 (the other being necessarily less than 1), so that an initial deviation along the associated eigenvector grows exponentially. The PO is stable if the eigenvalues are $e^{i\phi},\phi\neq\pi,2\pi$, implying that any initial deviation will simply rotate around the fixed point. The points of marginal stability are when the eigenvalues are ±1; and by the continuity of the map M_1 must pass through marginal stability in order for the orbit to go unstable. Equivalently, if $|\mathrm{Tr}[M_1]|$ is less than 2 the orbit is stable, if greater than 2 it is unstable, and when $|\mathrm{Tr}[M_1]|=2$ it is marginally stable. There are additional general constraints. As already noted, new orbits must appear in stable-unstable pairs in what are called *tangent bifurcations* (TB's). Exactly at the point of TB the orbits are marginally stable with $\mathrm{Tr}[M_1]=2$, before the stable one moves to $\mathrm{Tr}[M_1]<2$ and the unstable one moves to $\mathrm{Tr}[M_1]>2$. Conversely, the other value for marginal stability, $\mathrm{Tr}[M_1]=-2$, corresponds to forward or backwards period-doubling bifurcations of the PO. These will be of great interest below as they are closely related to the peak-doubling transitions seen in the magnetotunneling experiments.

We can obtain the monodromy (stability) matrix for all one-bounce orbits analytically, but again will first extract its qualitative features by continuity arguments. As just noted, for infinitesimal tilt angle the TO is deformed into the $(1)^{+(k)}$ orbit in the interval $2\pi k<\beta<2\pi(k+1)$. Therefore the stability properties of the $(1)^{+(k)}$ orbits must be continuous with those of the TO in these intervals. For the case of the TO of the untilted system the monodromy matrix is trivial. The TO has $v_x=v_y=0$, therefore, a small increment of velocity in the x-y plane leaves the time interval between collisions unchanged to linear order in δv. Thus each iteration of the monodromy matrix is just rotation of this deviation vector by the angle $\omega_c T$, leading to $\mathrm{Tr}[M_1] = 2\cos(\omega_c T)$. Therefore the TO is stable at all values of β except such that $\omega_c T = m\pi$; $m = 1,2,3,\ldots$. It follows by continuity that the orbits $(1)^{+(k)}$ will be stable everywhere in the interval $2\pi k < \beta < 2\pi(k+1)$ except in infinitesimal intervals around these values.

The lowest value at which instability can occur is $\beta = 2\pi k$, but this is precisely the point of tangent bifurcation where the $(1)^{+(k)}$ and $(1)^{-(k)}$ orbits are born. Since $(1)^{+(k)}$ must evolve immediately into the analog of the (stable) TO above threshold, it must become the stable member of the pair immediately after the TB; whereas the $(1)^{-(k)}$ orbit must then be unstable. This is allowed by continuity since the $(1)^{-(k)}$ immediately evolves into the analog of the HO's, which are marginally stable for all β and can hence become unstable under infinitesimal perturbation.

Near the midway points of the relevant interval, $\beta = 2\pi(k+1/2)$, the $(1)^{+(k)}$ orbit can again go unstable, but it must immediately restabilize by continuity for higher values of β in this interval. We find that in fact all $(1)^{+(k)}$ do go unstable by period-doubling bifurcation (PDB) near this value, and for sufficiently small tilt angles they all restabilize by inverse PDB at slightly higher β.

As β increases past the value $2\pi(k+1)$ the $(1)^{+(k)}$ orbit ceases to play the role of the TO [which is taken over by the $(1)^{+(k+1)}$ orbit] and continuity alone does not determine its stability. However, from the effective map arguments of Sec. II D we know that at $\beta \geqslant 1/\theta$ the system undergoes the KAM transition to global chaos, and we therefore expect all existing periodic orbits to finally go unstable for sufficiently high values of β. In other words, for any nonzero θ the continuity argument will fail for sufficiently high $\beta \sim 1/\theta$ and new orbits can appear that have no analog in the untilted system. In fact, this second destabilization of the $(1)^{+(k)}$ orbit occurs by a PDB that creates a period-two orbit with no analog in the untilted system, as we shall see below.

As θ becomes of order unity, the β value at which global chaos sets in becomes also of order unity and we do not expect any of the $(1)^{+(k)}$ orbits to remain stable over a large interval. As already shown above, however, we can prove from Eq. (39) that a $(1)^{\pm(k)}$ pair is born by tangent bifurcation in each interval. Thus the $(1)^{+(k)}$ must be stable over some small interval for arbitrarily large k, but it need not restabilize after its first PDB. (Note that the effective map argument only predicts global chaos in the sense of no remaining KAM tori for large β; it does not prove that no stable periodic orbits can exist, and indeed we have proved the converse: stable one-bounce orbits do exist above any finite value of β.) To interpolate continuously between the limits of infinitesimal and large θ the second PDB moves continuously to lower β values until it eliminates the inverse PDB and hence eliminates the restabilization of the $(1)^{+(k)}$ PO.

To make all of these features explicit and quantitative we have derived the monodromy matrix for all single-bounce orbits. The straightforward but tedious calculation is sketched in Appendix A. We find

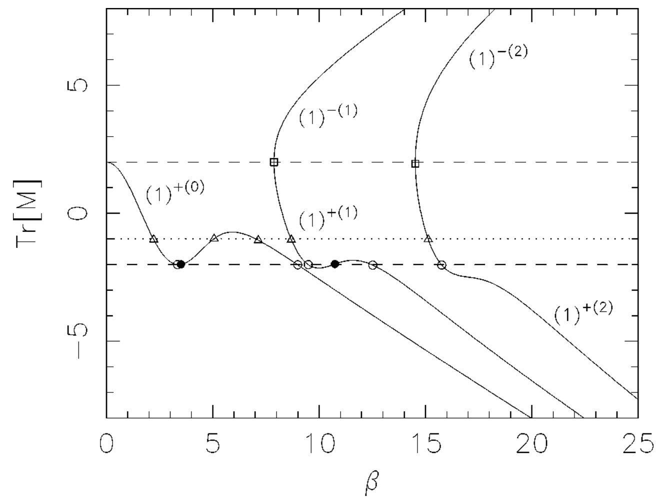

FIG. 8. Trace of the monodromy matrix for single-bounce orbits $(1)^{+(0)}$, $(1)^{+(1)}$, $(1)^{-(1)}$, $(1)^{+(2)}$, $(1)^{-(2)}$ for $\theta = 16°$. The dotted line represents the condition for the 1:3 resonance, the dashed lines show the boundaries of the stability region $|\mathrm{Tr}[M]| \leqslant 2$. Open circles show the locations of the direct PDB's, the solid circles correspond to inverse PDB's, open triangles represent 1:3 resonances, squares represent tangent bifurcations.

$$\mathrm{Tr}(M_1) = 4\cos^4(\theta)[\tan^2(\theta) + (\omega_c T/2)\cot(\omega_c T/2)] \times \{\tan^2(\theta) + \sin(\omega_c T)/(\omega_c T)\} - 2. \tag{43}$$

This equation describes precisely the stability properties of the one-bounce orbits sketched above. First, every time a new pair of roots of Eq. (39) appears with increasing β, $\mathrm{Tr}(M_1) = +2$ corresponding to a tangent bifurcation, as discussed. As β increases from this threshold one root [describing the $(1)^{-(k)}$ PO] becomes increasingly unstable with $\mathrm{Tr}(M_1) \to +\infty$. In contrast, the other root corresponding to the $(1)^{+(k)}$ orbit initially becomes stable $[\mathrm{Tr}(M_1) < 2]$ and remains so for a finite interval before going unstable at $\mathrm{Tr}(M_1) = -2$ by PDB. For sufficiently small θ, $\mathrm{Tr}(M_1)$ will pass through the value -2 twice more before tending to $-\infty$, corresponding to the restabilization and subsequent destabilization of the $(1)^{+(k)}$ predicted by the continuity arguments above. As θ increases for any fixed interval k eventually a critical angle is reached at which this restabilization ceases, just as predicted. The behavior of the $\mathrm{Tr}(M_1)$ for $(1)^{\pm(k)}$ orbits with $k = 0,1,2$ is shown in Fig. 8. Since increasing k corresponds to larger β, the critical angle becomes smaller as k increases. The intervals of restabilization of the $(1)^{+(k)}$ orbits are shown in Fig. 9, terminating at the critical angles $\theta_k^\dagger$.

Quantitative results for the β values at which the PDB's occur and for the critical angle are easily obtained from Eq. (43) for the monodromy matrix. Equation (43) can be written as

$$\mathrm{Tr}(M_1) + 2 = 4R(\theta, \omega_c T) = 4\cos^4(\theta) R_1(\theta, \omega_c T) R_2(\theta, \omega_c T), \tag{44}$$

where the zeros of the function $R(\theta, \omega_c T)$ give the parameter values for all PDB's. It is easily seen from Eq. (43) that factor R_1 has exactly one root in each interval k, whereas the factor R_2 has either two or zero roots in each interval, cor-

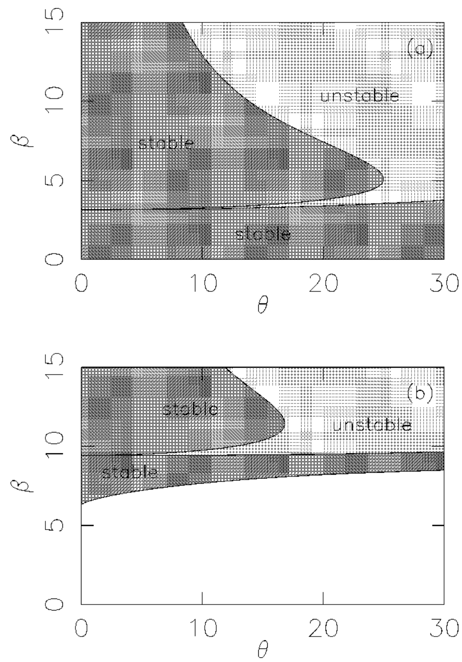

FIG. 9. Regions of existence (shaded areas) of one-bounce orbits $(1)^{+(0)}$ (a) and $(1)^{+(1)}$ (b) in the (θ,β) plane. Dark and light shading correspond to stable and unstable regions, respectively.

responding to the presence or absence of the restabilization. The set of transcendental equations which determine the roots of R_1, R_2 and hence the bifurcations points and critical angles are summarized in Appendix B.

The existence and stability properties of the one-bounce orbits as predicted by Eqs. (39),(43) are confirmed by the numerically generated SOS and indeed reveal the underlying pattern to the complex behavior seen in the SOS. The period-doubling bifurcations of the one-bounce orbits are of particular interest because they are closely related to the peak-doubling phenomena observed experimentally. We will elucidate this behavior in the next section on period-two orbits.

D. Two-bounce orbits

1. Qualitative description, $\beta\theta \ll 1$

For $\theta=0$ all two-bounce periodic orbits occur in helical families satisfying the resonance condition:

$$(2k+1)\omega_L = 2\omega_c, \quad k=0,1,2,\dots . \tag{45}$$

Only odd integers appear in the resonance condition since even integers yield orbits equivalent to the period-one helical family. As follows from Eqs. (32) and (45), the periods of the two-bounce helical orbits are given by

$$T=(2k+1)\frac{2\pi}{\omega_c}. \tag{46}$$

Therefore, just as for the one-bounce helical orbits, the resonant tori corresponding to the two-bounce orbits can only appear above a threshold value of β at which the longitudinal period becomes long enough to satisfy Eq. (46). At this threshold the two-bounce orbits are indistinguishable from the second repetition of the traversing orbit. Thus the thresholds $\beta_{c2}^{(k)}$ are given by the condition $2T_{\mathrm{TO}}=(2k+1)T_c$, which gives

$$\beta_{c2}^{(k)} = \pi(2k+1). \tag{47}$$

Once emerged, the period-two resonant tori remain in the phase space of the system for arbitrary large value of β, simply moving towards the periphery of the surface of section as β increases.

Again, as for the helical one-bounce periodic orbits, when the magnetic field is tilted, the resonant tori of the two-bounce orbits are destroyed and replaced by an integer number of pairs of stable and unstable two-bounce periodic orbits. By continuity, these orbits must appear in the vicinity of the $(1)^{+(k)}$ traversing orbits (which are now playing the role of the TO) and near the values $\beta \approx \pi(2k+1)$ at which the two-bounce tori appear. Our previous analysis for small tilt angles has already identified one direct and one inverse period-doubling bifurcation of the $(1)^{+(k)}$ near these values of β (see Fig. 8). In a direct PDB a stable one-bounce PO becomes unstable while generating a stable two-bounce PO in its neighborhood; in an inverse PDB an unstable one-bounce PO becomes stable while creating an unstable two-bounce PO in its neighborhood. Hence for consistency we conclude that exactly one pair of two-bounce PO's is created from each two-bounce family for infinitesimal tilt angle. Furthermore, one of these arises from the direct PDB and is therefore stable, whereas the other arises from the inverse PDB and is unstable. (For infinitesimal tilt angle the interval $\Delta\beta$ between these two PDB's is also infinitesimal and they are created at the same ''time'' in agreement with the Poincaré-Birkhoff theorem; for any finite angle they are separated by some finite interval in β.)

It follows that there must be exactly two orbits from each helical family that are continuously deformed into the stable and unstable two-bounce PO's created at these two PDB's. It is easy to identify one of the two in analogy to our earlier reasoning. There is only one two-bounce PO in each helical family for which both of its two collisions with the barrier occur with $v_y=0$ (see Fig. 10). This orbit can be continuously deformed into a nonmixing two-bounce orbit that will become degenerate with the nonmixing $(1)^{+(k)}$ at the PDB—see Fig. 11(a). However, unlike the case for one-bounce HO's, there is no second orbit with fixed points at $v_y=0$, that can evolve into the second two-bounce orbit which we know must be created. Hence this second orbit at $\theta\neq 0$ must be mixing; i.e., it must generate fixed points with nonzero v_y. Thus it must be obtained by a deformation of one of the two-bounce orbits in the helical torus with finite values of v_y at collision.

To identify which orbit this is we must consider the general properties of mixing two-bounce orbits in this system. We have noted above that due to time-reversal symmetry the SOS has to be symmetric under the transformation $v_y \to -v_y$. It is obvious that a two-bounce orbit with the same value of v_x at each collision will generate two fixed points in the SOS that satisfy this reflection symmetry. Note that since $v_x \propto y$, such a mixing period-two orbit strikes the barrier at the same value of y in each collision. We will refer to such orbits as self-retracing since they retrace themselves in y-z

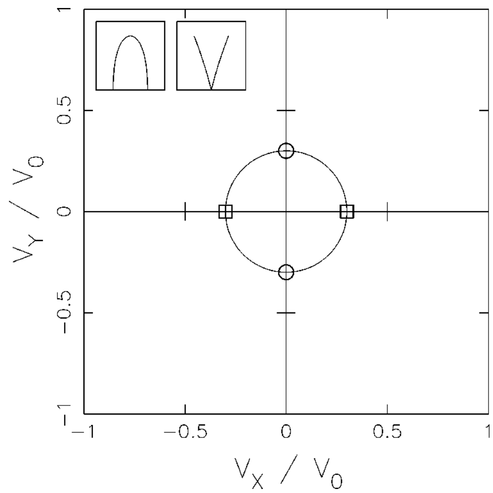

FIG. 10. Torus of two-bounce orbits in the surface of section. Marked are the only ''self-retracing'' (in the y-z plane) two-bounce orbits: (a) the orbit with $v_y=0$ at collisions, which evolves into the nonmixing two-bounce orbit $(2)^+$, and (b) the orbit with $v_x=0$ at collisions—which becomes the self-retracing mixing orbit $(2)^-$. Insets show the y-z projections of these orbits.

projection. All such self-retracing two-bounce orbits are mixing. However, there exist non-self-retracing two-bounce mixing orbits. These must collide with different values of v_x at each collision, but still satisfy the required reflection symmetry of the SOS in a more subtle manner. In such an orbit the values of v_x at collision differ *for any one sense of traversal*, but traversing the orbit in the opposite sense generates two additional fixed points that restore the $v_y \to -v_y$ symmetry of the SOS, which has four fixed points for such orbits. Such an orbit is shown in Fig. 11(c), and analogous orbits exist for higher-bounce PO's as well. We will discuss their origin later.

However, these non-self-retracing two-bounce orbits cannot be created at a PDB of a one-bounce orbit (period-one fixed point) since such a PDB cannot create more than two new fixed points.[32,33] Therefore the second, mixing orbit we seek for $\theta \neq 0$ must be a self-retracing orbit, i.e., it must have the same value of v_x at each of its two collisions with non-

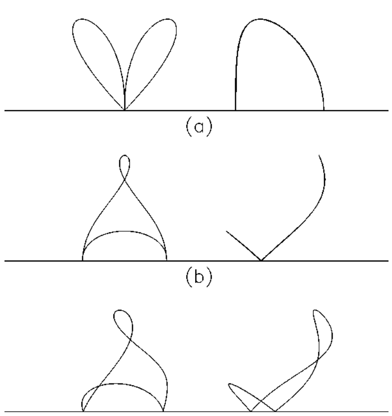

FIG. 11. Examples of the different types of period-two orbits, projected onto (x,z) and (y,z) planes: a nonmixing orbit (a), a self-retracing mixing orbit (b), and a non-self-retracing mixing orbit (c).

TABLE I. Period-1 and period-2 orbits in the SBM.

orbit	y−z projection	origin	initial stability
$(1)^+$	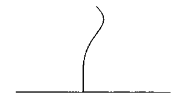	TB with $(1)^-$	stable
$(1)^-$	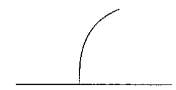	TB with $(1)^+$	unstable
$(2)^+$	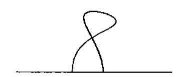	PDB of $(1)^+$	stable
$(2)^-$	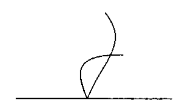	IPDB of $(1)^+$	unstable
$(2)^*$	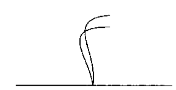	PDB of $(1)^+$	stable

zero v_y—see Fig. 11(b). The only orbit in the $\theta=0$ helical family with this property is the one which collides with the barrier with $v_x=0$ at each collision (see Fig. 10). Hence by continuity it is this orbit which must be continuously deformed to give the mixing orbit which must, by the Poincaré-Birkhoff theorem, exist for infinitesimal tilt angle. Intuitively, the PDB of the $(1)^{+(k)}$ orbit to the nonmixing two-bounce orbit corresponds to splitting the $(1)^{+(k)}$ at the point of collision, whereas the PDB corresponding to the mixing one corresponds to splitting the $(1)^{+(k)}$ at the point furthest away from the collision (see Table I).

Since lack of mixing at collision should enhance the stability of an orbit for given β,θ, we may expect that the non-mixing two-bounce orbit is born stable in the direct PDB and the mixing one is born unstable at the inverse PDB that occurs at a slightly higher value of β. This conjecture is confirmed by our analytic calculations below. In accord with our earlier notation we will label this pair of two-bounce orbits, which must exist in each interval by continuity, as

$$(2)^{\pm k}, \tag{48}$$

where the sign ''+'' corresponds to the orbit that is initially stable, as before. For simplicity we drop the interval index k below. The same scenario occurs in each interval, just at smaller θ as k is increased.

2. Qualitative description, $\beta\theta \sim 1$

Up to now we have focused on the limit of small $\beta\theta$ where each orbit must by continuity have an analog for $\theta=0$. Unlike single-bounce orbits in the tilted well, there will exist orbits with two or more bounces that have no analogs in the integrable case. In fact, we have already shown above (see Figs. 8,9) that after restabilizing by inverse PDB the $(1)^+$ orbit must eventually go unstable by a third PDB that must give rise to a stable two-bounce orbit with no analog in the untilted system. We denote these new orbits as $(2)^*$; one such orbit must exist for each $(1)^+$ orbit although for small tilt angle they will not appear until values of $\beta \sim 1/\theta$.

Will the $(2)^*$ orbits be mixing or nonmixing? One can also decide this by reference to our stability analysis of the $(1)^+$ orbit (see Fig. 8 above). As we showed, for each $(1)^+$ orbit, as θ is increased to a critical value $\theta^\dagger$, the second and third PDB's move closer together and finally merge, after which no restabilization of the $(1)^+$ orbit occurs. But the second PDB is associated with the mixing $(2)^-$ orbit; if it merges with the $(2)^*$ orbit when the second and third PDB coincide, then $(2)^*$ orbits must also be of the same topology, i.e., mixing.

What happens to the $(2)^-$,$(2)^*$ orbits for tilt angles above $\theta_k^\dagger$? On the one hand, above $\theta_k^\dagger$ they cannot be created by PDB's of the $(1)^+$ orbit, since we have shown that it never restabilizes. On the other hand, these two periodic orbits cannot cease to exist suddenly, since they exist for an infinite interval above the threshold for PDB and the orbit far from threshold is negligibly perturbed by a small increase in tilt angle. The resolution of this apparent paradox is that above $\theta_k^\dagger$ the two orbits are created by a tangent bifurcation in a region of the SOS and at a value of β very close to that at which the PDB's occur below $\theta_k^\dagger$. The detailed description of the transition from the PDB scenario to the TB scenario is sketched in Fig. 12 and described in the caption. In contrast, nothing qualitatively new happens to the behavior of the initially stable $(2)^+$ as θ is increased beyond $\theta_k^\dagger$; its interval of stability just shrinks continuously.

So for *all* θ we are able to locate all two-bounce orbits that are related originally to the one-bounce $(1)^{+(k)}$ orbit, and to describe their evolution qualitatively. There are exactly three such orbits associated with each $(1)^+$ orbit: the $(2)^+$, which is initially stable and nonmixing, the $(2)^-$, which is initially unstable and mixing, and the $(2)^*$, which is initially stable and mixing.

The last point to understand is the evolution of these orbits with increasing β once they are created. Since these orbits exist for all β above threshold at $\theta = 0$, we expect the same behavior for nonzero θ. However, as both the $(2)^+$ and $(2)^*$ orbits are initially stable, we expect them both to become unstable as $\beta \rightarrow \infty$. It turns out that the $(2)^+$ orbit goes unstable as the second stage of an infinite period-doubling transition to chaos. The $(2)^*$, on the other hand, follows a more complex route to its final unstable form. As the parameter β is increased, the orbit $(2)^*$ goes unstable via a period-doubling bifurcation, but soon restabilizes and finally goes unstable via a *pitchfork* bifurcation. In such bifurcation a new stable (mixing) orbit is created with a period identical to that of the orbit that has gone unstable. In this case the new orbit is precisely of the non-self-retracing type shown in Fig. 11(c) and described above. Thus this one new two-bounce orbit creates four fixed points in the SOS and satisfies the required conservation of the Poincaré index. From the generic properties of 2D conservative maps it can be shown that such orbits can *only* be created in these pitchfork bifurcations. Although it is interesting to note the origin of the non-self-retracing two-bounce orbits, they are of a little importance for the description of the experimental tunneling spectra, since generally the pitchfork bifurcations appear at relatively high values of β, as we will show in the quantitative description of the two-bounce orbits in the next subsection.

In principle, completely new two-bounce orbits can also arise by tangent bifurcations at sufficiently large tilt angles and values of β, in fact no visible islands due to such orbits

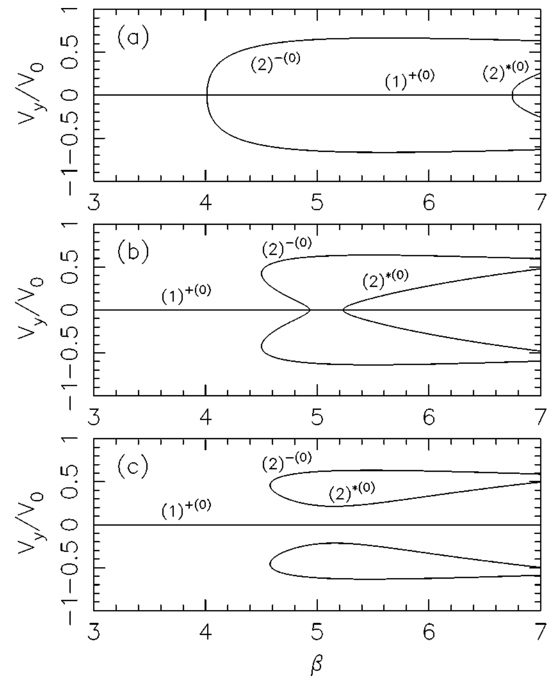

FIG. 12. Bifurcation diagrams in the coordinates $(\beta,\tilde{v}_y)$ for the period-two mixing orbits, related to the bifurcations of the single-bounce orbits. The two branches with nonzero $\tilde{v}_y$ correspond to the two-bounce mixing orbits $(2)^{+(0)}$ and $(2)^{*(0)}$, while the horizontal line represents the single-bounce orbit $(1)^{+(0)}$. The nonmixing period-two orbit $(2)^{-(0)}$ has $v_y = 0$ at each of the points of collision and cannot be seen in this diagram. For a small tilt angle the period-two orbits are born in period-doubling bifurcations—see panel (a). When $\theta > \theta_k^\dagger$ the mixing period-two orbits are born in a tangent bifurcation—see panel (c). The transformation from the two types of behavior cannot happen in a single step. If it were possible, then at the critical angle *two* new mixing two-bounce orbits were created at the location of the single-bounce orbit, which *cannot* happen in a generic conservative 2D system. The alternative is provided by the following two-step process. First, at some critical angle $\theta_k^0 < \theta_k^\dagger$ the behavior of the first to appear mixing orbit $(2)^{-(k)}$ is changed, as is shown in the bifurcation diagram at the panel (b). When $\theta_k^0 < \theta < \theta_k^\dagger$, the unstable orbit $(2)^{+(k)}$ appears in a tangent bifurcation with a new self-retracing mixing stable period-two orbit, which is soon to be absorbed by the single-bounce orbit in an backwards period-doubling bifurcation, while the qualitative behavior of the stable $(2)^{*(k)}$ orbit remains unchanged. As the tilt angle is increased, the interval of stability of the single-bounce orbit shrinks, while the interval of existence of the auxiliary mixing orbit increases. At the critical tilt angle the backwards and standard period-doubling bifurcations merge and annihilate each other, so that at greater values of the tilt angle the mixing period-two orbit are no longer directly related to the single-bounce orbit—see panel (c).

are seen in the SOS for any tilt angles of interest in the range of β values that are accessible experimentally. Thus for understanding the experimentally observed peak-doubling regions only the the three two-bounce orbits $(2)^+,(2)^-,(2)^*$ for the intervals $k=0,1$ are most relevant. Their properties are summarized in Table I. These orbits, once their generalization to the double-barrier model is understood, will be sufficient to explain the peak-doubling data of Refs. 10 and 12.

We now give an analytical description of the periods and stability of the two-bounce orbits identified above.

3. Quantitative theory: Nonmixing two-bounce orbits

The derivation of the periods of the nonmixing two-bounce orbits can be performed using the same technique developed in the analysis of the single-bounce orbits. In the drift frame introduced in Sec. III C 2 the orbit consists of two identical and overlapping arcs of a circle of angular size $\omega_c T > \pi$ with their endpoints displaced by $v_d T/2$. Imposing the nonmixing condition at the two collisions determines T. Conservation of energy is not required to fix the period and this leads to the striking result that the period is independent of energy (this is the only relevant orbit with this property). This calculation, the details of which are given in the Appendix D, yields

$$\frac{\omega_c T}{4}\cot\frac{\omega_c T}{4} = -\tan^2\theta. \tag{49}$$

The $(k+1)$-th positive root of this equation gives the value of the period of the $(2)^{+(k)}$ orbit. Note that the solutions T do not depend on β. This is the only orbit with this property.

We have also calculated the stability properties of these orbits by evaluating the trace of the corresponding monodromy matrix using the general expressions developed in Appendix C. This straightforward but tedious derivation is given in Appendix E. In Fig. 13 we plot $\mathrm{Tr}(M)$. In agreement with our qualitative analysis, $\mathrm{Tr}(M)$ is a monotonically decreasing function of β, so that the initially stable two-bounce nonmixing orbit destabilizes by a period-doubling bifurcation and then remains unstable for all β. The four-bounce periodic orbit, which is born in this bifurcation, will

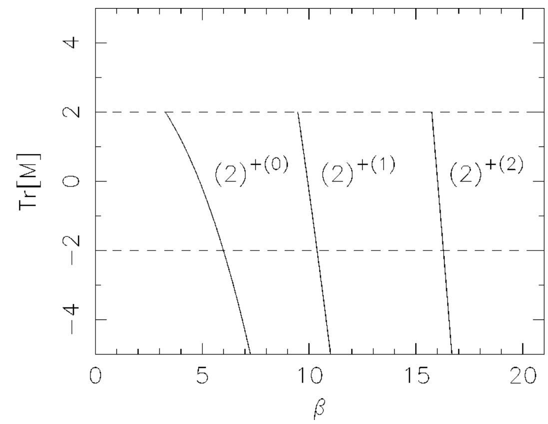

FIG. 13. Trace of the monodromy matrix as a function of β for different nonmixing two-bounce periodic orbits: $(2)^{+(0)}$, $(2)^{+(1)},(2)^{+(2)}$ for $\theta=15°$.

in turn bifurcate, producing an infinite series of period-doubling bifurcations of the same type as the period-doubling sequence in the quadratic DeVogelaere map.[34,26] However, since the periodic orbits of this sequence have long periods and relatively large cyclotron energy, they are of a little importance for the description of the tunneling spectra in the tilted well, and will not be discussed in the present paper.

4. Quantitative theory: Mixing period-two orbits

Due to nonzero energy exchange at the points of collision the analytical description of a general mixing two-bounce periodic orbit will be very complicated. However, as we pointed out before, the most important two-bounce mixing orbits are self-retracing (in y-z projection) leading to the symmetry property that v_x is the same a both collisions. Imposing this condition simplifies the analytical treatment. For each of these orbits, the electron collides with the barrier twice at the same point with exactly the same *absolute values* of the velocity components v_x, v_y, v_z. Using this property, one can show (see Appendix F), that the periods T of the two-bounce self-retracing orbits must satisfy the following system of coupled transcendental equations:

$$\frac{\sin\left(\frac{\omega_c T}{2}\right)}{\frac{\omega_c T}{2}} = -\tan^2\theta \frac{\sin\left(\frac{\omega_c \delta T}{2}\right)}{\frac{\omega_c \delta T}{2}}, \tag{50a}$$

$$\left(\frac{\beta}{2}\right)^2 = \sin^2\theta\left(1 - \frac{\frac{\omega_c T}{2}\left[\cos\left(\frac{\omega_c T}{2}\right)+\cos\left(\frac{\omega_c \delta T}{2}\right)\right]}{2\sin\left(\frac{\omega_c T}{2}\right)}\right)^2 + \left(\frac{\omega_c T}{4}\right)^2 + \cot^2\theta\left(\frac{\omega_c \delta T}{4}\right)^2, \tag{50b}$$

where $\delta T < T$ is the difference of the time intervals between successive collisions t_1 and t_2 (see Appendix F). This system of two equations determines the periods of all of the self-retracing two-bounce orbits as functions of β and the tilt angle.

Although Eqs. (50a),(50b) look quite complicated, they allow a further analysis. Assume at least one solution exists for some fixed value of T and find the corresponding value(s) of the time difference δT from Eq. (50a) that depend explicitly only on T,θ (but only implicitly on β). As an equation for δT at fixed T and θ, this relation can have multiple solutions $\delta T = \delta T_n$:

$$\omega_c \delta T_n = 2\wp_n\left(-\cot^2\theta \frac{\sin\left(\frac{\omega_c T}{2}\right)}{\frac{\omega_c T}{2}}\right), \quad \delta T_n < T \tag{51}$$

where the function $\wp_n(x)$ was defined in Appendix B [see Eq. (B5)] and the maximal value of n depends on the values of T and θ. If T is not a solution of the system for any β, Eq. (8) will have no roots with $\delta T < T$. One knows (from the calculation of the stability matrix for the single-bounce orbits) the exact values of T at which the $(2)^{-(k)}$,$(2)^{*(k)}$ orbits are born by PDB and inverse PDB of the $(1)^{+(k)}$. Hence we can find the starting value of T for each $(2)^{-(k)}$,$(2)^{*(k)}$ orbit and follow it continuously as β increases. Each root δT_n when inserted into Eq. (50b) yields a solution ''branch'' $\beta_n(T)$ for a two-bounce orbit.

There does not however need to be exactly one self-retracing two-bounce orbit for each solution branch $\beta_n(T)$. If the period of such an orbit is a nonmonotonic function of β then the same orbit will give rise to multiple solution branches that must merge at the extrema of $T(\beta)$. One can show that there can be no more than one extremum at finite β for $T(\beta)$, thus each orbit will be described by either one or two such branches. Conversely, one solution $\beta_n(T)$ can be nonmonotonic in T, hence it must describe two different two-bounce orbits with different periods at the same value of β. With care, *any* two-bounce self-retracing orbit can be obtained by this approach. This procedure yields the plots of the periods for the $(2)^{-(0)}$,$(2)^{*(0)}$ orbits shown in Fig. 14. Note that unlike the nonmixing $(2)^{+(k)}$ orbits, the periods of the mixing orbits depend on β.

In fact for small tilt angles the period of the $(2)^{-(k)}$ orbit is a monotonically decreasing function of β and there is only the $n=1$ solution branch to consider. In this case we can expand Eqs. (7),(8) for $\beta\theta \ll 1$ and obtain an explicit formula for the periods of these orbits:

$$\omega_c T = 2\pi(1+2k)\{1+\theta^2+\tfrac{1}{6}\theta^4[8+\pi^2(1+2k)^2-\beta^2]\} + O(\theta^6). \tag{52}$$

Although the $(2)^*$ orbits have the same topology as the $(2)^-$ (and at large θ they are born together in a tangent bifurcation), they have no analogs in the untilted system so their periods cannot be obtained from such an expansion. The quantitative analysis of Eqs. (50a),(50b) confirms the transition scenario between PDB and TB for the $(2)^-$,$(2)^*$ for large tilt angles described in Fig. 12.

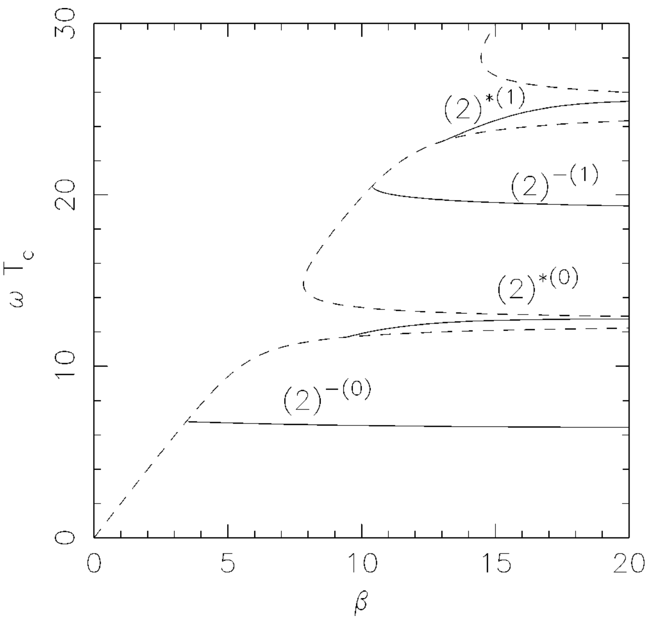

FIG. 14. Periods of the self-retracing mixing two-bounce orbits $(2)^{-(0)}$, $(2)^{*(0)}$, $(2)^{-(1)}$, and $(2)^{*(1)}$, related to the bifurcations of the single-bounce periodic orbits as functions of β. The tilt angle is $\theta=15°$. The dashed lines show the (scaled) time intervals of two repetitions of single-bounce orbits (i.e., twice the period of single-bounce orbits).

Once the values of T and δT are known from the Eqs. (50a),(50b), the components of the velocity at the points of collisions can be obtained from Eq. (F4), and one can calculate the monodromy matrix for each such orbit using Eqs. (C4) and (C3). In Fig. 15 we show the behavior of the trace of the monodromy matrix for $(2)^-$ and $(2)^*$ orbits. As argued above, one finds that the $(2)^-$ orbits are unstable for all β, whereas the $(2)^*$ orbits which are born stable [since they arise from a direct PDB of the $(1)^+$ orbit], and go unstable in the complicated sequence ending with a pitchfork bifurcation that we have described above—see Fig. 15.

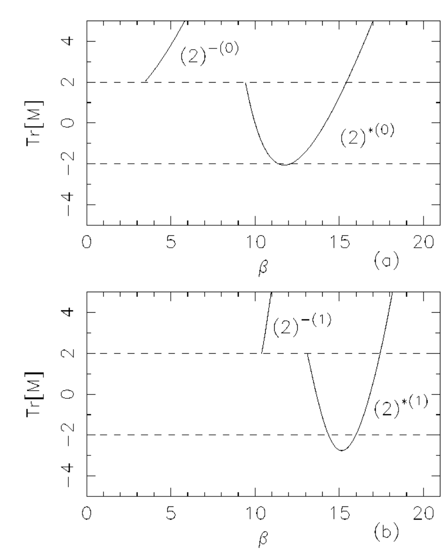

FIG. 15. Trace of the monodromy matrix as a function of β for mixing two-bounce orbits (a) $(2)^{-(0)}$ and $(2)^{*(0)}$, $(2)^{-(1)}$, and $(2)^{*(1)}$. The tilt angle is $\theta=15°$.

In Table I we summarize the relevant period-one and period-two orbits.

E. Three-bounce periodic orbits

The scenario for the three-bounce periodic orbits is similar in many ways to that for the two-bounce orbits just described. When the magnetic field is not tilted all three-bounce periodic orbits belong to resonant tori and correspond to the resonances

$$k\omega_L = 3\omega_c, \tag{53}$$

where the integer k is not a multiple of 3. Thus as β increases from zero in the first interval there are two thresholds for the birth of resonant tori. When $\beta = 2\pi/3$ the family of helical orbits that perform 1/3 of a cyclotron rotation per collision with the barrier appears, and at $\beta = 4\pi/3$ the family that makes 2/3 of a rotation per collision appears. As for the two-bounce orbits, the analogous orbits in the higher intervals behave in exactly the same manner qualitatively, and so we focus here on those in the first interval.

When the magnetic field is tilted, the period-three resonant tori are destroyed and replaced by pairs of stable and unstable three-bounce orbits. Here some important differences from the two-bounce orbits enter. First, we cannot have a *single* three-bounce orbit created at some value of β since there is no analog of a period-doubling bifurcation for creating three-bounce orbits. At the threshold for creation of the three-bounce helical families, when they are degenerate with the third repetition of the traversing orbit, the $\mathrm{Tr}(M_1) = -1$ and its stability cannot change. Therefore period-three orbits must always be created in stable-unstable pairs by tangent bifurcation. Moreover, there is generically no constraint that such a tangent bifurcation occur at the fixed point corresponding to a period-one orbit.[32] In this sense there are no trifurcations in a generic system. When $\theta = 0$ the rotational symmetry of the system does constrain the entire family of three-bounce orbits to appear degenerate with the third repetition of the traversing orbit, but as soon as $\theta \neq 0$ the pair of three-bounce orbits that survive are created away from the period-one fixed point. However, by continuity the tangent bifurcation (TB) that creates this pair must occur near this fixed point and at approximately the same value of β. We infer that for small tilt angles there are at least two TB's in the first interval, each of that creates a stable-unstable pair of three-bounce orbits, at $\beta_1 \approx 2\pi/3, \beta_2 \approx 4\pi/3$. Extending our earlier notation, we will denote these four orbits by $(3)_1^{\pm}, (3)_2^{\pm}$.

Which orbits of the resonant tori survive? In this case there is no orbit in the helical family that has all of its collisions with $v_y = 0$; therefore by continuity there can be no three-bounce nonmixing orbits for small tilt angles (and one can easily show that this result holds for any θ). However, there are two orbits in each torus that collide with $(v_y)_1 = 0, (v_y)_2 = -(v_y)_3$ corresponding to two possible orientations of the appropriate equilateral triangle along the v_x axis. These two orbits satisfy the required symmetry of the SOS upon tilting, while no others in the torus do. Therefore it is these orbits which survive (slightly distorted due to the tilt, of course).

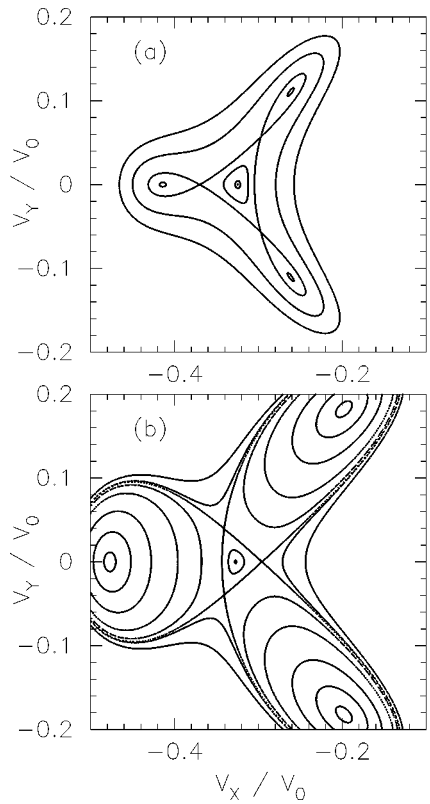

FIG. 16. Surface of section near the one-bounce periodic orbit $(1)^{+(0)}$ close to its 1:3 resonance and the corresponding touch-and-go bifurcation of the orbits $(3)_2^-$: (a) just before and (b) soon after the touch-and-go bifurcation.

This conclusion, while correct, must be reconciled with our earlier statement that the two orbits must appear at a tangent bifurcation. At a TB the two orbits are identical, yet the two orbits we have identified correspond to opposite orientations of the triangle and would not coincide for any finite size of the triangle defining the three fixed points (see Fig. 16). In order to coincide at the TB the unstable member of the pair must actually pass through the single-bounce fixed point at the center of the triangle in what is known as a ''touch-and-go'' bifurcation.[32] At this point the unstable three-bounce orbit coincides with the third repetition of the $(1)^+$ orbit, which is no longer isolated and $\mathrm{Tr}(M_1^3) = 2$ [or equivalently $\mathrm{Tr}(M_1) = -1$]. So as β is reduced to the threshold for the TB, first the unstable three-bounce orbit shrinks to a point coinciding with the period-one fixed point, and then at even lower β reappears on the other side with the appropriate symmetry to disappear by TB with the stable member of the pair. In Fig. 16 we show the surfaces of section just before (a) and soon after (b) the touch-and-go bifurcation of the orbits $(3)_1^-$ and $(1)^{+(0)}$. This ''touch-and-go'' (TAG) bifurcation of the three-bounce orbits occurs over such a small β interval for small tilt angles that it is hard to distinguish from a trifurcation of the $(1)^+$ orbit without careful magnification of the transition, but it is required by continuity and the generic principles of 2D conservative maps. In Fig. 17 we plot the periods of these four three-bounce orbits, $(3)_1^{\pm}, (3)_2^{\pm}$, that are related to the resonant tori of the untilted system.

As in the case of the two-bounce orbits, our knowledge of

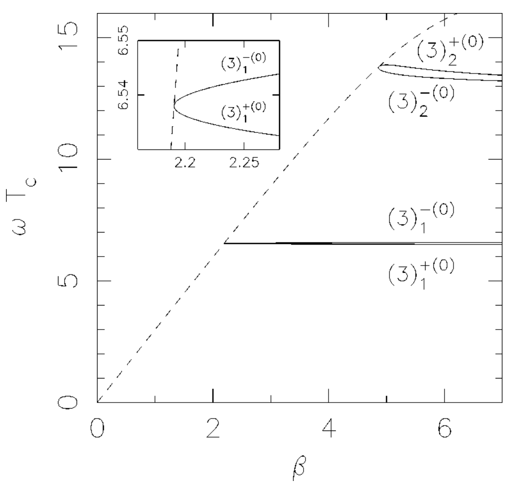

FIG. 17. The periods of the three-bounce orbits $(3)_1^{\pm 0}$ and $(3)_2^{\pm 0}$ vs β for tilt angle for $\theta = 15°$ (solid lines). The dashed line represents the period of single-bounce orbit $(1)^{+(0)}$, multiplied by 3.

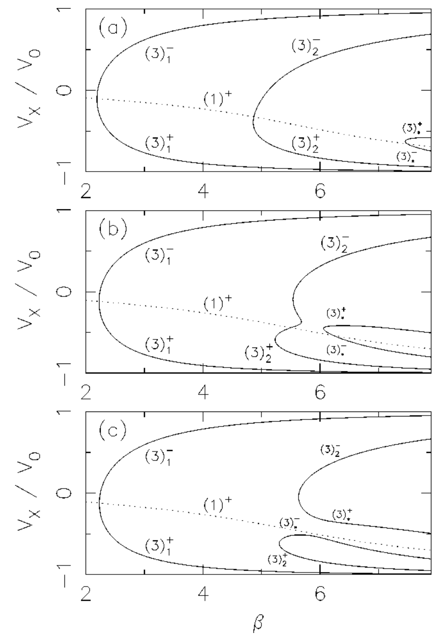

FIG. 18. The bifurcation diagrams of the self-retracing three-bounce orbits in three different regimes (see text), $\theta = 15°$. The vertical axis represents the x component of the scaled velocity of the electron at the point of collision with $\tilde{v}_y = 0$. The dotted line represents the single-bounce orbit. Note the exchange of partners bifurcation between (b) and (c).

the behavior of the $(1)^+$ orbit allows us to predict that in the first interval their must exist a further (pair) of three-bounce orbits that have no analog in the untilted system. The reason is the following. From Fig. 8, for small tilt angle, we know that the $\mathrm{Tr}(M_1)$ for the $(1)^+$ orbit passes through -1 three times before the $(1)^+$ orbit becomes permanently unstable. Each time $\mathrm{Tr}(M_1) = -1$ there must be a TAG bifurcation, so there must be three such bifurcations. Two of them are associated with the $(3)_1^-, (3)_2^-$ orbits we have already identified and occur near $\beta = 2\pi/3, 4\pi/3$; the third TAG bifurcation must be associated with a third pair of orbits born by TB at large $\beta \sim 1/\theta$. This pair plays a similar role for the three-bounce orbits as does the $(2)^*$ orbit for the two-bounce orbits in each interval, hence we denote them by $(3)_*$.

As θ is increased to order unity, the TAG bifurcation of the $(3)_*^-$ orbit moves to lower β till it eventually coincides with the TAG bifurcation of the $(3)_2^-$ orbit and the two bifurcations ''annihilate.'' We know this must occur since $\mathrm{Tr}(M_1)$ ceases passing through -1 the second and third times (see Fig. 8). The TAG resonances relating the orbits to the resonances of the $(1)^+$ orbit no longer exist for higher θ (just as the PDB's of the $2^-, 2^*$ no longer exist above some critical angle), but the orbits do not disappear. Instead, they demonstrate an ''exchange of partners'' bifurcation, which for higher tilt angles allows them to exist without ever evolving into TAG resonances of the $(1)^+$—see Fig. 18. Again, just like for the two-bounce orbits, the transformation from the small tilt angle to large tilt angle behavior requires the appearance of auxiliary three-bounce orbits in additional tangent bifurcations to provide a smooth evolution. This scenario is illustrated by the bifurcation diagrams in Fig. 18.

In principle, an analytic theory of the periods and stability of these three-bounce orbits is possible, but the system of three coupled transcendental equations which define the period is not easily analyzed. Since we already know the qualitative scenario, we have simply used the symmetry properties of these three-bounce orbits to locate numerically the fixed points and hence find the period and time interval between collisions. These quantities are all we need to use the general formalism for the monodromy matrix developed in Appendix C.

In Fig. 19 we show the behavior of the trace of the monodromy matrix for three-bounce orbits $(3)_1^{\pm(0)}$, $(3)_2^{\pm(0)}$, and $(3)_*^{\pm(0)}$. The stability properties of the three-bounce orbits show a clear analogy with the behavior of two-bounce orbits. The $(3)_1^{\pm}, (3)_2^{\pm}$ orbits related to the resonant tori, are either always unstable, or go unstable via period-doubling bifurcations and never regain stability. Whereas the behavior of the new $(3)_*$ is different. As follows from Fig. 19, the initially unstable $(3)_*$ restabilizes via a pitchfork bifurcation after its TAG bifurcation with the $(1)^+$ orbit, before eventually going unstable in a period-doubling bifurcation at higher value of β. The initially stable $(3)_*$ orbit has a monotonically decreasing trace of the monodromy matrix and goes unstable via a period-doubling bifurcation. All of these orbits are self-retracing in the sense defined above. At the pitchfork bifur-

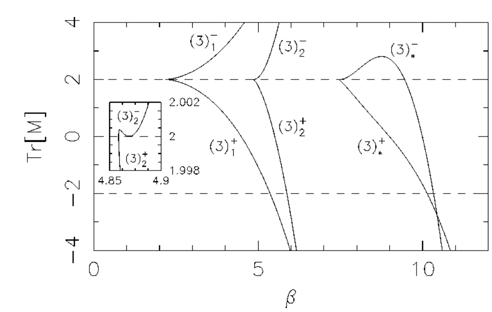

FIG. 19. Trace of the monodromy matrix as a function of β for self-retracing three-bounce orbits. The inset shows the behavior of $\mathrm{Tr}[M]$ near the touch-and-go bifurcation.

cation of the $(3)_*$ orbit just described, a new three-bounce orbit appears that is non-self-retracing. Thus, as for the two-bounce orbits, orbits of this type only appear after the creation of the self-retracing orbits and hence arise at relatively high β values. Hence they have little effect on the experimental observations and will be disregarded below.

F. Many-bounce orbits

The analysis of period-N ($N>3$) orbits can be conducted in a similar framework. First, one can identify the periodic orbits, which survived from the resonant tori of the untilted system, and then relate these orbits to the $1:n$ resonances of the single-bounce orbits $(1)^+$. Since for small tilt angles $\mathrm{Tr}(M_1)$ is nonmonotonic with β and crosses the stability region three times, the third crossing will always give rise to new orbits that are born at $\beta\sim 1/\theta$ and that have no analogs in the untilted system. As θ is increased these resonances will move to lower β and annihilate with earlier resonances leading to new tangent bifurcations and the ''exchange of partners'' already understood and observed for the two-bounce and three-bounce orbits.. Additional new orbits can be formed both by pitchfork bifurcations of self-retracing orbits and by completely new tangent bifurcations, however such orbits appear to play no role in the first and second interval for experimentally relevant values of β. More generally, there is no experimental evidence that periodic orbits with $N>5$ play a role, presumably because either their periods are too long and they are damped out by phonon effects, or they have too much cyclotron energy to reach the emitter in the experimental parameter range. As they introduce no essentially new physics we will not present a detailed treatment of these orbits.

IV. PERIODIC ORBITS IN THE DBM

We now analyze the periodic orbit structure of the double-barrier model (DBM). This model will provide a description of periodic orbits relevant to the experiments of Refs. 10 and 12. A crucial point discussed in Sec. II A and II B above is that in general for a fixed tilt angle the classical dynamics of the DBM depends on two dimensionless parameters: the parameter $\beta=2v_0B/E$ already used in analyzing the SBM, and the parameter $\gamma=\epsilon_0/eV$ measuring the ratio of the injection energy to the voltage drop. Fortunately, in the experiments this second parameter is roughly constant,[12,15] $\gamma\approx 1.15-1.17$. Therefore the theory of the periodic orbits (and ultimately the semiclassical tunneling theory) need only be done varying β with γ fixed to the experimental value. We will focus on this case henceforth. In interpreting the results of this section however, it must be borne in mind that β no longer is the product of three independent variables; v_0 and E are related by the condition of constant γ. The magnetic field, however, is still an independent variable and thus it is easiest to think of increasing β as increasing the magnetic field.

Many of the periodic orbits we will discuss below have been previously identified by Fromhold and co-workers[10] or Monteiro and Dando.[14] What has not been done is to systematize all the experimentally relevant orbits and find their intervals of existence and stability. This we attempt to do below.

As previously noted, the theory of periodic orbits in the DBM is in many respects similar to that of the SBM, but there are three significant differences. First, orbits can be born or disappear in a manner that violates the generic bifurcation principles for conservative systems since the Poincaré map for the DBM is nonanalytic on the critical boundary of the SOS (the curve separating initial conditions that will reach the emitter barrier from those that will not, cf. Sec. II E). The bifurcations that result (which we call cusp bifurcations) play a crucial role in the behavior of the short periodic orbits in the system. Second, the unperturbed system has a more complicated structure as there can exist two distinct resonant tori corresponding to the same resonance condition $n\omega_c=k\omega_L$, one corresponding to helical orbits that do reach the emitter, and the other corresponding to helical orbits that do not. Third, once the field is tilted, orbits which are periodic after N bounces with the collector may collide with the emitter any number of times from zero to N. As a function of β such orbits can change their connectivity with the emitter. In fact, it can be shown that any orbit that does reach the emitter can only exist for a finite interval of β. We will now explain these important points in detail.

A. Periodic orbits at $\theta=0$

First let us assume there exists an $\{n,k\}$ resonant torus of the unperturbed system that does not make any collisions with the emitter barrier for a given value of β. At $\theta=0$ longitudinal and cyclotron energy decouple and, as the emitter barrier plays no role, the frequency of the longitudinal motion must be given by Eq. (30) for the SBM. Using this formula for ω_L, the resonance condition $n\omega_c=k\omega_L$ leads to a condition on β:

$$\beta=2\pi\frac{k}{n}\sqrt{\varepsilon_0/\varepsilon_L}. \tag{54}$$

Exactly as for the SBM, if such an orbit exists for one value of the longitudinal energy ε_L, another such family will exist at the same total energy but with smaller longitudinal energy, since adding to the cyclotron energy does not change ω_c. From Eq. (54) the new family with smaller ε_L will exist at higher β as the magnetic field will have to be increased to keep it in resonance. As β increases for such families the orbits will just move further away from the emitter but will always exist above the threshold value defined by the maximum value of ε_L. Unlike the SBM, however, the maximum allowed value is not ε_0, since before all the energy is put into longitudinal motion the orbit begins to hit the emitter barrier; this happens of course when $\varepsilon_L=eV\equiv\varepsilon_0/\gamma$. We will call orbits that do not reach the emitter ''collector'' orbits and those which do ''emitter'' orbits. Our argument implies that there exist families of $\{n,k\}$ helical collector orbits for all β *above* the threshold $\beta_c=2\pi(k/n)\sqrt{\gamma}$. These orbits are identical to those in the SBM and the only change introduced by the emitter barrier is that the threshold for their creation has been raised by a factor $\sqrt{\gamma}=\sqrt{\varepsilon_0/eV}$.

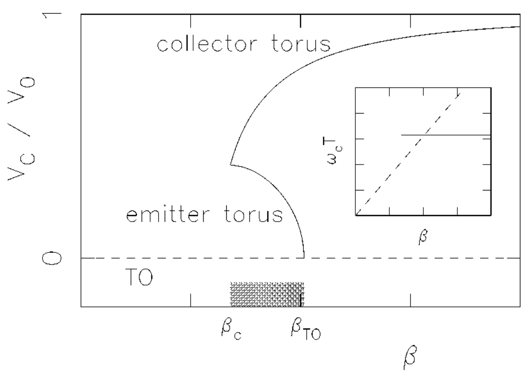

FIG. 20. The scaled cyclotron velocity for the resonant tori as function of β at zero tilt angle; $\gamma=1.2$, $n=1$, number of cyclotron rotations per period $k=1$. The horizontal line $\widetilde{v}_c=0$ corresponds to the traversing orbit. Inset shows the (scaled) period of the corresponding orbits.

Now assume there exists an $\{n,k\}$ family for a given value of β that *does* reach the emitter barrier. The longitudinal frequency of any such orbit is easily calculated to be

$$\omega_L=\frac{2\pi\omega_c}{\beta}\sqrt{\frac{\varepsilon_0}{\varepsilon_L}}\left(1-\sqrt{1-\frac{eV}{\varepsilon_L}}\right)^{-1}. \tag{55}$$

Note the crucial difference here from Eq. (30): for the emitter orbits ω_L is an *increasing* function of ε_L. Imposing the resonance condition then leads to the relation

$$\beta=2\pi\frac{k}{n}\sqrt{\frac{\varepsilon_0}{\varepsilon_L}}\left(1-\sqrt{1-\frac{\varepsilon_0}{\gamma\varepsilon_L}}\right)^{-1}, \tag{56}$$

which implies that β is also an increasing function of ε_L in the interval of interest. For emitter orbits the *smallest* value that ε_L can take is eV, otherwise they will cease to reach the emitter, and for this value $\beta=\beta_c$. Therefore, like the collector families, the emitter $\{n,k\}$ families also do not exist below β_c. They are born when β increases through β_c at the critical boundary simultaneously with the collector family corresponding to the same values of $\{n,k\}$ (see Fig. 20).

When created, the emitter families have nonzero cyclotron energy (see Fig. 20) and can be continuously deformed by transferring cyclotron energy to longitudinal energy, moving the family to higher values of β for fixed total energy. This can only continue until $\varepsilon_L=\varepsilon_0$ and all of the energy is longitudinal, yielding now a *maximum* allowed value of β,

$$\beta_{\mathrm{TO}}=\beta_c[\sqrt{\gamma}+\sqrt{\gamma-1}]. \tag{57}$$

We denote this value by β_{TO} because at this value the $\{n,k\}$ helical emitter family has collapsed to the traversing orbit (which exists and always reaches the emitter for $\gamma>1$). Thus the scenario at $\theta=0$ is that two $\{n,k\}$ families are born at the critical boundary each time β increases through $\beta_c(n,k)$. The collector family moves outwards in the SOS and exists for all $\beta>\beta_c$, whereas the emitter family moves inwards in the SOS and annihilates with the TO at $\beta_{\mathrm{TO}}(n,k)$ (see Fig. 21). The consequence is that each emitter family lives for only a finite interval, $\beta_c<\beta<\beta_{\mathrm{TO}}$. By continuity all the emitter periodic orbits which evolve from these emitter tori (in a manner similar to the SBM) will also live in a finite

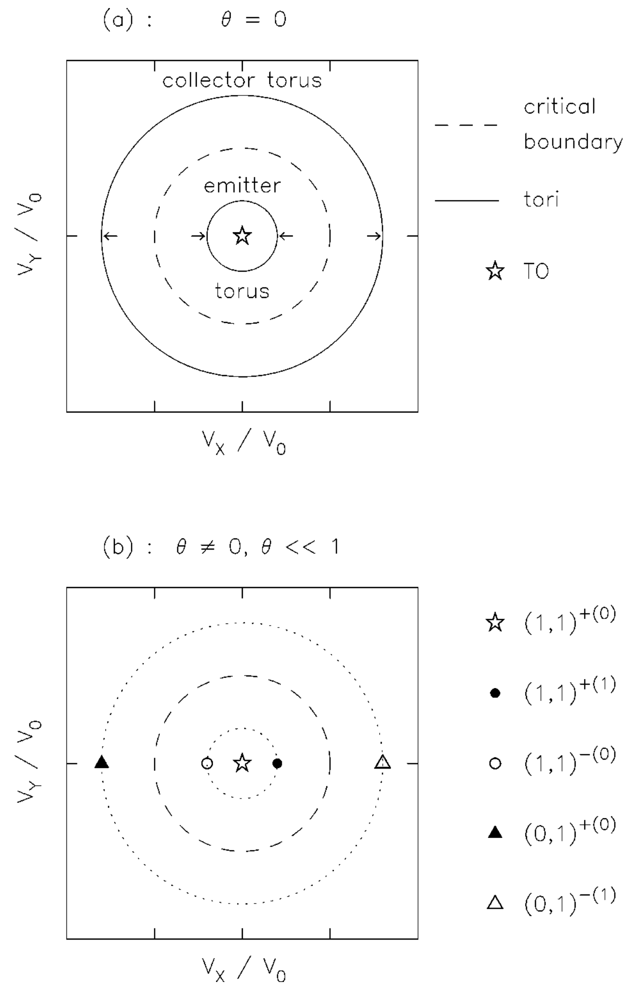

FIG. 21. A schematic representation of (a) the two resonant tori of the period-one orbits at $\theta=0°$ and (b) the surviving orbits at $\theta \ll 1$. The arrows in (a) indicate the direction of the evolution of the resonant tori with the increase of β at constant γ.

interval given approximately by this inequality for small tilt angle. To our knowledge this property of the system has not been demonstrated in the previous literature. As only the emitter orbits will play a major role in the semiclassical theory of the tunneling spectrum (collector orbits make exponentially small contributions), the point is of some significance.

It follows from this argument that as β increases the collector families evolve by transferring longitudinal energy to cyclotron energy in the manner familiar from the SBM, whereas as β increases the new emitter orbits *give up* cyclotron energy to remain in resonance. To understand this less familiar behavior recall that increasing β may be regarded as increasing B with all other parameters fixed. As B increases the cyclotron frequency increases and the longitudinal frequency will need to increase to maintain the resonance condition. As noted already, unlike the collector orbits, for emitter orbits the longitudinal frequency increases with ε_L. The reason for this is that as ε_L increases the electron traverses the fixed distance to the emitter faster and is more rapidly returned to the collector. We will see below that the consequence of this reversal of the dependence on ε_L means that all bifurcations of emitter orbits in the DBM happen in the reverse direction (as a function of β) from the bifurcations of the corresponding orbits in the SBM.

B. Period-one orbits in the DBM

1. Continuity argument

We now analyze the period-one PO's of the DBM for $\theta \neq 0$. Here we mean period-one orbits with respect to iteration of the Poincaré map defined at the collector of the DBM, i.e., the orbits must collide with the collector only once before retracing. For zero tilt angle these orbits will be of three types: (1) the collector orbits corresponding to the $n=1,k=1,2,\ldots$ resonances, which do not collide with the emitter: (2) the emitter orbits corresponding to the $n=1,k=1,2,\ldots$ resonances which do reach the emitter; (3) the traversing orbit, which has zero cyclotron energy and which hence must reach the emitter for $\gamma>1$. The TO has the period

$$T_{\mathrm{TO}}=\frac{\beta}{\omega_c}\left(1-\sqrt{1-\frac{1}{\gamma}}\right). \tag{58}$$

As in the SBM, the helical families of orbits will generate pairs of PO's when $\theta\neq 0$ and by continuity, for infinitesimal tilt angle, the orbits arising from emitter families will be emitter orbits and those arising from collector families will be collector orbits.

We must now classify periodic orbits not only by the number of bounces with the collector, but also by the number of bounces with the emitter. We introduce the generalization of our earlier notation:

$$(1,1)^{\pm(k)} \text{ for the emitter orbits,}$$

$$(0,1)^{\pm(k)} \text{ for the collector orbits,}$$

where the first number in the parentheses denotes the number of collisions with the emitter barrier and the second the number with the collector barrier per period. k is the integer defining the interval as in the SBM; the period of the corresponding orbit is between kT_c and $(k+1)T_c$. This notation is used in Fig. 22.

For infinitesimal tilt angle and $\beta<\beta_c\simeq 2\pi$ there will exist only one period-one orbit, the analog of the TO, which we denote as $(1,1)^{+(0)}$. This orbit differs only infinitesimally from a straight line when $\beta\rightarrow 0$, but gains more cyclotron energy as β is increased, just as in the SBM.

As β is increased to $\approx\beta_c$ *four* new period-one orbits arise in an infinitesimal interval; these are the two nonmixing orbits from each of the collector and emitter $n=1,k=1$ families. Due to the breaking of the symmetry between these two orbits in each family, they are created pairwise at slightly different β values and with slightly different periods. However the corresponding collector and emitter orbits are still born at the same β value in a cusp bifurcation. The two orbits that survive from the period-one collector orbit families are identical to those already discussed in the SBM, they are denoted by $(0,1)^{+(0)}$ and $(0,1)^{-(1)}$, because they are born in different intervals (see Fig. 22) of the period [the period of the orbit $(0,1)^{+(0)}$ is greater than T_c, while the period of $(0,1)^{-(1)}$ is less than T_c]. The period-one collector orbits must be nonmixing by the simple argument given in discussing the SBM. The period-one emitter orbits collide twice in each period and so it is less obvious that they must be nonmixing in their collision with the collector barrier; however, it can be rigorously proved that this must be the case. Therefore, again our continuity argument implies that only the two emitter orbits with $v_y=0, v_x=\pm v_c$ will survive. The one with period shifted slightly down from T_c will be denoted $(1,1)^{-(0)}$; the one with period shifted up will be denoted $(1,1)^{+(1)}$.

Above β_c in the first interval there now exist three period-one orbits, the $(0,1)^{+(0)}$ orbit that does not reach the emitter, the $(1,1)^{-(0)}$ "helical" emitter orbit, and the $(1,1)^{+(0)}$ "traversing orbit," which has the shortest period of the three. As in the SBM, for $\theta\neq 0$ there is no qualitative difference between traversing orbits and helical orbits, since both must have nonzero cyclotron energy. As β increases to $\approx\beta_{\mathrm{TO}}$ [see Eq. (58)], the helical $(1,1)^{-(0)}$ orbit loses cyclotron energy (as would the corresponding orbits at $\theta=0$ discussed above) whereas the $(1,1)^{+(0)}$ orbit gains cyclotron energy. Eventually the two orbits become degenerate and annihilate in a backwards tangent bifurcation, the analog of the annihilation of the $n=1,k=1$ emitter family at $\theta=0$ (see Fig. 22).

At β larger than the value for this TB the $(1,1)^{+(0)}$ orbit does not exist, and this is apparently in contradiction with the behavior of the TO at $\theta=0$ which survives unscathed through the annihilation of the helical family. Moreover, by continuity, for an infinitesimal tilt angle the analog of the (normally) isolated TO must survive at all but a discrete set of values of β. The resolution of this apparent paradox is that, just as in the SBM, an orbit in the next interval, the $(1,1)^{+(1)}$, which is the partner of the $(1,1)^{-(1)}$, takes over the role of the TO at this value of β; see Fig. 22. The same scenario repeats then in the $k=1$ and higher intervals. Note that in this scenario all period-one emitter orbits only survive for a finite interval, being born at some threshold value of β by cusp bifurcation and disappearing at higher β by backwards tangent bifurcation.

The behavior of the period-one orbits for larger tilt angle differs in one important respect. It becomes more and more difficult for the (1,1) orbits to reach the emitter barrier and as a result their intervals of existence in β (which initially fill the entire β axis) shrink monotonically until they go to zero at a critical angle that differs for each interval (see Fig. 23). The only exception is in the first interval where for sufficiently small β it is always possible to have a $(1,1)^{+(0)}$ analogous to the TO of the untilted system. The reason the $(1,1)^{+(0)}$ orbit always exists is that we may regards the limit $\beta\rightarrow 0$ as the limit of vanishing magnetic field, so its tilt can have no effect on the orbit, which does have enough energy to reach the emitter ($\gamma>1$). However, since all other period-one orbits require finite β, tilting the field sufficiently for fixed γ can prevent the electron from reaching the emitter. As these intervals shrink the scenario also changes. Instead of the $(1,1)^{+(k)}$ orbit being created directly by a cusp bifurcation, it is created in a tangent bifurcation as a $(0,1)^{+(k)}$ orbit and then evolves at higher β into $(1,1)^{+(k)}$ orbit. This is the first example of an orbit continuously changing its connectivity with the emitter as a function of β; these events also play a role in the theory of the period-two or period-three orbits, as discussed below.

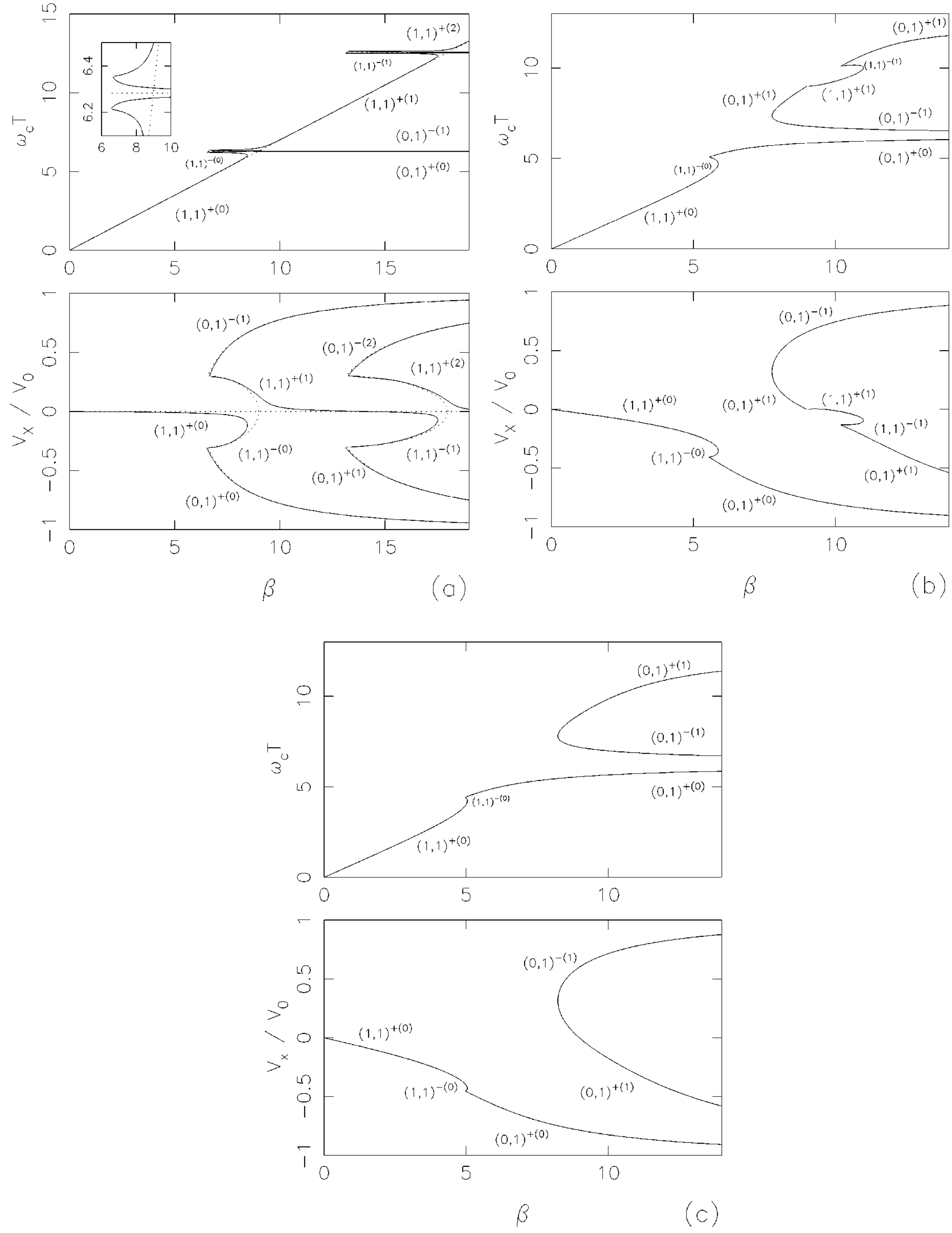

FIG. 22. The scaled period $\omega_c T$ as function of β and the corresponding bifurcation diagrams for the period-one orbits in the double-barrier model at zero tilt angle. The tilt angle (a) $\theta = 0.64°$, (b) 14°, and (c) 25°. $\gamma = 1.17$. The vertical axis in the bifurcation diagrams represents the x component of the scaled velocity of the electron at the point of collision with the collector barrier.

Now we discuss the stability of the period-one orbits. Clearly, the collector $(0,1)^{\pm}$ orbits have identical stability properties as their SBM counterparts. As for the emitter orbits, their stability can also be understood using qualitative arguments similar to the ones we applied in our SBM analysis. Just as in the SBM, in the DBM for zero tilt angle the traversing orbit is stable for any β and γ except when its period is either an integer or a half-integer multiple of the cyclotron period T_c, when it is marginally stable. When the period takes the values $T = kT_c$ the corresponding value of β is $\beta = \beta_{\mathrm{TO}}(1,k)$; when $T = (k + \frac{1}{2})T_c$ the corresponding β values are $\beta = \beta_{\mathrm{ms}}(k) \equiv [1 + (1/2k)]\beta_{\mathrm{TO}}(1,k)$. Therefore, for

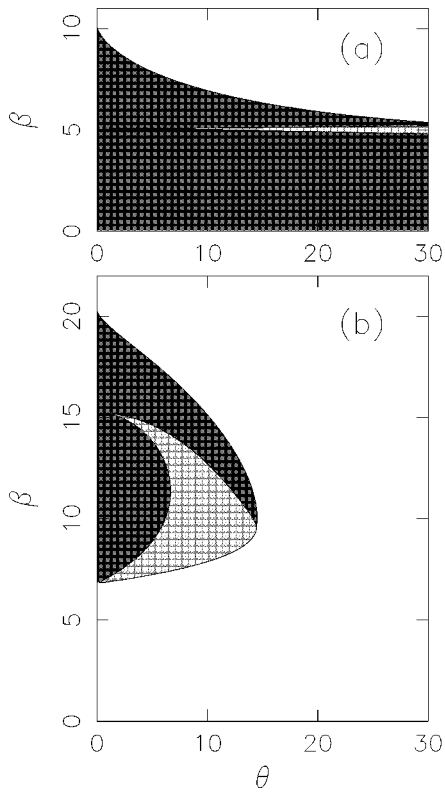

FIG. 23. The intervals of existence of the period-one ''emitter'' orbits shown as shaded areas in the (θ,β) plane for (a) $(1,1)^{+(0)}$ and (b) $(1,1)^{+(1)}$. Dark and light shading represents existing stable and unstable periodic orbits, respectively.

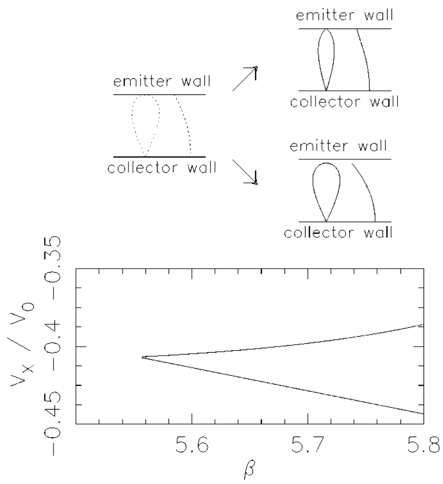

FIG. 24. The bifurcation diagram for the period-one orbits $(1,1)^{-(0)}$ and $(0,1)^{+(0)}$ near the cusp bifurcations. The schematic at the top represents the real space projections of the ''cusp'' orbit exactly at the bifurcation (dotted lines) and the orbits produced by the bifurcation (solid lines).

a small tilt angle the single-bounce orbit which evolved from the TO of the untilted system, can become unstable only near β_{TO} and β_{ms}. In particular, the $(1,1)^{+(0)}$ orbit is stable for small β, but goes unstable and soon restabilizes near $\beta_{\mathrm{ms}}(0)\equiv\pi/(1-\sqrt{1-1/\gamma})$. As in the SBM, this instability for period $\approx T_c/2$ locates the bifurcations involving the important period-two orbits.

Whereas in the SBM the $(1)^{+(0)}$ orbit simply evolves into a helical orbit when $\beta\gg 2\pi$, its analog, the $(1,1)^{+(0)}$ annihilates with the $(1,1)^{-(0)}$ orbit near β_{TO}. Due to the general properties of tangent bifurcations, one of these orbits must be stable, while the other must be unstable. Since the $(1,1)^{+(0)}$ orbit is a deformation of the stable TO it is the stable one just before the TB, while the orbit $(1,1)^{-(0)}$ is unstable. This is illustrated by the plot of the monodromy matrix for these orbits (Fig. 24).

This $(1,1)^{-(0)}$ is worth further consideration because it appears at the critical boundary near $\beta=\beta_c$ in a cusp bifurcation together with the collector orbit $(0,1)^{+(0)}$. By definition of the critical boundary a periodic orbit appearing there has precisely the energy to reach the emitter barrier with zero normal velocity $(v_z=0)$. If β is increased infinitesimally above β_c, this periodic orbit ''breaks up'' into two PO's, one of which reaches the emitter near the previous point of contact, the other of which does not (see schematic, Fig. 25). The bifurcation diagram for this pair of orbits as a function of β will exhibit a cusp at β_c. A detailed analysis of cusp bifurcations is given in Sec. IV B 3 below. Here we simply note that due to the singularity in the Poincaré map at the critical boundary the monodromy matrices defining the stability of the new orbits cannot be uniquely defined at the cusp bifurcation. We will show that, therefore, the two orbits need not be born as unstable-stable pairs as in tangent bifurcations [this is why we have introduced the new term cusp bifurcation[27] (CB)]. Moreover, one can show that of the two orbits born in a CB, the one with the greater number of collisions with the emitter barrier is necessarily unstable. It follows that the orbit $(1,1)^{-(0)}$ is unstable immediately after it is born, and turns out to be unstable over its entire interval of existence until it vanishes in the TB with $(1,1)^{+(0)}$.

These principles allow us to understand the behavior in the next interval as well. The emitter orbit $(1,1)^{+(1)}$ is also born in a cusp bifurcation with the $(0,1)^{-(1)}$ collector orbit and hence is born unstable. Initially it plays the role of the

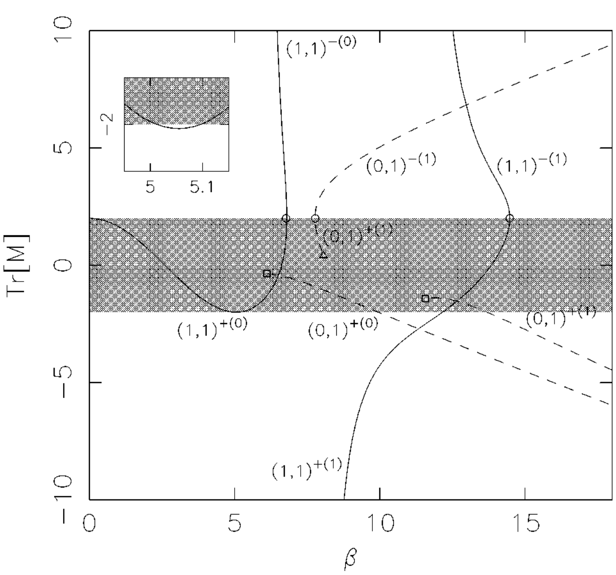

FIG. 25. Trace of monodromy matrix of the period-one orbits of the first two intervals at $\theta=11°$, $\gamma=1.17$. The tangent bifurcations, cusp bifurcations and connectivity transitions are labeled by open circles, open squares, and open triangles, respectively. Shaded area corresponds to the stable region.

''other'' emitter helical orbit. However, near $\beta=\beta_{\rm TO}$ the orbit $(1,1)^{+(1)}$ loses almost all its cyclotron energy (see Fig. 22) and becomes a recognizable deformation of the TO of the untilted system. By continuity, since away from $\beta_{\rm TO}$ the TO was stable, the $(1,1)^{+(1)}$ periodic orbit must restabilize near $\beta_{\rm TO}$. Its further evolution is similar to that of the first interval orbit $(1,1)^{+(0)}$ just discussed. It will bifurcate and then restabilize near $\beta_{\rm ms}(1)$ and later annihilate with the unstable orbit $(1,1)^{-(1)}$ in a tangent bifurcation—see Fig. 24. This scenario is repeated in higher intervals although the first interval of stability [below $\beta_{\rm ms}(1)$] may disappear. We note however, that as long as a $(1,1)^{+(k)}$ orbit exists in each interval, it must have a region of stability just before it annihilates with the $(1,1)^{-(k)}$ orbit (which is always unstable), although these intervals will shrink with increasing tilt angle and k.

2. Exact analysis

The derivation of the periods of the period-one emitter orbits in the DBM can be performed using a technique similar to the one employed for the description of period-two nonmixing orbits in the SBM, since both the emitter and collector bounces are nonmixing. The calculation is given in Appendix G and yields the following equation:

$$\beta^2=\left(\frac{\omega_C T}{2}\right)^2\left(1+\frac{\beta^2}{\gamma(\omega_c T)^2}\,\frac{1-f(\omega_c T)}{1-\cos^2\theta f(\omega_c T)}\right)^2$$
$$+4\sin^2\theta f^2(\omega_c T)$$
$$\times\left(1+\frac{\beta^2}{16\gamma}\,\frac{1}{f(\omega_c T)[1-\cos^2\theta f(\omega_c T)]}\right)^2, \quad (59)$$

where

$$f(x)=1-\frac{x}{4}\cot\left(\frac{x}{4}\right). \quad (60)$$

This is a quadratic equation for β^2 for a given T; it should be solved along with condition (G11), that v_z just before the collision with the emitter is positive, to determine the physically meaningful roots. Solving Eq. (58) together with the condition (G11), one can obtain the dependence $\beta(T)$, which was plotted in Fig. 22 and used to obtain the corresponding bifurcation diagrams. Equation (25) and the condition (G11) imply that $\beta(T)$ is not monotonic in each interval $[(k-1)T_c<T<kT_c$, but always has a single maximum. Therefore it describes *two* different (1,1) orbits, which we already identified as the $(1,1)^{\pm}$ orbits.

Using Eqs. (59) and (G11), one can show, that, as for the period-one orbits in the SBM, for a nonzero tilt angle the period of the (1,1) orbits cannot be equal to integer multiples of the cyclotron period kT_c. Moreover, the period also can not take values too close to kT_c. The width of each of these ''forbidden'' regions in each interval increases (from zero at $\theta=0$) with the increase of tilt angle, so that at some critical angle (which depends on the interval number k) the ''forbidden'' regions originating from $T=(k-1)T_c$ and $T=kT_c$ merge and as already noted, it becomes impossible for the period-one orbits to reach the emitter in this interval of period. When period-one emitter orbits exist in an interval, we can calculate their interval of existence in β from Eqs. (58),(G11). The results for the $(1,1)^{+(0)}$ and $(1,1)^{+(1)}$ orbits are shown in Fig. 23.

One can also calculate the stability properties of the (1,1) orbits as outlined in Appendix H. The results for the trace of the monodromy matrix for different (1,1) orbits are shown in Fig. 24. The qualitative behavior is as discussed above. The key new feature that emerges is an analytic understanding of the cusp bifurcations at the birth of the $(1,1)^-$ and $(0,1)^+$ orbits.

3. Cusp bifurcations and connectivity transitions

First, we note again that *all* relevant emitter orbits are born in cusp bifurcations at the low β side of their existence interval. As shown in Appendix H, the monodromy matrix for the emitter orbit born in a CB involves terms proportional to the inverse of the velocity at the emitter barrier. Since at the cusp bifurcation the emitter velocity goes to zero, the trace of the monodromy matrix of the corresponding orbit will diverge (see Fig. 24). Therefore *all* emitter orbits are extremely unstable just after their appearance in a CB (unless both orbits born in a cusp bifurcation are emitter orbits, in which case the one with greater number of collision with the emitter barrier will be extremely unstable). On the other hand, their companion collector orbits, for β just above the CB no longer ''feel'' the emitter barrier and must have stability properties as in the SBM, where there is no such divergence for any values of β. Therefore the monodromy matrix for this orbit as β is reduced to the CB value does not tend to infinity but tends toward a finite value (see Fig. 24). Whether this value is in the stable region or not depends on the value of the tilt angle and of γ. For large tilt angle the companion collector orbit is typically unstable just above the CB and *two* unstable orbits are born at the CB, in contrast to the generic behavior at tangent bifurcations.

There is an interesting and important variant on the concept of cusp bifurcation. It is possible that orbits may be born as collector orbits in a TB, and lose cyclotron energy with increasing β until at some higher β they reach the emitter and evolve into emitter orbits. We will refer to these events as *connectivity transitions* since the orbit changes its connectivity to the emitter. However, in this case no new orbit is created at the value of β at which the emitter is reached, so this is not a bifurcation point in any sense. Nonetheless, the behavior of the monodromy matrix of this one orbit in the neighborhood of the connectivity transition is similar to that near a CB. The Tr$[M]$ tends to a finite value on the low β side, whereas it diverges at the high β side. For a not too small tilt angle this behavior occurs for the $(0,1)^{+(1)}$ and $(1,1)^{+(1)}$ orbits (see Fig. 24). Interestingly enough, the dynamics does not seem to favor these connectivity changes although they are allowed. For tilt angles larger than a few degrees they are typically replaced by a tangent bifurcation and a new cusp bifurcation that ultimately results in the appearance of an orbit with higher connectivity and the disappearance of one with lower connectivity.

C. Period-two orbits

As in the SBM, the most important set of period-two orbits, for small tilt angles, are those associated with the

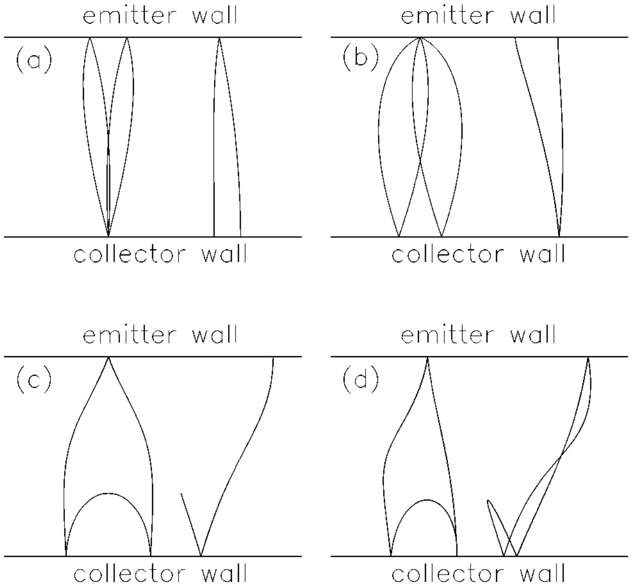

FIG. 26. Examples of the different types of period-two orbits in the DBM, projected onto (x,z) and (y,z) planes: (a) $(2,2)^-$ orbit, (b) $(2,2)^+$ orbit, (c) self-retracing (1,2) orbit, and (d) non-self-retracing (1,2) orbit.

period-doubling bifurcations of the (deformed) traversing orbit $(1,1)^{+(0)}$ which occurs near $T \approx T_c/2$ (so that the relevant period-two orbits have $T \approx T_c$). The scenario for their creation and evolution is in many respects similar to the behavior of the helical period-one orbits just described. For $\theta = 0$ a pair of emitter and collector families are created at the critical boundary at the threshold $\beta_c(n=2,k=1) = \pi\sqrt{\gamma}$. The emitter family loses cyclotron energy with increasing β, moves inward in the SOS and annihilates with the TO at $\beta_{\rm TO}(2,1) = \pi(\gamma + \sqrt{\gamma^2 - \gamma})$. The collector family gains cyclotron energy with increasing β, moves outward, and exists for all β.

When $\theta \neq 0$ two orbits survive from each of the collector and emitter families. These four orbits are born pairwise in two cusp bifurcations involving degenerate collector and emitter orbits, which occur at slightly different values of β. The two collector orbits involved are identical to the nonmixing $(2)^+$ orbit of the SBM and the mixing $(2)^-$ orbit. According to our notation, these collector orbits are denoted as $(0,2)^\pm$. The emitter orbit created in a CB with the nonmixing orbit $(0,2)^+$, which will be referred to as the $(2,2)^+$ orbit (see Fig. 26), has the simplest qualitative behavior and we will discuss it first.

1. $(2,2)^+$ orbits

The period-two emitter orbit, which appears together with the $(0,2)^+$ orbit, at the cusp bifurcation is degenerate with $(0,2)^+$ and has, therefore, the same shape. However, as the parameter β is increased, it begins striking the emitter wall with a nonzero velocity. Since at the point of this collision the angle in the (y,z) plane between the electron velocity and the normal to the barrier is *not* 90°, it is a *mixing collision*. In fact, it can be shown that any orbit in either the SBM or DBM with more than two total collisions must be partially mixing.

As a result of the mixing collision with the emitter barrier this emitter orbit acquires a cusp at the emitter (see Fig. 27). Although this $(2,2)^+$ orbit is mixing in a strict sense, it remains nonmixing at the ''collector'' barrier. Since the magnitude of the velocity is very low at the emitter collision the mixing for this orbit remains very weak.

Whereas the $(0,2)^+$ orbit moves away from the emitter with increasing β in the usual manner, the $(2,2)^+$ orbit transfers more and more energy to longitudinal motion until its ''two legs'' come together and it becomes degenerate with the $(1,1)^+$ traversing orbit. It is then absorbed in a backwards period-doubling bifurcation, causing a change in the stability of the $(1,1)^+$ orbit.

We have already shown by continuity that the $(1,1)^+$ orbit must destabilize and restabilize in a short interval when its period is $\approx T_c/2$. And we have argued that all its bifurcations must be backwards, since in the DBM orbits are born at lower β in cusp bifurcations. Therefore this backwards PDB of the emitter $(2,2)^+$ orbit corresponds to one of these stability changes. To decide which one, we note that although the $(2,2)^+$ orbit must be born unstable because it is the more connected partner in a cusp bifurcation, it should typically be more stable than other period-two orbits which are mixing at the collector, when the velocity is large. Thus, we expect it to restabilize at higher β and, therefore, to restabilize the $(1,1)^+$ orbit when the $(2,2)^+$ orbit is absorbed as a stable period-two orbit in the backwards PDB (see Fig. 28). The exact calculation of the monodromy matrix (see Appendix H for the details) confirms this scenario—see Fig. 29. Furthermore, increasing the tilt angle does not change the scenario for the $(2,2)^+$ orbit, it only reduces its interval of existence. This orbit is relevant in the first peak-doubling region observed at small tilt angles in the data of Muller and co-workers.[12]

2. (1,2) and $(2,2)^-$ orbits

As just noted above, a collector orbit identical to the mixing $(2)^-$ orbit of the SBM [the $(0,2)^-$ orbit] is also created in a cusp bifurcation with an emitter orbit which must have similar morphology. The simplest scenario would have this emitter orbit evolving exactly as did the $(2,2)^+$ orbit, losing cyclotron energy until it is absorbed by the $(1,1)^+$ in the other backwards PDB. However, we can immediately see that this simplest scenario is impossible. The mixing collector orbit $(0,2)^-$ with zero emitter collisions per period and an emitter orbit $(2,2)^-$ with *two* emitter collisions per period can never be created in a *single* cusp bifurcation.

If it were possible, then at the cusp bifurcation these two orbits would have zero *z and y* components of the velocity at two *different* points of collision with the emitter barrier.[35] Since the total kinetic energy of the electron must be the same at any collision with the emitter barrier, this means that the velocities at each of the collisions with the emitter wall will differ only by the sign of v_x. That is possible only for a zero tilt angle, when the system possesses reflection symmetry.

What must happen instead is that the $(0,2)^-$ is born in a cusp bifurcation with an orbit of the type $(1,2)^+$ (see Fig. 26), which infinitesimally above the CB is connected to the emitter at one point and not two. For small tilt angle the reflection symmetry is only weakly broken and the other leg

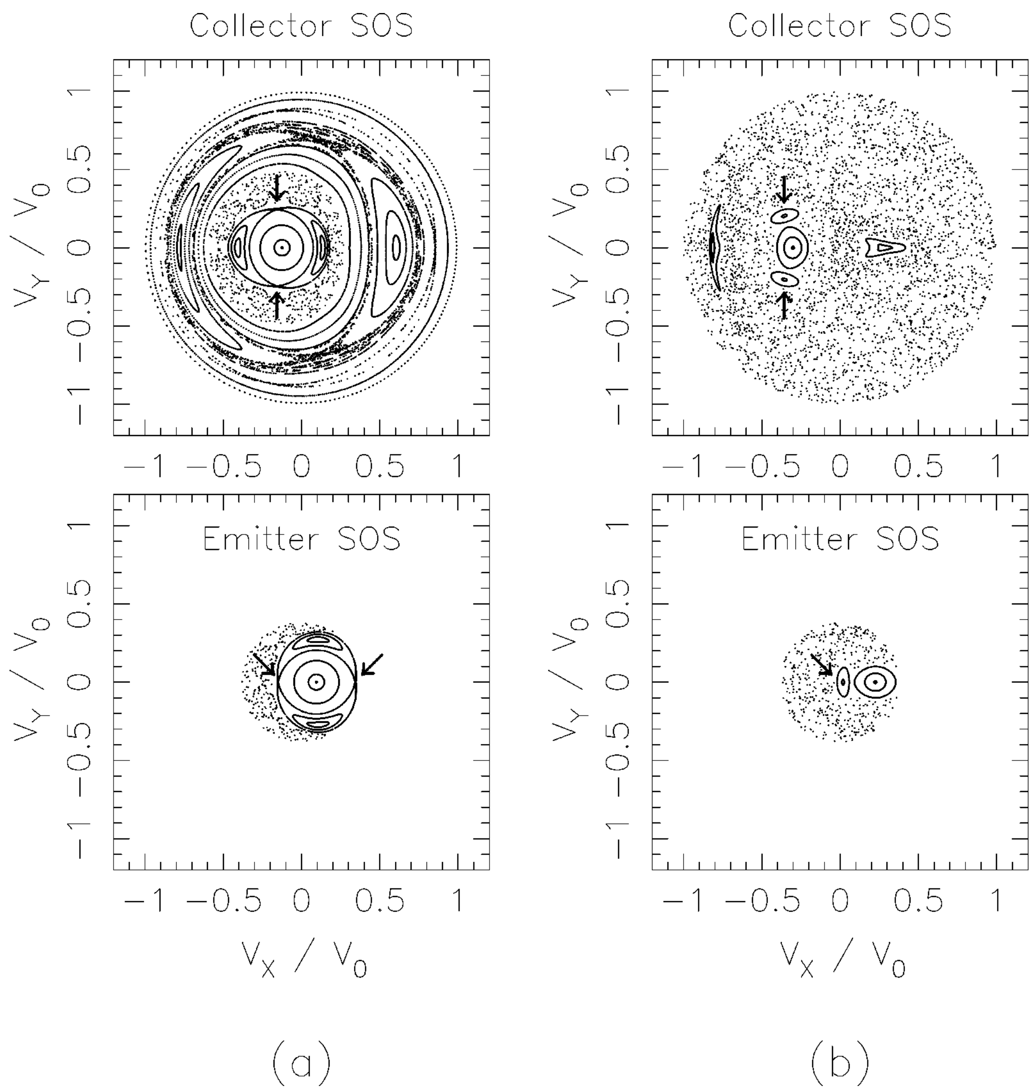

FIG. 27. Surfaces of section, showing the fixed points of $(2,2)^+$, $(0,2)^+$, $(2,2)^-$, and (1,2) orbits for $\beta=4.5$, $\gamma=1.17$ and the tilt angle $\theta=$ (a) 11°, (b) $=28°$. The top and bottom panels correspond to the surfaces of section at the collector and the emitter barriers, respectively. (a) One can clearly see one big stable island of the period-one orbit $(1,1)^+$, and stable islands of the $(2,2)^+$ and $(0,2)^+$ orbits. The stable islands of the $(0,2)^+$ orbit lie at the $\tilde{v}_x \equiv v_x/v_0$ axis at the periphery of the collector surface of section, they are absent at the emitter SOS. The $(2,2)^+$ orbit produces two islands centered on the $\tilde{v}_x$ axis at the collector barrier and two islands at the emitter barrier. To show the $(0,2)^+$ and $(2,2)^+$ orbits in a single bifurcation diagram it is therefore natural to represent these orbits by their values of the x component of the scaled velocity at the collector barrier. The fixed points of the generally unstable orbit $(2,2)^-$ are not so easy to see by an (untrained) eye and are pointed out by the arrows. Both fixed points of $(2,2)^-$ have zero $\tilde{v}_y$ at the emitter barrier and nonzero $\tilde{v}_y$ at the collector barrier. Note, that at the collector barrier the $(2,2)^-$ orbit has the same values of the x component of the scaled velocity [since $\tilde{v}_x \sim y$ and the $(2,2)^-$ orbit strikes the collector wall at the same point]. Therefore, this value is a convenient representation for the $(2,2)^-$ orbits in the bifurcation diagrams. (b) One can see a relatively large stable island of the $(1,1)^+$ orbit, two islands of the $(0,2)^-$ orbit (in collector barrier SOS only) and stable islands of the (1,2) orbit (two islands at the collector barrier surface of section and one island at the emitter barrier SOS). Just as for the $(2,2)^-$ orbit, the fixed points of the (1,2) orbits at the collector SOS have exactly the same values of $\tilde{v}_x$, which can therefore be used as their representation in the bifurcation diagrams.

of this orbit will be quite close to the emitter, but it may not touch. Eventually, the creation of this orbit leads to the creation of a $(2,2)^-$ orbit (see Fig. 26), which is absorbed by the $(1,1)^+$ in a backwards inverse PDB. However the qualitative scenario changes several times with increasing tilt angle and may be quite subtle, with no less than four regimes which are relevant to the recent experiments. Since the orbits involved control much of the peak-doubling behavior at larger tilt angles, we will describe these scenarios in some detail here.

Regime one ($\theta < \hat{\theta}_1$). This regime is described completely by continuity arguments once it is understood that the mixing $(0,2)^-$ collector orbit must pair with a $(1,2)^+$ orbit. As β increases above the threshold $\beta_c \approx \pi\sqrt{\gamma}(1+2k)$ (where $k=0,1,\ldots$ is the interval number) the $(0,2)^-$ and $(1,2)^+$ orbit are created in a CB. In a very small interval of β this $(1,2)^+$ orbit attaches its other leg to the emitter and becomes a $(2,2)^-$ orbit in a connectivity transition of the type described in Sec. IV B 3 above. The $(1,2)^+$ orbit must have

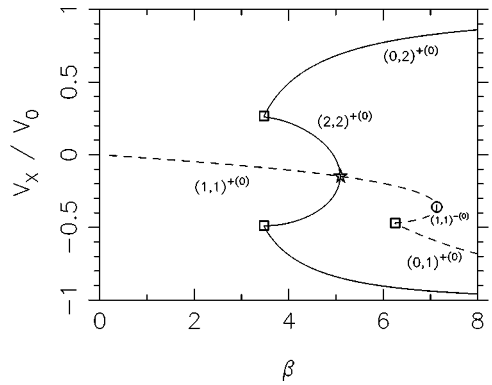

FIG. 28. The bifurcation diagram of the $(2,2)^+$ and $(0,2)^+$ orbits in the DBM. The vertical axis represents x component of the scaled velocity of the electron at the point of collision with the collector barrier [see also Fig. 27(a)] . The tilt angle $\theta = 15°$, and $\gamma = 1.17$. The tangent bifurcations, cusp bifurcations, and period-doubling bifurcation are labeled by open circles, open squares, and an open star, respectively.

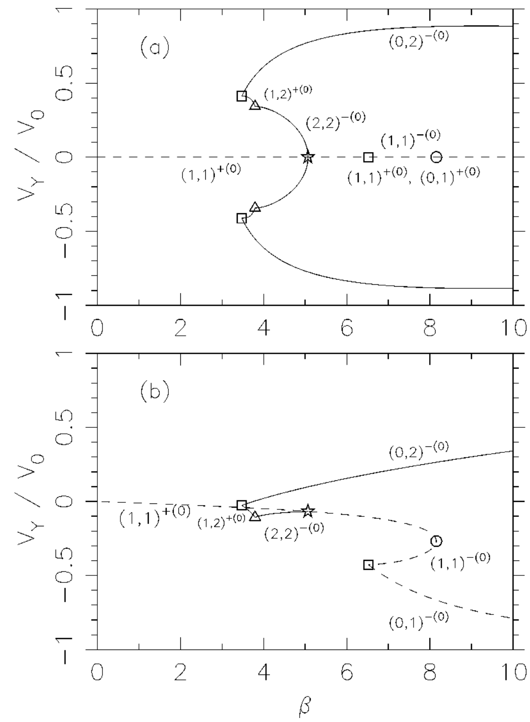

FIG. 30. The bifurcation diagram of the $(2,2)^-$, (1,2), and $(0,2)^-$ orbits in the DBM in ''regime one.'' The vertical axis represents y (top panel) and x (bottom panels) components of the scaled velocity of the electron at the point of collision with the collector barrier [see Fig. 27(b)]; $\gamma = 1.17$; the tilt angle $\theta = 5°$.

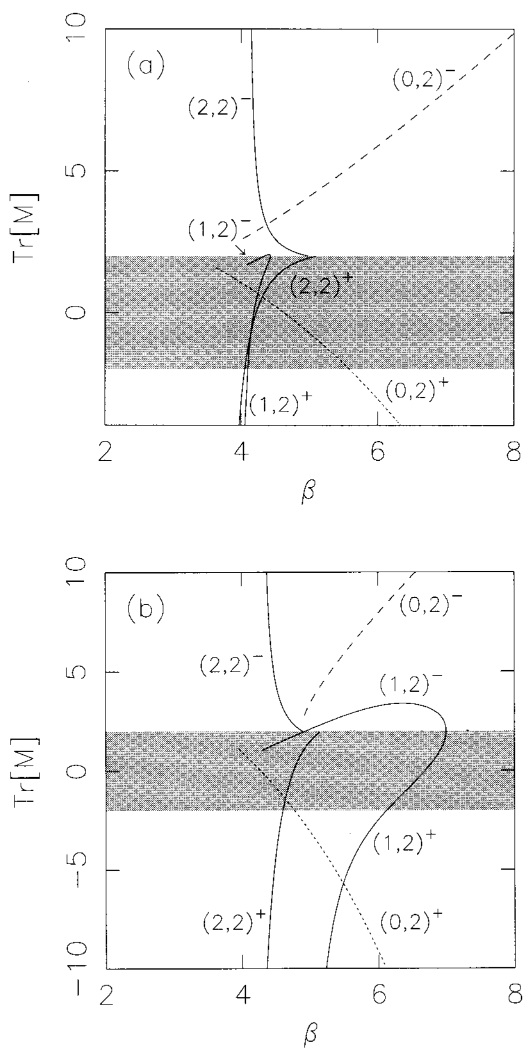

FIG. 29. The trace of monodromy matrix for different period-two orbits of the first interval at (a) $\theta = 17°$ and (b) $\theta = 28°$.

been born unstable at the CB and since the $(0,2)^-$ orbit it creates is mixing at the collector we expect it to remain unstable as it loses cyclotron energy until it is absorbed in a backwards inverse PDB with the $(1,1)^+$ orbit. The $(1,1)^+$ then becomes unstable and is shortly after restabilized by its backwards PDB with the $(2,2)^-$ orbit. All steps are consistent with the continuity argument from $\theta = 0$. The bifurcation diagram in Figs. 30 illustrates the behavior in this regime.

The $(1,1)^+$ continues its evolution until it vanishes in the backwards tangent bifurcation described above and neither creates nor destroys any further period-two emitter orbits. However, there is a new period-two orbit created by the $(0,1)^+$ collector orbit. It behaves just as in the SBM and goes unstable creating a $(0,2)^*$ orbit that is the exact analog of the $(2)^*$ orbit of the SBM. However, this only occurs at large β values and the orbit never reaches the emitter once it is created, so it is not relevant to the experiments at small tilt angle. We mention it because it will become very relevant at large tilt angles.

Regime two ($\hat{\theta}_1 < \theta < \hat{\theta}_2$). The behavior in this regime is as follows. As β increases, as before, the first event is the creation of the $(0,2)^-$ collector orbit and the $(1,2)^+$ orbit via CB. This $(1,2)^+$ orbit evolves for some interval in β without becoming a $(2,2)^-$ and in this interval a second CB occurs in which a distinct orbit $(1,2)^-$ and a $(2,2)^-$ are created—see Fig. 31(a) (this can happen because their connectivity only differs by one). At slightly higher β still the two orbits $(1,2)^+$, $(1,2)^-$ annihilate in a backwards TB and a yet higher β the $(2,2)^-$ orbit is absorbed by the traversing orbit in the now-familiar PDB. The net effect of the creation of this second orbit $(1,2)^-$ is to eliminate the connectivity transition

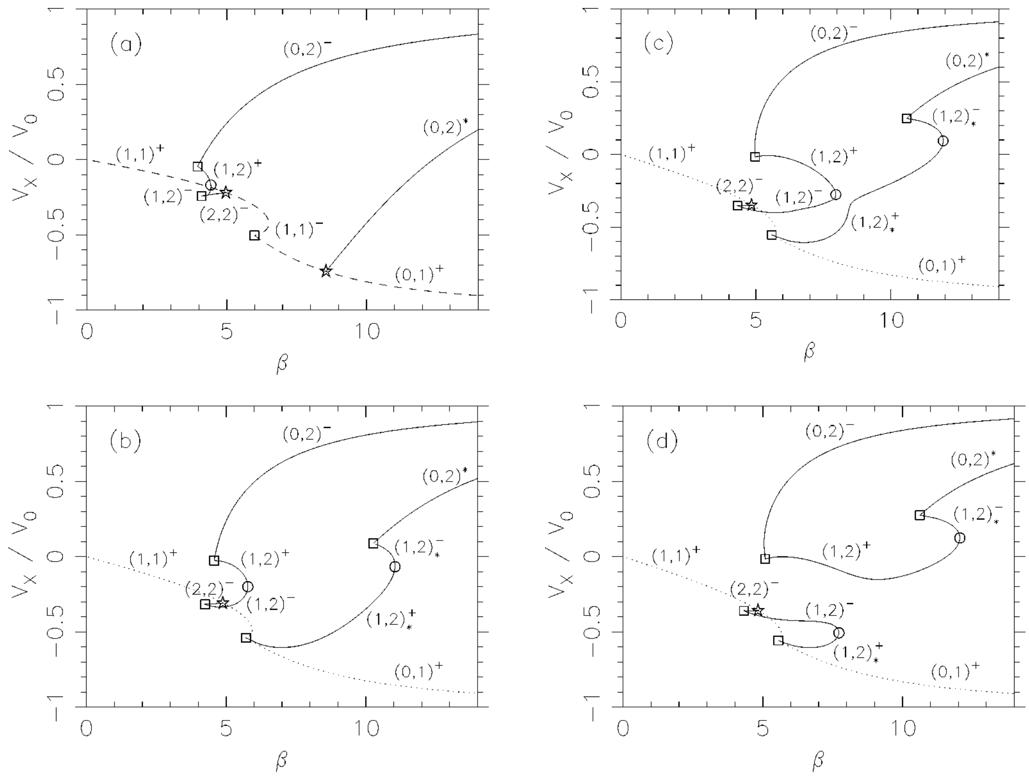

FIG. 31. The bifurcation diagrams of the $(2,2)^-$, (1,2), and $(0,2)^-$ orbits in the DBM in $(\beta, v_x/v_0)$ coordinates [see Fig. 27(b)] in regimes (a) two, [(b),(c)] three, and (d) four; $\gamma=1.17$; the tilt angle $\theta=$ (a) 20°, (b) 27°, (c) 29°, and (d) 30°.

directly from $(1,2)^+$ to $(2,2)^-$. The dynamics seems to rapidly eliminate these transitions even though they are not strictly forbidden; preferring to replace one connectivity transition with a CB and TB which results in the same final state. The total number of (1,2) orbits is increased to two by this change.

Regime three ($\hat{\theta}_2 < \theta < \hat{\theta}_3$). As already mentioned, a further period-two orbit, $(0,2)^*$ is created by the PDB of the $(0,1)^+$ collector orbit, exactly as the $(2)^*$ orbit is created in the SBM. As tilt angle is increased this PDB moves to lower and lower β until at the value $\hat{\theta}_2$, it coincides with the cusp bifurcation that creates the $(1,1)^-$ and $(0,1)^+$ orbits. For larger θ a period-two emitter orbit of type (1,2) is created at this CB. Thus in a somewhat mysterious manner this CB is a ''point of accumulation'' for the creation of higher period orbits (a similar thing happens for period-three here as well). We may call this orbit $(1,2)_*^+$ since it is similar in many ways to the $(2)^*$ orbit of the SBM. For example it has no analog in the untilted system. Just above the critical angle $\hat{\theta}_2$ this $(1,2)_*^+$ orbit is barely reaching the emitter and it rapidly detaches for higher β and becomes a collector orbit. As θ is increased, very quickly this connectivity transition is again replaced by a combination of CB and TB, where in this case the CB involves the $(0,2)^*$ collector orbit and a second $(1,2)_*$ orbit, $(1,2)_*^-$. The orbits $(1,2)_*^+$, $(1,2)_*^-$ then annihilate at higher β in tangent bifurcation —see Figs. 31(b,c). So except for very near the critical angle $\hat{\theta}_2$, there are now a total of four (1,2) orbits associated with the first interval. These are the two $(1,2)_*^{\pm}$ orbits just mentioned, which are connected with the cusp bifurcation of the $(0,1)^+$,$(1,1)^-$ orbits, and the two $(1,2)^{\pm}$ orbits that can be associated with the destabilizing PDB of the $(1,1)^+$ traversing orbit. Therefore, although the scenario is substantially more complicated than in the SBM, the bifurcations of the period-one orbits in the first interval determine all the relevant period-two orbits.

For most of this interval the two $(1,2)^{\pm}$ orbits exist at lower β than the two $(1,2)_*^{\pm}$ orbits. However, as the next critical angle $\hat{\theta}_3$ is approached the intervals of existence of these pairs of orbits begin to overlap and their associated fixed point move together [see Fig. 31(c)]. The final act is about to take place.

Regime four ($\theta > \hat{\theta}_3$). Recall that in the SBM the different branches of the $(2)^*$ and $(2)^-$ orbits linked up above the critical angle $\theta^{\dagger}$. In that case the link was established by the merging of the PDB's at which these orbits were created from the traversing orbit. In the DBM a similar connection now occurs for the $(1,2)_*^+$ and $(1,2)^{\pm}$ orbits via an ''exchange of partners'' bifurcation (note, that we already encountered this bifurcation in the SBM—see the description of three-bounce orbits). The $(1,2)^+$ and $(1,2)_*^-$ orbits are both created at cusp bifurcations with collector orbits [which are identical to the $(2)^-$,$(2)^*$ orbits of the SBM] and are annihilated at tangent bifurcations with their partners $(1,2)^-$,$(1,2)_*^+$. At a critical angle $\hat{\theta}_3$ the $(1,2)^+$ and $(1,2)_*^-$ orbits exchange partners. Above this angle, the $(1,2)^+$ orbit born in CB with the $(0,2)^-$ annihilates in a TB with the $(1,2)_*^-$ orbit born in a CB with the $(0,2)^*$; whereas the $(1,2)^-$ orbit born in a CB with the (one and only) $(2,2)^-$ orbit now annihilates with the $(1,2)_*^+$ orbit born at the CB of the period-one orbits—see Fig. 31(d).

In the experiments of Ref. 12 one of the most puzzling features of the observed peak doubling is that a large region of peak-doubling is seen[36] to separate around $\theta > 30°$. It is now clear that this reseparation is initiated by the ''exchange of partners'' bifurcation described above. This will be demonstrated quantitatively using the semiclassical tunneling formula (1).[16]

After the ''exchange of partners'' transition the $(1,2)^+$ orbit exists for a very large interval of β and has relatively low cyclotron energy. Thus it plays a dominant role in the tunneling spectrum in this interval of β. The importance of this orbit has been emphasized in work of Fromhold.[10]

In contrast, the other pair of orbits, $(1,2)^-,(1,2)^+_*$, decrease their interval of existence because the PDB and CB to which they are connected move together.

In Fig. 29 we show the behavior of the trace of the monodromy matrix for different period-two orbits. Note that the orbit $(1,2)^-$ remains near marginal stability in the whole interval of its existence. This is an unusual dynamical property, not shared by the other period-two orbits in its family, nor by typical unstable orbits, e.g., in chaotic billiards. It is now well known that unstable periodic orbits that are close to stability are most likely to generate nonergodic quantum states concentrated in real and phase space along these orbits (''scarred wave functions'').[37–39] Therefore orbits such as the $(1,2)^-$, which are ''pinned'' near marginal stability while the classical parameters of the system are varied, can generate many scars of the same orbit. We have argued elsewhere[24] that this special dynamical property of the tilted well explains the existence of the long sequence of wave functions scarred by the same orbit found numerically.[11] Only certain orbits in each family can participate in this anomalous scarring; we will point out examples for the period-three and period-five orbits below.

To summarize the complicated story of the period-two orbits: For small tilt angles the important orbits are the (2,2) orbits we have denoted as $(2,2)^{\pm}$ orbits. As tilt angle increases the importance of (1,2) orbits increases and eventually they become the dominant period-two orbits in the first interval. Since higher intervals correspond to greater chaoticity, they become important more quickly in the second interval. These (1,2) orbits are created in a complicated bifurcation tree that connects to a period-doubling bifurcation of the period-one traversing orbit, as well as cusp bifurcations with various period-one and period-two collector orbits. It is very difficult to discern these relationships from simple observations of the SOS as many of these orbits are born highly unstable in cusp bifurcations and certain of the transitions described occur over very small angular intervals.

D. Period-three orbits

All of the qualitative differences between the periodic orbit theory of the SBM and that of the DBM already have entered into the description of the period-one and two orbits. However, peak-tripling regions have been clearly observed in experimental tunneling spectra, indicating that the behavior of period-three orbits is relevant to these experiments. Moreover, there has been a recent Comment questioning the interpretation proposed for these peak-tripling regions[22,23] in Ref. 12, where they were attributed to trifurcations of the traversing orbit. Since we are able to reach a complete understanding of these orbits based on the principles used in discussing the period-one and two orbits, we will briefly summarize their properties.

As for the period-two orbits, for small tilt angles the main period-three orbits are those related to the resonances of the traversing orbit. When the tilt angle is exactly zero, the traversing orbit has *two* 1:3, resonances in each interval, when its period is equal to $(3k+1)T_c/3$ and $2(3k+1)T_c/3$, respectively. The behavior near each of these resonances is essentially the same for small tilt angles, so we just consider the first one. First, an emitter and collector family is created at the critical boundary at $\beta_{c1} < \beta_1$. The emitter family moves inwards in the SOS and collapses to the TO at resonance. When the field is tilted only two period-three orbits survive from each emitter family and they are now created in cusp bifurcations with the corresponding collector families at slightly different values of β.

As with the period-two orbits in the DBM, these emitter orbits will move inwards in the SOS until they annihilate. The one difference in their behavior has already been noted in the discussion of of the SBM (see Sec. III E). Because period-three orbits generically are not born or absorbed in bifurcations with a period-one orbit, these two orbits cannot disappear precisely on resonance with the TO. Instead one of them (the unstable one) passes through the fixed point associated with the $(1,1)^{+(k)}$ traversing orbit in a touch-and-go bifurcation and then annihilates with the other in a backward tangent bifurcation. For all tilt angles the interval between the TAG bifurcation and the TB is negligibly small, and so practically speaking it is as if these two orbits vanish in a ''backwards trifurcation.''

Again, as with the period-two orbits, for finite tilt angle the emitter orbits cannot be created as (3,3) orbits at the initial cusp bifurcation. Therefore the two emitter orbits just described are created in the form of a (1,3) and a (2,3) orbit. These orbits are the analogs of the period-two (1,2) orbits, but now there are two different types of orbits with less than the maximum (3,3) connectivity to the emitter. In y-z projection the (3,3) orbits each have a mixing collision point (where two collisions occur) and a nonmixing collision point (where only one collision occurs, see Fig. 32.) The (1,3) orbits correspond to detaching the orbit at the mixing collision point, the (2,3) orbits correspond to detaching it at the nonmixing collision point. As noted, both occur for each resonance.

For small tilt angles the (1,3) and (2,3) orbits created at these cusp bifurcations evolve by connectivity transitions into the stable and unstable (3,3) orbits which participate in the TAG/TB behavior already described. At higher tilt angles, as for the period-two orbits, the connectivity transitions are replaced by the appearance of a new (1,3) and (2,3) orbit that through a combination of CB and TB leads to the same final state. In the regime of small tilt angle there are six period-three orbits created in the neighborhood of each resonance: two collector orbits, a (1,3), a (2,3), and two (3,3) orbits. For large tilt angles there are *eight* period-three orbits due to the new (1,3) and (2,3) orbits that arise to replace the connectivity transitions (see Fig. 33). The bifurcation diagrams of Fig. 33 summarize the behavior of the family of period-three orbits related to the first resonance; qualitatively the same behavior is observed at the second resonance as

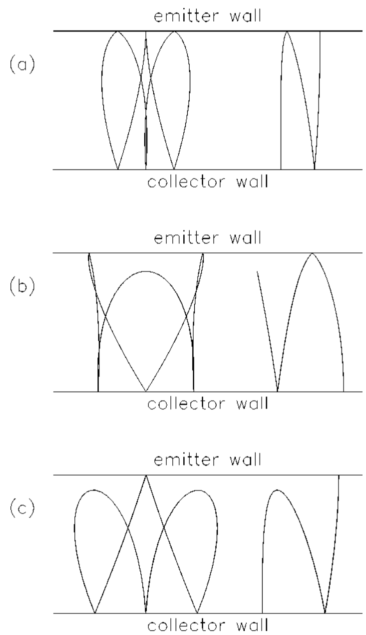

FIG. 32. Examples of the different types of period-three orbits in the DBM, projected onto (y,z) planes: (a) (3,3) orbit, (b) (2,3) orbit, (c) (1,3) orbit.

well. In Fig. 34 we show the behavior of the trace of the monodromy matrix for these orbits. Note, that as for the period-two orbits, there is one orbit which, although exists in a substantial interval, does not become too unstable [the orbit $(1,3)^-$] and is therefore expected to produce strong scars.

The (1,3) and (2,3) orbits in each family appear at lower magnetic field than the resonance value, and evolve either directly or indirectly into the (3,3) orbits. One of these orbits has been identified previously by Fromhold and co-workers[21,22] in connection with peak tripling. We have recently shown that this orbit satisfies the same criteria for generating strong scars in the quantum wave functions as does the period-two orbit discussed above.[24] We will analyze the relation of the entire family to the experimental observations elsewhere. We simply point out here that each family of eight period-three orbits is connected to a period-three resonance through bifurcation processes, and in the scheme presented in this paper they arise as a natural consequence of that resonance.

As noted, for small tilt angles both resonances between the period-three and period-one orbits in the first interval are similar, with the creation of six or eight period-three orbits, four of which are related by continuity to tori of the unperturbed system. As with the period-two orbits, there is another resonance corresponding to $T \approx 3T_c$ that occurs in the first interval, but initially for very high β. This resonances will give rise to (1,3) and (2,3) orbits analogous to the $(1,2)^*$ period-two orbits. For small tilt angles they are created near the (0,1) collector orbit and do not reach the emitter, as happened also for the $(1,2)^*$. Just as for that case, as tilt angle is increased the resonance moves ''down'' to the period-one cusp bifurcation and now gives rise to emitter orbits. These emitter orbits then evolve similarly to the $(1,2)^*$ orbits with exchange of partner bifurcations, etc. However, the periods of these orbits $(T>2T_c)$ apparently

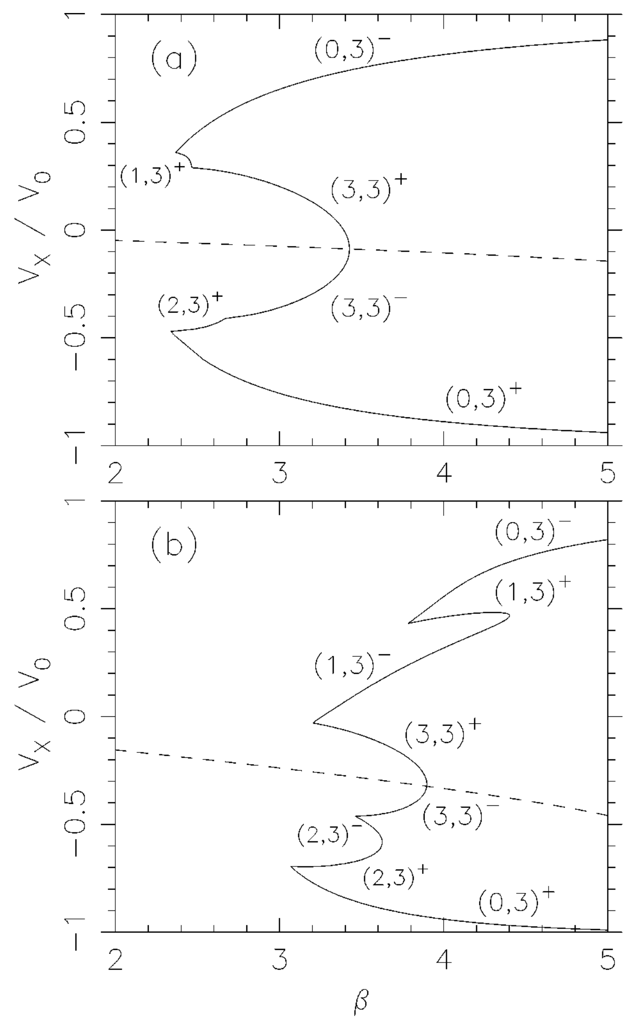

FIG. 33. The bifurcation diagrams of the period-three orbits in the DBM, at $\gamma = 1.17$, $\theta =$ (a) 11°, (b) 38°.

are too long for them to be resolved as resonance peaks in the experimental data of Ref. 12.

Higher period orbits also appear in families in connected bifurcation sequences which begin with collector orbits and end with fully connected emitter orbits which are annihilated at resonances with the TO. The principles and analytic relations we have derived can be used to develop a quantitative theory of such orbits. We have done this elsewhere[24] for the case of a period-five orbit of the (1,5) topology, which is expected to cause anomalously strong scarring. Here we restrict ourselves to the relevant orbits of the DBM with periods less than four, their properties are summarized in Table II.

V. SUMMARY AND CONCLUSIONS

We have developed a complete qualitative and quantitative theory of the periodic orbits relevant to the magnetotunneling spectra of quantum wells in tilted magnetic field.

First we introduced two model Hamiltonians and showed how to scale the variables so that only one or two dimensionless parameters $\beta;(\beta,\gamma)$ describe the classical dynamics at fixed θ. As $\gamma = \epsilon_0 / eV$ is approximately constant in experiments, the dependences on magnetic field, voltage and injection energy are all summarized by the behavior of the Poin-

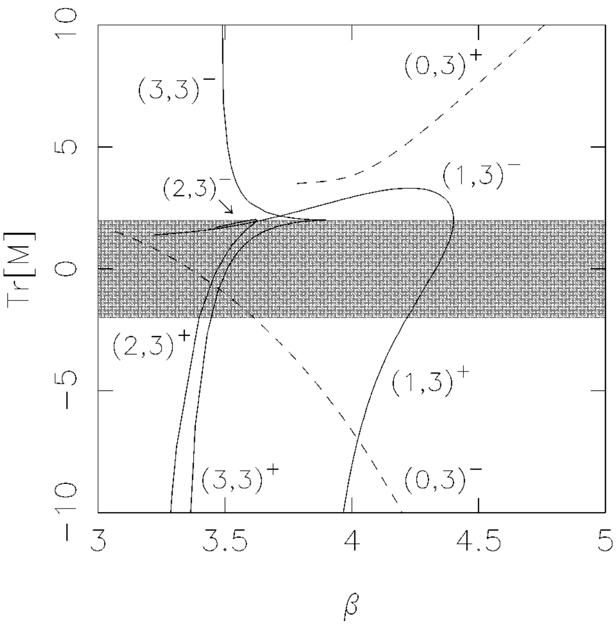

FIG. 34. The trace of monodromy matrix for different period-three orbits related to the first 1:3 resonance of the traversing orbit $(1,1)^{+(0)}$ at $\theta = 17°$.

TABLE II. Relevant periodic orbits in the DBM

orbit	y–z projection	"birth" ←→ "death"
$(1,1)^{\pm}$	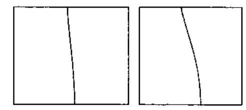	CB ←→ TB
$(2,2)^{+}$	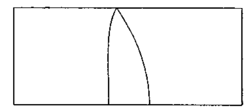	CB ←→ PDB
$(2,2)^{-}$	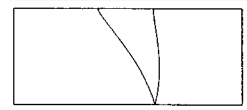	CB ←→ PDB
$(1,2)^{\pm}$	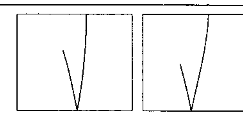	CB ←→ TB
$(3,3)^{\pm}$	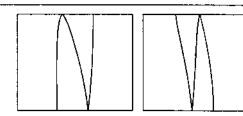	CB ←→ TB
$(1,3)^{\pm}$	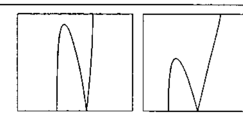	CB ←→ TB
$(2,3)^{\pm}$	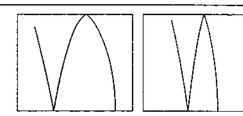	CB ←→ TB

caré velocity map as a function of the variables β, θ.

The theory of the periodic orbits was first developed for the single-barrier model, which elucidates many of the qualitative features of the system. In particular, the SBM describes a standard KAM transition to chaos as a function of tilt angle. The period-one orbit with the smallest cyclotron energy (the traversing orbit) plays a fundamental role in the transition, with the relevant periodic orbits appearing through the bifurcations of this orbit. These bifurcations follow the known bifurcation rules for generic (2D) conservative maps. However, the detailed scenario for the bifurcations evolves with tilt angle in a complicated manner, which nonetheless can be understood using continuity arguments. Exact analytic expressions for the period and stability of most of the relevant orbits were obtained for all parameter values, something that has not been possible for other experimentally studied chaotic quantum systems. We note again that the SBM could be realized in a practical double-barrier structure in which the band profiles were chosen to reduce the emitter energy appropriately.

In generalizing the theory to the double-barrier model that is relevant to the present generation of experiments we uncovered several new features of the dynamics. Perhaps most interesting was the discovery that *all* relevant orbits (except the traversing orbit) are created in a new kind of bifurcation, called a cusp bifurcation, which can violate generic bifurcation rules due to the discontinuity in the Poincaré map on the curve separating initial conditions that reach the emitter from those that do not. These orbits are created in families below the value of β at which resonances with the traversing orbit occur. They only exist for a finite interval of β (or magnetic field) and then annihilate in backwards bifurcations with the traversing orbit or in tangent bifurcations. In a given family of period-N orbits (N collisions with the collector per period) there will exist orbits with $0,1, \ldots N$ emitter collisions, connected together by one or more bifurcation ''trees.'' Typically, several orbits in a given family will be relevant for understanding the magnetotunneling spectra, with their relative importance changing as a function of tilt angle.

Having determined the periods and stability of all the orbits that are short enough to resolve in the experimental tunneling spectra, we can now calculate the tunnel current semiclassically using Eq. (1) from Ref. 16 above and compare to experiment. We have reported initial results of this semiclassical theory in comparison to the experiments of Muller *et al.* elsewhere.[16] Many features of the complicated evolution of the observed spectra with increasing tilt angle find a natural explanation in this approach. The ability to develop a semiclassical theory in essentially analytic form makes this system unique among the few quantum systems which have been studied experimentally in the transition regime to chaos.

ACKNOWLEDGMENTS

The authors wish to thank G. Boebinger, T. M. Fromhold, H. Mathur, T. Monteiro, and D. Shepelyansky for helpful discussions. We particularly thank T. Monteiro for pointing out to us the importance of the (1,2) orbits even at tilt angles as small as 11°, and for making us aware that the period-three bifurcations follow the touch-and-go scenario. The work was partially supported by NSF Grant No. DMR-9215065. We also acknowledge the hospitality of the Aspen Center for Physics where some of this work was done.

APPENDIX A: THE MONODROMY MATRIX FOR THE SINGLE-BOUNCE PERIODIC ORBITS

In this appendix we derive the expressions for the components and the trace of the monodromy matrix for the period-one orbits in the single-barrier model. By definition, the monodromy matrix $M=(m_{ij})$ of a period-one orbit is the matrix, which represents the linearized Poincaré map, calculated at the position of the single-bounce periodic orbit $(\tilde{v}_x^*, \tilde{v}_x^*)$ in the Poincaré surface of section:

$$\Phi_x(\tilde{v}_x^* + \delta\tilde{v}_x, \tilde{v}_x^* + \delta\tilde{v}_x) = \tilde{v}_x^* + m_{11}\delta\tilde{v}_x + m_{12}\delta\tilde{v}_y + O((\delta\tilde{v}_x)^2, (\delta\tilde{v}_y)^2, (\delta\tilde{v}_x)(\delta\tilde{v}_y)),$$

$$\Phi_y(\tilde{v}_x^* + \delta\tilde{v}_x, \tilde{v}_x^* + \delta\tilde{v}_x) = \tilde{v}_y^* + m_{21}\delta\tilde{v}_x + m_{22}\delta\tilde{v}_y + O((\delta\tilde{v}_x)^2, (\delta\tilde{v}_y)^2, (\delta\tilde{v}_x)(\delta\tilde{v}_y)). \tag{A1}$$

The monodromy matrix m_{ij} therefore relates to each other the deviation $\delta\tilde{\mathbf{v}}$ from the location of the periodic orbit after one iteration of the Poincaré map to the initial deviation $\delta\tilde{\mathbf{v}}_0$ in the limit $|\delta\tilde{\mathbf{v}}|\to 0$:

$$\begin{pmatrix} \delta\tilde{v}_x \\ \delta\tilde{v}_y \end{pmatrix} = \begin{pmatrix} m_{11} & m_{12} \\ m_{21} & m_{22} \end{pmatrix} \begin{pmatrix} (\delta\tilde{v}_x)_0 \\ (\delta\tilde{v}_y)_0 \end{pmatrix} + O(\delta\tilde{v}_0^2). \tag{A2}$$

Expanding the Poincaré map (14) in $\delta\tilde{\mathbf{v}}$, we obtain

$$\Phi_x(\tilde{v}_x^* + \delta\tilde{v}_x, \tilde{v}_x^* + \delta\tilde{v}_x) = \tilde{v}_x^* + \delta T\left[\frac{\sin\theta\,\omega_c T^*}{\beta}\cos(\omega_c T^*) - \left(\tilde{v}_x^* + \frac{2\sin\theta}{\beta}\right)\sin(\omega_c T^*)\right] + (\delta\tilde{v}_x)_0\left(\cos(\omega_c T^*) - \frac{\sin\theta\,\beta\tilde{v}_x^*}{\omega_c T^*}\sin(\omega_c T^*)\right) - (\delta\tilde{v}_y)_0\cos\theta\sin(\omega_c T^*) + O((\delta\tilde{v}_x)_0^2, (\delta\tilde{v}_y)_0^2, (\delta\tilde{v}_x)_0(\delta\tilde{v}_y)_0), \tag{A3}$$

$$\Phi_y(\tilde{v}_x^* + \delta\tilde{v}_x, \tilde{v}_x^* + \delta\tilde{v}_x) = \tilde{v}_y^* + \omega_c\delta T\cos\theta\left[\left(\tilde{v}_x^* + \frac{2\sin\theta}{\beta}\right)\cos(\omega_c T^*) + \sin\theta\sqrt{1-(\tilde{v}_x^*)^2}\sin(\omega_c T^*) - \frac{2\sin\theta}{\beta}\right] + (\delta\tilde{v}_x)_0\cos\theta\left(\sin(\omega_c T^*) - \frac{\tilde{v}_x^*\sin\theta}{\sqrt{1-(\tilde{v}_x^*)^2}}[1-\cos(\omega_c T^*)]\right) + (\delta\tilde{v}_y)_0[\cos^2\theta\cos(\omega_c T^*) + \sin^2\theta] + O((\delta\tilde{v}_x)_0^2, (\delta\tilde{v}_y)_0^2, (\delta\tilde{v}_x)_0(\delta\tilde{v}_y)_0), \tag{A4}$$

where the parameter δT is the difference between the time interval to the next collision of the electron with the barrier $T(\beta,\theta;\tilde{v})$ and the period of the single-bounce periodic orbit T^*:

$$T(\beta,\theta;\tilde{v}) = T^*(\beta,\theta) + \delta T. \tag{A5}$$

To obtain the linearization of the Poincaré map in terms of the velocity deviations, we therefore need to calculate the expansion of δT in $(\delta\tilde{v}_x)_0$ and $(\delta\tilde{v}_y)_0$ up to linear order. This result can be obtained from Eq. (16), which relates the scaled in-plane components of the velocity of the electron $(\tilde{v}_x, \tilde{v}_y)$ at the point of collision with the barrier to the time interval T to the next collision. Substituting the expression (A5) into Eq. (16), we obtain

$$\omega_c\delta T = -\frac{\sin\theta[1-\cos(\omega_c T^*)] + \beta\tilde{v}_x^*\left(\cos^2\theta + \sin^2\theta\,\frac{\sin(\omega_c T^*)}{\omega_c T^*}\right)}{\frac{\omega_c T^*}{\beta}[\cos^2\theta - \sin^2\theta\cos(\omega_c T^*)] + \sin\theta\sin(\omega_c T^*)\left(\tilde{v}_x^* + \frac{2\sin\theta}{\beta}\right)}(\delta\tilde{v}_x)_0 + \sin\theta\cos\theta\frac{\omega_c T^* - \sin(\omega_c T)}{\frac{\omega_c T^*}{\beta}[\cos^2\theta - \sin^2\theta\cos(\omega_c T^*)] + \sin\theta\sin(\omega_c T^*)\left(\tilde{v}_x^* + \frac{2\sin\theta}{\beta}\right)} \times(\delta\tilde{v}_y)_0 + O((\delta\tilde{v}_x)_0^2, (\delta\tilde{v}_y)_0^2, (\delta\tilde{v}_x)_0(\delta\tilde{v}_y)_0). \tag{A6}$$

Substituting Eq. (A6) into Eqs. (A3),(A4) and using Eq. (37), the monodromy matrix, we obtain

$$m_{11}=\sin^2\theta+\cos^2\theta\cos(\omega_c T^*)-2\sin^2\theta\cos^2\theta\left(1-\frac{\omega_c T^*}{\tan(\omega_c T^*)}\right)\left(1-\frac{\sin(\omega_c T^*)}{\omega_c T^*}\right),$$

$$m_{12}=-\cos\theta[\sin^2\theta\omega_c T^*+\cos^2\theta\sin(\omega_c T^*)],$$

$$m_{21}=\cos\theta\sin(\omega_c T^*)+\frac{4\sin^2\theta\cos\theta}{\omega_c T^*}\left(1-\frac{\frac{\omega_c T^*}{2}}{\tan\left(\frac{\omega_c T^*}{2}\right)}\right)$$

$$\times\left[1-\cos(\omega_c T^*)-\left(1-\frac{\frac{\omega_c T^*}{2}}{\tan\left(\frac{\omega_c T^*}{2}\right)}\right)\left(\cos^2\theta+\sin^2\theta\frac{\sin(\omega_c T^*)}{\omega_c T^*}\right)\right],$$

$$m_{22}=m_{11}, \tag{A7}$$

and the trace of the monodromy matrix is therefore

$$\mathrm{Tr}(M)=2m_{11}. \tag{A8}$$

For the analysis of the stability of the single-bounce periodic orbits it is convenient to represent the expression for $\mathrm{Tr}(M)$ as a sum of -2 (which is the critical value of the trace of the monodromy matrix, when the periodic orbit bifurcates and loses stability), and an additional term. A trivial rearrangement of terms yields

$$\mathrm{Tr}(M)=-2+4\cos^4(\theta)(\tan^2(\theta)+(\omega_c T^*/2)\cot(\omega_c T^*/2))$$
$$\times[\tan^2(\theta)+\sin(\omega_c T^*)/(\omega_c T^*)], \tag{A9}$$

which is exactly Eq. (43).

APPENDIX B: PERIOD-DOUBLING BIFURCATIONS OF SINGLE-BOUNCE ORBITS AND THE SCALING OF THE POINCARÉ MAP

In this appendix we consider the evolution of the single-bounce orbits $(1)^{+(k)}$, which appear in tangent bifurcations together with the unstable orbits $(1)^{-(k)}$. As follows from Eqs. (43) and Eq. (39), immediately after the tangent bifurcation all $(1)^{+(k)}$ orbits are stable $[-2<\mathrm{Tr}(M)\leqslant 2$—see Fig. 8].

At $\beta=\beta_{\mathrm{b1}}^{(k)}$, where

$$\beta_{\mathrm{b1}}^{(k)}=\mathcal{F}(\sin\theta,\iota_k(-\tan^2\theta)); \tag{B1}$$

the function $\mathcal{F}$ is defined in Eq. (41) and $\iota_k(a)$ is the kth positive root of the equation

$$\frac{\iota}{\tan\iota}=a, \tag{B2}$$

the trace of the corresponding monodromy matrix reaches the value -2, and the orbit $(1)^{+(k)}$ goes unstable via a period-doubling bifurcation. At that moment a new stable two-bounce periodic orbit with the period exactly twice the period of $(1)^{+(k)}$ is born in the neighborhood.

However, although *all* one-bounce periodic orbits $(1)^{+(k)}$ $(k=0,\ldots,\infty)$ show the period-doubling bifurcation at $\beta=\beta_{\mathrm{b1}}^{(k)}$, the further evolution of the $(1)^{+(k)}$ periodic orbits depends on θ and k and is qualitatively different for $\theta<\theta_k^\dagger$ and $\theta\geqslant\theta_k^\dagger$, where

$$\theta_k^\dagger=\arctan(\sqrt{-\sin(\xi_k)/\xi_k}) \tag{B3}$$

and ξ_k is the $(k+1)$th positive root of the equation $\tan(\xi)=\xi$.

Note, that since critical angle $\theta_k^\dagger$ is a monotonically decreasing function of k for a fixed value of the tilt angle θ, the inequality $\theta<\theta_k^\dagger$ is equivalent to the condition $k<k_{\min}(\theta)$, where the integer $k_{\min}(\theta)$ is the smallest integer value of k, for which the inequality $\theta_k^\dagger<\theta$ still holds. $k_{\min}(\theta)$ is a decreasing function of θ, it diverges as integer$(1/\theta)$ at $\theta\to 0$, and $k_{\min}(\theta)=0$ for $\theta>\theta_0$. The regime $\theta<\theta_k^\dagger$ corresponds to $k\leqslant k_{\min}(\theta)$, and $\theta>\theta_k^\dagger$ holds for $k\geqslant k_{\min}(\theta)$ (hence an for arbitrary θ at sufficiently high β the system is in the regime $\theta>\theta_k^\dagger$).

First, we consider the case $k<k_{\min}$ (which is nongeneric in a sense that it corresponds to a *finite* part of an *infinite* sequence $k=0,\ldots,\infty$). At $\beta=\beta_{\mathrm{b2}}^{(k)}$, where

$$\beta_{\mathrm{b2}}^{(k)}=\mathcal{F}(\sin\theta,\wp(-\tan^2\theta)) \tag{B4}$$

and $\wp_n(a)$ is the nth positive root of the equation

$$\frac{\sin\wp}{\wp}=a; \tag{B5}$$

the trace of the monodromy matrix of the one-bounce periodic orbit $(1)^{+(k)}$ again passes through the value -2 (see

Fig. 8). At this point, the orbit $(1)^{+(k)}$ restabilizes via a period-doubling bifurcation. In this bifurcation, the period-one orbit $(1)^{+(k)}$ can either ''emit'' an unstable two-bounce orbit or absorb a stable two-bounce orbit. A detailed description of this behavior is given in Sec. III D, where we analyze the properties of the two-bounce orbits.

As follows from the Eqs. (42) and (B1), for a fixed tilt angle θ the intervals of stability of the single-bounce orbits $(1)^{+(k)}$ at large k scale as $1/k$. If we introduce an effective ''local'' parameter β_ℓ such that

$$\beta_\ell = k[\beta - \pi(2k+1)], \tag{B6}$$

then in the limit $k \gg 1$ the values of this local parameter corresponding to the bifurcations of the single-bounce orbits do not depend on k. This property gives a hint about the existence of a universal limiting behavior of the Poincaré map in the regime $k \gg 1$. Also, using Eqs. (B1),(B4) together with Eq. (39), one can show that for $k \gg 1$ the ''nontrivial'' part of the evolution of the single-bounce orbit $(1)^{+(k)}$ takes place in the vicinity of the origin of the surface of section, so that the ''universality'' of the behavior of the Poincaré map is expected to show up for $\tilde{v} \ll 1$.

Introducing the rescaled velocity

$$\mathbf{v}_\ell = \left(\frac{\tilde{v}_x}{k}, \frac{\tilde{v}_y}{k^2} \right) \tag{B7}$$

and substituting the expressions of β and $\tilde{\mathbf{v}}$ in terms of the local variables β_ℓ and $\mathbf{v}_\ell$ into the exact Poincaré map (14), in the leading order in $1/k$ we obtain the following mapping:

$$(\mathbf{v}_\ell)_{n+1} = \mathbf{\Phi}_\ell((\mathbf{v}_\ell)_n ; \beta_\ell), \tag{B8}$$

where

$$(\Phi_\ell)_x = a_{00} + a_{10}(v_\ell)_x + a_{10}(v_\ell)_x + a_{20}(v_\ell)_x^2 + a_{01}(v_\ell)_y + O\left(\frac{1}{k}\right),$$

$$\begin{aligned}(\Phi_\ell)_y = {} & b_{00} + b_{10}(v_\ell)_x + b_{10}(v_\ell)_x + b_{20}(v_\ell)_x^2 + b_{30}(v_\ell)_x^3 \\ & + b_{40}(v_\ell)_x^4 + b_{01}(v_\ell)_y + b_{02}(v_\ell)_y^2 + b_{11}(v_\ell)_x(v_\ell)_y \\ & + b_{21}(v_\ell)_x^2(v_\ell)_y + O\left(\frac{1}{k}\right),\end{aligned} \tag{B9}$$

and

$$a_{00} = -\cos^2\theta \sin\theta \left(\beta_\ell + \frac{2}{\pi} \right),$$

$$a_{10} = -\cos^2 2\theta,$$

$$a_{20} = \pi \cos^2\theta \sin\theta,$$

$$a_{01} = -2\pi \sin^2\theta \cos\theta,$$

$$b_{00} = \sin 2\theta \frac{1-\cos^4\theta}{2\pi} - \frac{\sin 2\theta \cos^2\theta}{\pi^2} - \beta_\ell^2 \frac{2 \sin 2\theta \cos^2\theta}{4},$$

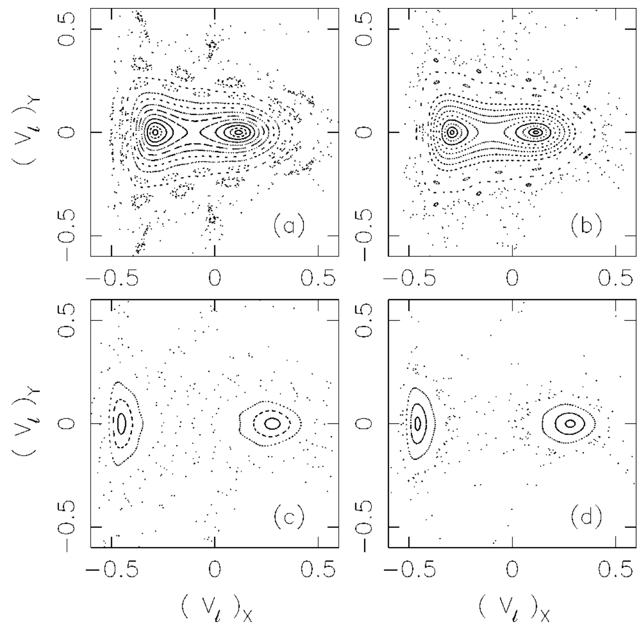

FIG. 35. Comparison of the SOS for the limiting mapping (B8) (b,d) with the ones of the exact Poincaré map (a,c). The tilt angle $\theta = 15°$, $\beta_{\mathrm{local}} = 0.2$ (a,b) and 0.5 (c,d). The SOS of the exact map is obtained for $k = 20$.

$$b_{10} = \frac{2}{\pi} \cos\theta \sin^2\theta (3 - 2\sin^2\theta) - \beta_\ell \cos 2\theta \cos^3\theta,$$

$$b_{20} = \sin 2\theta (\cos^4\theta - \sin^2\theta + \tfrac{1}{2}),$$

$$b_{30} = \pi \cos^3\theta \cos 2\theta,$$

$$b_{40} = \frac{\pi^2 \cos^4\theta \sin 2\theta}{4},$$

$$b_{01} = -\cos 2\theta - \frac{\pi \beta_\ell}{2} \sin^2 2\theta \cos^2\theta,$$

$$b_{02} = -\frac{\pi^2}{4} \sin^3 2\theta,$$

$$b_{11} = -\frac{\pi}{2} \sin 4\theta \cos\theta,$$

$$b_{21} = \frac{\pi^2}{2} \sin^2 2\theta \cos^2\theta.$$

In Fig. 35 we compare the Poincaré surfaces of section of the mapping (B8) with Poincaré surfaces of section of the exact map (14), and an excellent agreement is found.

APPENDIX C: THE MONODROMY MATRIX FOR A MANY-BOUNCE ORBIT IN SBM

To obtain the monodromy matrix for the period-one orbits, we used the nonmixing property of the single-bounce periodic orbits. Therefore, it may seem that an analytical expression for the trace of the monodromy matrix may be obtained only for the simplest nonmixing orbits. However, it is not the case. The nonmixing property substantially simplifies the calculation of the monodromy matrix, but is not necessary for an analytical description of the stability, as shown in the present appendix.

Consider a general (mixing) periodic orbit with n collisions with the barrier per period. Let $\tilde{\mathbf{v}}_k \equiv [(\tilde{v}_x)_k, (\tilde{v}_y)_k, (\tilde{v}_z)_k]$ and t_k be, respectively, the scaled velocity immediately *after* the kth collision and the time interval from kth to $(k+1)$ th collision. Once the values of $\tilde{\mathbf{v}}_k$ and t_k are known, one can linearize the Poincaré map near the point $((\tilde{v}_x)_k, (\tilde{v}_y)_k)$:

$$(\delta\tilde{v}_x)_{k+1} = (M_k)_{11}(\delta\tilde{v}_x)_k + (M_k)_{12}(\delta\tilde{v}_y)_k,$$

$$(\delta\tilde{v}_y)_{k+1} = (M_k)_{21}(\delta\tilde{v}_x)_k + (M_k)_{22}(\delta\tilde{v}_y)_k, \qquad \text{(C1)}$$

where $\delta\tilde{\mathbf{v}}_k$ and $\delta\tilde{\mathbf{v}}_{k+1}$ are the deviations of the velocity from $\tilde{\mathbf{v}}_k$ and from $\tilde{\mathbf{v}}_{k+1}$, respectively, and the matrix M_k is defined as follows:

$$M_k = \begin{pmatrix} \left.\dfrac{\partial\Phi_x(\tilde{v}_x,\tilde{v}_y)}{\partial\tilde{v}_x}\right|_{\tilde{\mathbf{v}}=\tilde{\mathbf{v}}_k} & \left.\dfrac{\partial\Phi_x(\tilde{v}_x,\tilde{v}_y)}{\partial\tilde{v}_y}\right|_{\tilde{\mathbf{v}}=\tilde{\mathbf{v}}_k} \\ \left.\dfrac{\partial\Phi_y(\tilde{v}_x,\tilde{v}_y)}{\partial\tilde{v}_x}\right|_{\tilde{\mathbf{v}}=\tilde{\mathbf{v}}_k} & \left.\dfrac{\partial\Phi_y(\tilde{v}_x,\tilde{v}_y)}{\partial\tilde{v}_y}\right|_{\tilde{\mathbf{v}}=\tilde{\mathbf{v}}_k} \end{pmatrix}. \qquad \text{(C2)}$$

Using the definition of the functions Φ_x, Φ_y [Eq. (14)], we obtain the following expressions for the components of the matrix M_k:

$$(M_k)_{11} = \cos(\omega_c t_k) - \frac{(\tilde{v}_x)_k \sin\theta \sin(\omega_c t_k)}{(\tilde{v}_z)_k} + \kappa_{1t}\kappa_{t1},$$

$$(M_k)_{12} = -\cos\theta\sin(\omega_c t_k) - \frac{(\tilde{v}_y)_k \sin\theta \sin(\omega_c t_k)}{(\tilde{v}_z)_k} + \kappa_{1t}\kappa_{t2},$$

$$(M_k)_{21} = \cos\theta\sin(\omega_c t_k) - \frac{(\tilde{v}_y)_k \sin\theta\cos\theta[1-\cos(\omega_c t_k)]}{(\tilde{v}_z)_k} + \kappa_{2t}\kappa_{t2},$$

$$(M_k)_{22} = \cos^2\theta\cos(\omega_c t_k) + \sin^2\theta - \frac{(\tilde{v}_y)_k \sin\theta\cos\theta[1-\cos(\omega_c t_k)]}{(\tilde{v}_z)_k} + \kappa_{2t}\kappa_{t2}, \qquad \text{(C3)}$$

where

$$\kappa_{1t} = (\tilde{v}_z)_k \sin\theta\cos(\omega_c t_k) - \frac{2\sin\theta\sin(\omega_c t_k)}{\beta} - (\tilde{v}_x)_k \sin(\omega_c t_k) - (\tilde{v}_y)_k \cos\theta\cos(\omega_c t_k),$$

$$\kappa_{2t} = (\tilde{v}_z)_k \sin\theta\cos\theta\sin(\omega_c t_k) - \frac{2\sin\theta\cos\theta[1-\cos(\omega_c t_k)]}{\beta} + (\tilde{v}_x)_k \cos\theta\cos(\omega_c t_k) - (\tilde{v}_y)_k \cos^2\theta\sin(\omega_c t_k),$$

$$\kappa_{t1} = -\left(\sin\theta[1-\cos(\omega_c t_k)] + \frac{(\tilde{v}_x)_k[\omega_c t_k \cos^2\theta + \sin^2\theta\sin(\omega_c t_k)]}{(\tilde{v}_z)_k} \right) \varsigma_k^{-1},$$

$$\kappa_{t2} = \left(\sin\theta\cos\theta[t_k - \sin(\omega_c t_k)] - \frac{(\tilde{v}_y)_k[\cos^2\theta + \sin^2\theta\sin(\omega_c t_k)]}{(\tilde{v}_z)_k} \right) \varsigma_k^{-1},$$

$$\varsigma_k = \sin\theta\sin(\omega_c t_k)\left((\tilde{v}_x)_k + \frac{2\sin\theta}{\beta} \right) + \frac{\omega_c t_k[\cos^2\theta - \sin^2\theta\cos(\omega_c t_k)]}{\beta}.$$

The matrix M_k relates the deviations of the velocity from the periodic orbit after two successive iterations of the Poincaré map, and is, therefore, directly connected to the monodromy matrix. The monodromy matrix of a period-n orbit relates the velocity deviation after the first collision to the velocity deviation after the nth collision, and therefore can be obtained as

$$M = \Pi_{k=1}^{n} M_k. \qquad \text{(C4)}$$

The analytical expressions for the components of the monodromy matrix (C4) and (C3) are the final results of this appendix.

APPENDIX D: PERIODS OF NONMIXING TWO-BOUNCE ORBITS

As in the case of single-bounce orbits, the derivation of the periods of the two-bounce periodic orbits is most easily performed in the ''drifting'' coordinate system (x'', y'', z''), which was defined in Eq. (36). In this coordinate system, the electron moves under the action of electric and magnetic fields, which are *both* parallel to the z'' axis: $\mathbf{E} = E\cos\theta\hat{\mathbf{z}}''$, $\mathbf{B} = B\hat{\mathbf{z}}''$. An immediate consequence of this fact is that in this coordinate system the kinetic energy of the electron at the point of collision depends on the corresponding value of z'':

$$\left.\frac{m^* v^2}{2}\right|_{z_1''} - \left.\frac{m^* v^2}{2}\right|_{z_2''} = -eE\cos\theta(z_1'' - z_2''). \qquad \text{(D1)}$$

Projected onto the plane (x'', y''), a two-bounce periodic orbit forms a repeating pattern of two arcs of two different circles, as shown in Fig. 36. Each ''kink'' in the projection of the trajectory corresponds to a collision with the barrier, when the direction of the electron velocity abruptly changes. The radius of each circle is related to the value of the cyclotron velocity: $R_c = v_c/\omega_c$. If the periodic orbit is nonmixing, then the cyclotron velocity remains unchanged and the circles have equal radii—see Fig. 36(b).

Another consequence of the nonmixing property is that all the successive collisions of the electron with the barrier are

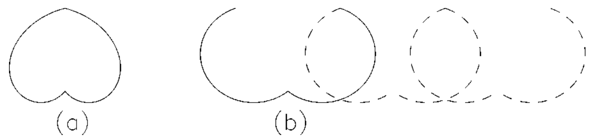

FIG. 36. A nonmixing two-bounce orbit, projected onto the (x',y') plane of the laboratory system of coordinates (a) and onto (x'',y'') plane of the "drifting" frame of reference.

separated by equal time intervals, so that the trajectory of the electron is symmetric under mirror reflection around any axis, parallel to the $\hat{\mathbf{y}}''$ and passing through any of the collision points. If it were not true, then the collisions would necessarily have to change the *absolute value* of the y'' component of the velocity. Since the x'' component of the velocity of the electron remains intact at collisions, this would introduce a nonzero energy exchange between cyclotron and longitudinal motion, which contradicts the nonmixing property of the periodic orbit.

At the point of a "nonmixing" collision the electron has zero y component of the velocity. In the drifting coordinate system this condition is equivalent to the following relation:

$$v_{y''} = -v_{z''}\tan\theta. \tag{D2}$$

Equation (D2) implies that the collision only reverses *sign* of the velocity in the (y'',z'') plane, leaving the x'' component unchanged:

$$v_{x''}^{+} = v_{x''}^{-},$$

$$v_{y''}^{+} = -v_{y''}^{-},$$

$$v_{z''}^{+} = -v_{z''}^{-}, \tag{D3}$$

where $\mathbf{v}^{-}$ and $\mathbf{v}^{+}$ are the velocities of the electron immediately before and immediately after the collision, respectively.

Let $\mathbf{v}_1$ and $\mathbf{v}_2$ be the velocities of the electron, corresponding to two successful (nonmixing) collisions with the barrier [Fig. 36(b)]. As follows from Eqs. (D3) and (11),

$$v_{z_2''}^{+} = -\left(v_{z_1''}^{+} - \frac{eE\cos\theta T}{2m^*} \right), \tag{D4}$$

where T is the period of the orbit, equal to twice the time interval between successful collisions. Due to the conservation of the cyclotron energy Eq. (D1) reduces to

$$v_{z_2''}^{+2} - v_{z_1''}^{+2} = -\frac{2eE\cos\theta}{m^*}(z_2'' - z_1''). \tag{D5}$$

Using Eq. (D4), we can rewrite Eq. (D5) as

$$v_{z_2''}^{+} - v_{z_1''}^{+} = \frac{4}{T}(z_2'' - z_1''). \tag{D6}$$

If α is the phase of the cyclotron rotation immediately after the first collision, then

$$v_{x_1''}^{+} = v_c\cos\alpha,$$

$$v_{y_2''}^{+} = v_c\cos(\alpha + \omega_c T/2) \tag{D7}$$

and

$$v_{y_1''}^{+} = v_c\sin\alpha,$$

$$v_{y_2''}^{+} = -v_c\sin(\alpha + \omega_c T/2). \tag{D8}$$

Substituting Eq. (D8) into (D2), we obtain

$$v_{z_1''}^{+} = -v_c\sin\alpha\cot\theta,$$

$$v_{z_2''}^{+} = v_c\sin(\alpha + \omega_c T/2)\cot\theta. \tag{D9}$$

The distance $z_2'' - z_1''$ can be obtained as

$$z_2'' - z_1'' = (y_2'' - y_1'')\tan\theta, \tag{D10}$$

where

$$y_2'' - y_1'' = 2\frac{v_c}{\omega_c}\sin\frac{\omega_c T}{4}\sin\left(\alpha + \frac{\omega_c T}{4}\right). \tag{D11}$$

Substituting Eqs. (D9)–(D11) into Eq. (D6), we finally obtain

$$\frac{\omega_c T}{4}\cot\frac{\omega_c T}{4} = -\tan^2\theta. \tag{D12}$$

The $(k+1)$th positive root of this equation gives the value of the period of the $(2)^{+(k)}$ orbit.

APPENDIX E: THE MONODROMY MATRIX FOR A TWO-BOUNCE NONMIXING ORBIT

The trace of the corresponding monodromy matrix for a (nonmixing) two-bounce orbit can be obtained using the general expressions developed in Appendix C. For the period-two orbits the monodromy matrix can be represented as

$$M = M_1 M_2, \tag{E1}$$

where the matrix M_k $(k=1,2)$ relates the velocity deviations from the periodic orbit at two successive collisions and can be calculated using the relations (C3). As the input information for this machinery one needs the values of the velocity of the electron immediately after each collision with the barrier ($\tilde{\mathbf{v}}_1$ and $\tilde{\mathbf{v}}_2$) and the time intervals between successive collisions (t_1 and t_2).

For the period-two nonmixing orbits, as we have shown in Appendix D, all the collisions are separated by equal time intervals, so that

$$t_1 = t_2 = \frac{T}{2}. \tag{E2}$$

To obtain the velocity at the point of collision, we can use the energy conservation condition

$$\varepsilon = \frac{m^*}{2}[(v_{x''} + v_d)^2 + v_{y''}^2 + v_{z''}^2]. \tag{E3}$$

Substituting the expressions for the velocity components at the point of collision [Eqs. (D7), (D8), and (D9)] into Eq. (E3) and using Eq. (D4), we obtain

$$\left(\frac{\beta\cos^2\theta}{2\sin\theta}\right)^2=\left[1+\sin^2\theta\tan^2\left(\frac{\omega_c T}{4}\right)\right](1+\sin^2\theta\tan^2\phi), \tag{E4}$$

where we introduced a new angle ϕ, defined as $\phi=\pi-\alpha-\omega_c T/4$.

Using Eq. (E4), we obtain

$$\tan\phi=\pm\frac{1}{\tan^2\theta}\sqrt{\frac{\left(\frac{\beta}{2}\right)^2-\left(\frac{\omega_c T}{4}\right)^2-\frac{\tan^2\theta}{\cos^2\theta}}{1+\sin^2\theta\tan^2\left(\frac{\omega_c T}{4}\right)}}, \tag{E5}$$

where the two different solutions correspond to the values of $\tan\phi$ at the two nonequivalent points of collision.

As follows from Eq. (E5), a particular period-two nonmixing orbit $(2)^{+(k)}$ exists only above the critical value of β given by

$$\beta_{c_2}=\sqrt{\left(\frac{\omega_c T}{2}\right)^2+\left(\frac{\tan\theta}{\cos\theta}\right)^2}, \tag{E6}$$

which is *exactly* equal to the value of $\beta=\beta_{b1}$, corresponding to the first period-doubling bifurcation of the single-bounce orbit $(1)^{+(k)}$, as expected.

For the velocity components at the points of collision in the nontilted ''stationary'' system of coordinates (x,y,z) we therefore obtain

$$(\tilde{v}_x)_{1,2}=-\frac{2\sin\theta}{\beta}\left(\frac{1}{\cos^2\theta}\pm\tan\left(\frac{\omega_c T}{2}\right)\times\sqrt{\frac{\left(\frac{\beta}{2}\right)^2-\left(\frac{\omega_c T}{4}\right)^2-\left(\frac{\tan\theta}{\cos\theta}\right)^2}{1+\sin^2\theta\tan^2\left(\frac{\omega_c T}{4}\right)}}\right),$$

$$(\tilde{v}_y)_{1,2}=0. \tag{E7}$$

The relations (E7) and (49) together with Eqs. (E1) and (C2) provide the complete information we need for the stability analysis. Substituting Eqs. (E7) and (49) into Eq. (C2), we obtain the matrices M_1 and M_2, which together with Eq. (E1) yield the monodromy matrix M.

APPENDIX F: PERIODS OF THE TYPE-1 MIXING TWO-BOUNCE ORBITS

Projected onto the plane (x'',y'') of the drifting frame of reference, a self-retracing mixing period-two orbit forms a repeating pattern of two portions of circles of *different* radii, with ''kinks'' at the points of collision with *exactly* same values of y''—see Fig. 37(b).

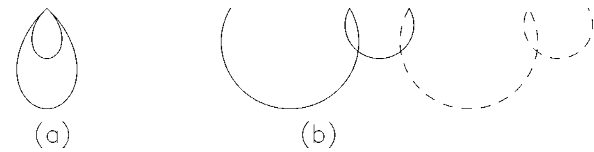

FIG. 37. A mixing self-retracing two-bounce orbit, projected onto the (x',y') plane of the laboratory system of coordinates (a) and onto (x'',y'') plane of the ''drifting'' frame of reference.

Since the x'' component of the velocity is unchanged at collisions, we obtain

$$v_{c_1}\cos\left(\frac{\omega_c t_1}{2}\right)=v_{c_2}\cos\left(\frac{\omega_c t_2}{2}\right), \tag{F1}$$

where v_c and t are the cyclotron velocity and the time interval between collisions, respectively.

The periodicity of the orbit requires, that the distance traveled by the electron in the drifting frame of reference after two successive collisions,

$$\delta x_2''=\frac{2v_{c_1}}{\omega_c}\sin\left(\frac{\omega_c t_1}{2}\right)+\frac{2v_{c_2}}{\omega_c}\sin\left(\frac{\omega_c t_2}{2}\right),$$

is equal to the displacement of this coordinate system,

$$\delta x_d''=v_d(t_1+t_2),$$

which yields

$$v_{c_1}\sin\left(\frac{\omega_c t_1}{2}\right)+v_{c_2}\sin\left(\frac{\omega_c t_1}{2}\right)=v_d\omega_c(t_1+t_2). \tag{F2}$$

Using Eq. (F1) together with Eq. (F2), we obtain

$$v_{c_1}=v_d\frac{\frac{\omega_c T}{2}}{\sin\left(\frac{\omega_c T}{2}\right)}\cos\left(\frac{\omega_c t_2}{2}\right),$$

$$v_{c_2}=v_d\frac{\frac{\omega_c T}{2}}{\sin\left(\frac{\omega_c T}{2}\right)}\cos\left(\frac{\omega_c t_1}{2}\right), \tag{F3}$$

where $T\equiv t_1+t_2$ is the period of the orbit. The ''in-plane'' components of the electron velocity $v_{x''}$, $v_{x'}$ and $v_{y'}\equiv v_{y''}$ are therefore given by

$$v_{x''}=v_d\frac{\frac{\omega_c T}{2}}{\sin\left(\frac{\omega_c T}{2}\right)}\cos\left(\frac{\omega_c t_1}{2}\right)\cos\left(\frac{\omega_c t_2}{2}\right),$$

$$v_{x'}=v_d\left(-1+\frac{\frac{\omega_c T}{2}}{\sin\left(\frac{\omega_c T}{2}\right)}\cos\left(\frac{\omega_c t_1}{2}\right)\cos\left(\frac{\omega_c t_2}{2}\right)\right),$$

$$v_{y''_{1,2}} \equiv v_{y'_{1,2}} = v_d \frac{\frac{\omega_c T}{2}}{\sin\left(\frac{\omega_c T}{2}\right)} \cos\left(\frac{\omega_c t_{2,1}}{2}\right) \sin\left(\frac{\omega_c t_{1,2}}{2}\right). \tag{F4}$$

Since the y'' coordinate is the same at each bounce, the longitudinal energy immediately after one collision is equal to the longitudinal energy immediately before the next collision, and the longitudinal velocities $v^+_{z'_1} \equiv v^+_{z''_2}$ immediately after two successive collisions the time intervals t_1 and t_2 between successive collisions must satisfy the relations

$$v_{z'_{1,2}} = \frac{eE\cos\theta t_{1,2}}{2m^*}. \tag{F5}$$

Substituting Eqs. (F4) and (F5) into Eq. (12) and using the conservation of the total energy,

$$\varepsilon = \frac{m^*}{2}(v^2_{x'} + v^2_{y'} + v^2_{z'}),$$

we obtain

$$\frac{\sin\left(\frac{\omega_c T}{2}\right)}{\frac{\omega_c T}{2}} = -\tan^2\theta \frac{\sin\left(\frac{\omega_c \delta T}{2}\right)}{\frac{\omega_c \delta T}{2}},$$

$$\left(\frac{\beta}{2}\right)^2 = \sin^2\theta \left(1 - \frac{\frac{\omega_c T}{2}\left[\cos\left(\frac{\omega_c T}{2}\right) + \cos\left(\frac{\omega_c \delta T}{2}\right)\right]}{2\sin\left(\frac{\omega_c T}{2}\right)} \right)^2 + \left(\frac{\omega_c T}{4}\right)^2 + \cot^2\theta \left(\frac{\omega_c \delta T}{4}\right)^2, \tag{F6}$$

where $\delta T \equiv |t_2 - t_1|$. This system of two equations defines the periods of all of the self-retracing mixing period-two orbits as functions of β and the tilt angle θ.

APPENDIX G: DOUBLE-BARRIER MODEL: PERIODS OF (1,1) ORBITS

In this appendix we derive Eq. (58). We perform the derivation in the drifting coordinate system (x'',y'',z''), which was defined in Eq. (36). In this coordinate system, the electron moves under the action of electric and magnetic fields, which are *both* parallel to the z'' axis: $\mathbf{E} = E\cos\theta \hat{z}''$, $\mathbf{B} = B\hat{z}''$. Since the (1,1) orbit is nonmixing, the cyclotron velocity v_c is conserved and the cyclotron radius $R_c \equiv v_c/\omega_c$ is the same for each part of the trajectory. Therefore, the (x'',y'') projection of the (1,1) orbit produces a pattern of two arcs of two different circles with *equal* radii and it looks exactly like the (x'',y'') projection of a two-bounce nonmixing orbit $(2)^+$ in the single-barrier model (see Fig. 36). However, the ''kink'' at (x''_2,y''_2) is due to collision at the *emitter* barrier [Fig. 36(b)], so that the periods of the (1,1) orbits are different from the ones of $(2)^+$.

In the drifting coordinate system the kinetic energy of the electron at the point of collision depends on the corresponding value of z'', so that [cf. (D1)]

$$\frac{m^* v_2^2}{2} - \frac{m^* v_1^2}{2} = -eE\cos\theta\left(\frac{d}{\cos\theta} + (y''_2 - y''_1)\right). \tag{G1}$$

As for the nonmixing two-bounce orbits $(2)^+$ in the single-barrier model, the successive collisions of the (1,1) with different barriers are are separated by equal time intervals, so that the trajectory of the electron is symmetric under mirror reflection around any vertical (i.e., parallel to the y'') axis, passing through any of the collision points.

At the point of a nonmixing collision with both the emitter and the collector barriers the electron has zero y component of the velocity, therefore at each collision of the (1,1) orbits the corresponding y'' and z'' components of the electron velocity are related to each other by Eq. (D2), while the velocity immediately before the collision $\mathbf{v}^-$ and the velocity immediately after the collision $\mathbf{v}^+$ satisfy the relations (D3).

Let $\mathbf{v}_1$ and $\mathbf{v}_2$ be the velocities of the electron, corresponding to two successful (nonmixing) collisions with the collector and emitter barrier, respectively. As follows from Eq. (11),

$$v^-_{z''_2} = v^+_{z''_1} - \frac{eE\cos\theta T}{2m^*}, \tag{G2}$$

where T is the period of the orbit, equal to twice the time interval between successful collisions. Substituting Eq. (G2) into Eq. (G1) and using the conservation of the cyclotron velocity, we obtain

$$v^+_{z''_1} + v^-_{z''_2} = \frac{4}{T}\left(\frac{d}{\cos\theta} + (y''_2 - y''_1)\tan\theta\right). \tag{G3}$$

If α is the phase of the cyclotron rotation immediately after the collision with the collector wall, then

$$v^+_{x''_1} = v_c\cos\alpha,$$

$$v^+_{y''_1} = v_c\sin\alpha,$$

$$v^-_{x''_2} = v_c\cos(\alpha + \omega_c T/2),$$

$$v^-_{y''_2} = v_c\sin(\alpha + \omega_c T/2), \tag{G4}$$

and [see Eq. (D2)] we obtain

$$v^+_{z''_1} = -v_c\sin\alpha\cot\theta,$$

$$v^-_{z''_2} = -v_c\sin(\alpha + \omega_c T/2)\cot\theta. \tag{G5}$$

The distance $y''_2 - y''_1$ can be obtained as [cf. Eq. (D11]

$$y''_2 - y''_1 = 2\frac{v_c}{\omega_c}\sin\frac{\omega_c T}{4}\sin\left(\alpha + \frac{\omega_c T}{4}\right). \tag{G6}$$

Substituting Eqs. (G5) and (G6) into Eq. (G3), we obtain

$$v_c \sin\left(\alpha + \frac{\omega_c T}{4}\right)\cos\left(\frac{\omega_c T}{4}\right) = -\frac{d\omega_c \tan\theta}{2\cos\theta}\frac{\cot\left(\frac{\omega_c T}{4}\right)}{\tan^2\theta + \frac{\omega_c T}{4}\cot(\omega_c T/4)}. \quad \text{(G7)}$$

The periodicity of the orbit requires, that the distance traveled by the electron in the drift frame of reference between two successive collisions with the collector barrier $x_2'' - x_1''$ is equal to the displacement of this coordinate system $v_d T$, which yields

$$v_c \cos\left(\alpha + \frac{\omega_c T}{4}\right)\sin\left(\frac{\omega_c T}{4}\right) = v_d \frac{\omega_c T}{4}. \quad \text{(G8)}$$

Using Eqs. (G7) and (G8), one can easily obtain

$$v_{y_1'}^{+} = v_c \sin\alpha = -v_d \frac{\omega_c T}{4} - \frac{d\omega_c \tan\theta}{2\cos\theta}\frac{\cot\left(\frac{\omega_c T}{4}\right)}{\tan^2\theta + \frac{\omega_c T}{4}\cot\left(\frac{\omega_c T}{4}\right)},$$

$$v_{x_1'}^{+} = -v_d + v_c\cos\alpha = -v_d\left[1 - \frac{\omega_c T}{4}\cot\left(\frac{\omega_c T}{4}\right)\right] - \frac{d\omega_c \tan\theta}{2\cos\theta}\frac{1}{\tan^2\theta + \frac{\omega_c T}{4}\cot\left(\frac{\omega_c T}{4}\right)}. \quad \text{(G9)}$$

Substituting Eq. (G9) into the equation for energy conservation,

$$v_{x'}^2 + v_{y'}^2 + v_{z'}^2 = v_0^2,$$

and using Eq. (D2), we finally obtain

$$\beta^2 = \left(\frac{\omega_c T}{2}\right)^2\left(1 + \frac{\beta^2}{\gamma(\omega_c T)^2}\frac{1 - f(\omega_c T)}{1 - \cos^2\theta f(\omega_c T)}\right)^2 + 4\sin^2\theta f^2(\omega_c T) \times \left(1 + \frac{\beta^2}{16\gamma}\frac{1}{f(\omega_c T)[1 - \cos^2\theta f(\omega_c T)]}\right)^2, \quad \text{(G10)}$$

which is exactly the Eq. (59). To obtain the period of the period-one orbits from this equation, one has to solve it together with the condition

$$(\tilde{v}_e)_z^- = \frac{2\cos\theta}{\beta}\frac{\omega_c T}{4} + \frac{\beta\cos\theta}{2\gamma\omega_c T}\frac{1 - f(\omega_c T)}{1 - \cos^2\theta f(\omega_c T)} > 0, \quad \text{(G11)}$$

which ensures that v_z just before the collision with the emitter is positive and allows to select the physically meaningful roots.

APPENDIX H: THE MONODROMY MATRIX FOR A GENERAL PERIODIC ORBIT IN THE DBM

In this appendix we consider the monodromy (stability) matrix for a general orbit in the double-barrier model. As in our stability analysis for the periodic orbits in the SBM, the velocity at each collision with the barriers and the time interval between successive collisions for the periodic orbit are considered already known.

By definition, the monodromy matrix is the linearization of the Poincaré map around the periodic orbits. It is straightforward to show that, since the evolution of the electron velocity *between* successive collisions is exactly the same in both SBM and DBM, and any collision only reverses the sign of z component of the velocity, the monodromy matrix will still be given by Eqs. (C4) and (C3), where the index k now labels all successive collisions of the electron (with *both* emitter and collector barriers).

Note that the components of the matrices M_k contain terms proportional to $1/\tilde{v}_z$. Therefore, if at any of the collisions with the emitter barrier the z component of the velocity goes to zero (as it happens in a cusp bifurcation), the components of the matrix M_k diverge, which leads to the divergence of the trace of the monodromy matrix. An immediate consequence of this behavior is that by continuity any orbit with sufficiently small v_z at one of the collisions of the emitter barrier per period is unstable.

[1] W. R. S. Garton and F. S. Tomkins, Astrophys. J. **158**, 839 (1969).
[2] A. Holle *et al.*, Phys. Rev. Lett. **61**, 161 (1988).
[3] M. C. Gutzwiller, *Chaos in Classical and Quantum Mechanics* (Springer-Verlag, New York, 1990).
[4] M. L. Du and J. B. Delos, Phys. Rev. Lett. **58**, 1731 (1987); Phys. Rev. A **38**, 1896 (1988); *ibid.* **38**, 1913 (1988).
[5] R. A. Jalabert, H. U. Baranger, and A. D. Stone, Phys. Rev. Lett. **65**, 2442 (1990).
[6] C. M. Marcus, A. J. Rimberg, R. M. Westervelt, P. F. Hopkins, and A. C. Gossard, Phys. Rev. Lett. **69**, 506 (1992).
[7] D. Weiss, K. Richter, A. Menschig, R. Bergmann, H. Schweizer, K. von Klitzing, and G. Weimann, Phys. Rev. Lett. **70**, 4118 (1993).
[8] G. Hackenbroich and F. von Oppen, Europhys. Lett. **29**, 151 (1995); J. Phys. B **97**, 157 (1995); Ann. Phys. (Liepzig) **5**, 696 (1996).
[9] K. Richter, Europhys. Lett. **29**, 7 (1995).
[10] T. M. Fromhold, L. Eaves, F. W. Sheard, M. L. Leadbeater, T. J. Foster, and P. C. Main, Phys. Rev. Lett. **72**, 2608 (1994); A. Fogarty, T. M. Fromhold, L. Eaves, F. W. Sheard, M. Henini, T. J. Foster, P. C. Main, and G. Hill, Superlattices Microstruct. **15**,

287 (1994); T. M. Fromhold, L. Eaves, F. W. Sheard, T. J. Foster, M. L. Leadbeater, and P. C. Main, Physica B **201**, 367 (1994); T. M. Fromhold, M. L. Leadbeater, L. Eaves, T. J. Foster, F. W. Sheard, P. C. Main, P. J. McDonnell, and A. Fogarty, Semicond. Sci. Technol. **9**, 488 (1994); T. M. Fromhold, M. L. Leadbeater, L. Eaves, T. J. Foster, P. C. Main, and F. W. Sheard, Surf. Sci. **305**, 511 (1994).

[11] P. B. Wilkinson, T. M. Fromhold, L. Eaves, F. W. Sheard, N. Miura, and T. Takamasu, Nature (London) **380**, 608 (1996); Science **361-362**, 696 (1996); T. M. Fromhold, P. B. Wilkinson, F. W. Sheard, L. Eaves, J. Miao, and G. Edwards, Phys. Rev. Lett. **75**, 1142 (1995).

[12] G. Muller, G. S. Boebinger, H. Mathur, L. N. Pfeiffer, and K. W. West, Phys. Rev. Lett. **75**, 2875 (1995); G. S. Boebinger, G. Muller, H. Mathur, L. N. Pfeiffer, and K. N. West, Surf. Sci. **361-362**, 742 (1996).

[13] Actually, we shall see that the current experimental system, which we describe by the double-barrier model introduced below, is not a standard KAM system due to a discontinuity in its classical mechanics, which is important for the periodic orbit theory and is addressed in detail in the text.

[14] T. S. Monteiro and P. Dando, Phys. Rev. E **53**, 3369 (1996).

[15] T. S. Monteiro, D. Delande, A. J. Fisher, and G. S. Boebinger, Phys. Rev. B **56**, 3913 (1997).

[16] E. E. Narimanov, A. D. Stone, and G. S. Boebinger, cond-mat/9707073, Phys. Rev. Lett. (to be published); E. E. Narimanov and A. D. Stone (unpublished).

[17] M. C. Payne, J. Phys. C **19**, 1145 (1986).

[18] D. L. Shepelyansky and A. D. Stone, Phys. Rev. Lett. **74**, 2098 (1995).

[19] B.V. Chirikov, Phys. Rep. **52**, 263 (1979).

[20] J. M. Greene, R. S. MacKay, F. Vivaldi, and M. J. Feigenbaum, Physica D **3**, 468 (1981).

[21] T. M. Fromhold, A. Fogarty, L. Eaves, F. W. Sheard, M. Henini, T. J. Foster, P. C. Main, and G. Hill, Phys. Rev. B **51**, 18 029 (1995).

[22] T. M. Fromhold, P. B. Wilkinson, F. W. Sheard, and L. Eaves, Phys. Rev. Lett. **78**, 2865(C) (1997).

[23] G. S. Boebinger, E. E. Narimanov, and A. D. Stone, Phys. Rev. Lett. **78**, 2866(C) (1997).

[24] E. E. Narimanov and A. D. Stone, cond-mat/9705167, Phys. Rev. Lett. **80**, 49 (1998).

[25] A. J. Lichtenberg and M. A. Lieberman, *Regular and Chaotic Dynamics* (Springer-Verlag, New York, 1994)

[26] L. Reichl, *The Transition to Chaos in Conservative Classical Systems: Quantum Manifestations* (Springer-Verlag, New York, 1992).

[27] The cusp bifurcation, which results from a discontinuity in the classical map, should not be confused with the cusp catastrophe, which is one of the generic catastrophes.

[28] F. Haake, *Quantum Signatures of Chaos* (Springer-Verlag, Berlin, 1991).

[29] The kicked-top map in the standard form in variables $(X_n, Y_n, Z_n; \alpha, \lambda)$ (Ref. 28) is identical to the approximate SBM mapping, when $X_n \equiv (\tilde{v}_{x'})_n, Y_n \equiv (\tilde{v}_{y'})_n, Z_n \equiv (\tilde{v}_{z'})_n, \alpha \equiv 2\theta, \lambda \equiv \beta/\cos\theta$.

[30] L. A. Bunimovich, Funct. Anal. Appl. **8**, 254 (1974).

[31] With a slightly different doping profile the bottom of the well could be raised above the emitter state at zero bias allowing an experimental study of the pure SBM.

[32] J.-M. Mao and J. B. Delos, Phys. Rev. A **45**, 1746 (1992).

[33] K. R. Meyer, Am. Math. Soc. Trans. **149**, 95 (1970).

[34] R. DeVogelaere, in *Contributions to the Theory of Nonlinear Oscillations*, edited by S. Lefshchetz (Princeton University Press, Princeton, NJ, 1958), Vol. IV; R. S. MacKay, in *Long Time Prediction in Dynamics*, edited by W. Horton, L. E. Reichl, and V. Szebehely (Wiley, New York, 1983).

[35] A nonzero y component of the velocity at the point of collision necessarily leads to a nonzero energy exchange between cyclotron and longitudinal motion at the emitter wall, while for the $(0,2)^+$ orbit (which at the cusp bifurcation is degenerate with an emitter orbit) the cyclotron velocity must not be changed between successive collisions with the collector barrier.

[36] G. S. Boebinger (private communication).

[37] E. J. Heller, Phys. Rev. Lett. **53**, 1515 (1984).

[38] E. B. Bogomolny, Physica D **31**, 169 (1988).

[39] M. V. Berry, Proc. Phys. Soc. London, Sect. A **423** 219 (1989).